

MEASURING THE HALF-LIFE OF O-26

By

Thomas Redpath

A DISSERTATION

Submitted to
Michigan State University
in partial fulfillment of the requirements
for the degree of

Physics – Doctor of Philosophy

2019

ABSTRACT

MEASURING THE HALF-LIFE OF O-26

By

Thomas Redpath

An interesting property of some neutron-unbound systems is true two-neutron emission where the neutrons are emitted simultaneously as opposed to a sequential decay through an intermediate state. Since neutrons are only affected by the angular momentum barrier, the timescale for this process is much shorter than for two proton emission which is dominated by the Coulomb barrier. One such case is ^{26}O where a very low decay energy was measured and the two valence neutrons are expected to occupy d -wave orbitals. Also, the ground state of ^{25}O is located 700 keV higher. Using the data from a previous measurement of the decay energy, the MoNA collaboration extracted a lifetime of $4.5^{+1.1}_{-1.5}(\text{stat}) \pm 3(\text{syst})$ ps with a confidence level of 82% (1). Results from a recent measurement give $T_{1/2} = 5.0^{+2.0}_{-1.6}(\text{stat}) \pm 1.7(\text{syst})$ ps and support the previous finding.

Measurements of neutron-unbound systems using invariant mass spectroscopy are often performed using low-intensity radioactive ion beams. Low reaction yields can be countered by using a thicker target but at the expense of larger uncertainties in the reconstructed invariant mass. A new segmented target was designed to address this trade-off, and it was first used in this experiment to re-measure the ground state half-life of ^{26}O .

Copyright by
THOMAS REDPATH
2019

ACKNOWLEDGEMENTS

I would like to thank George Perdikakis for introducing me to the fascinating world of nuclear physics. Without his mentorship, I would not have had this opportunity. I would like to thank my advisor Michael Thoennessen for all of his patience, knowledge, and wisdom. It has been an honor and a pleasure to work with him. I would also like to thank the members of my thesis committee, Alex Gade, Jaideep Singh, Morten Hjorth-Jensen, and Elizabeth Simmons for their advice and support during our meetings.

It has been a privilege to work with the MoNA Collaboration. The collective knowledge of this group is extensive, and their kind and inclusive attitude fosters a productive and supportive atmosphere. Many thanks to Anthony Kuchera, Thomas Baumann, Paul Gueye, Nathan Frank, Paul DeYoung, Jim Brown, Warren Rogers, and Sharon Stephenson for their support, advice, humor, and guidance. I would also like to thank Cole Persch and Charlie Baird for their work on this project. Finally, a huge thanks to my fellow graduate students Han Liu, Daniel Votaw and Dayah Chrisman for their help with everything from coursework to running experiments.

TABLE OF CONTENTS

LIST OF TABLES	viii
LIST OF FIGURES	x
CHAPTER 1 INTRODUCTION	1
1.1 The Shell Model	2
1.2 Nuclear Stability	5
1.2.1 Binding Energy	5
1.2.2 Half-life	6
1.2.3 Separation Energies	8
1.3 Nuclear Decays	9
1.3.1 Alpha Decay	9
1.3.2 Beta Decay	11
1.3.3 Other Decay Processes	13
1.3.4 Neutron and Proton Emission	14
1.3.4.1 One- and Two-Proton Radioactivity	14
1.3.4.2 Prospects for Two-Neutron Radioactivity	15
1.4 Dissertation Overview	16
CHAPTER 2 BACKGROUND AND MOTIVATION	17
2.1 Previous Experiments	17
2.2 Theoretical Background	18
2.2.1 Two-body decay	18
2.2.2 Three-body decay	18
2.2.3 $2n$ Decay of ^{26}O	19
2.3 The Unbinned Loglikelihood	21
2.4 Fragment momentum reconstruction and decay energy resolution	23
CHAPTER 3 EXPERIMENTAL TECHNIQUE	25
3.1 Experimental Setup	25
3.2 Beam Production	26
3.3 A1900 and Target Scintillators	27
3.4 Segmented Target	28
3.4.1 Silicon Detectors and Beryllium Targets	28
3.4.2 Signal readout and electronics	30
3.5 Sweeper magnet	32
3.6 Charged Particle Detectors	32
3.6.1 CRDCs	32
3.6.2 Ionization Chamber	34
3.6.3 Thin Timing Scintillator	34
3.7 MoNA LISA	34

3.8	Electronics and DAQ	36
3.9	Invariant Mass Spectroscopy	40
3.10	The Decay in Target Technique	42
CHAPTER 4 DATA ANALYSIS		46
4.1	Calibrations and Corrections	46
4.1.1	Segmented Target	46
4.1.1.1	Energy loss calibration	47
4.1.1.2	Reaction Target Identification	50
4.1.1.3	Position calibration	53
4.1.2	Charged particle calibrations and corrections	54
4.1.2.1	A1900 and Target scintillators	54
4.1.2.2	CRDCs	56
4.1.2.3	Ionization Chamber	61
4.1.2.4	Thin scintillator	64
4.1.3	MoNA-LISA	71
4.1.3.1	Charge Calibration (QDC)	72
4.1.3.2	Timing and x position calibration	74
4.1.3.3	Timing offsets	77
4.2	Event Selection	79
4.2.1	Beam Identification	81
4.2.2	Element Identification	81
4.2.3	Isotope Identification	82
4.2.4	Two-Neutron Selection	92
4.2.4.1	Causality Cuts	93
4.2.4.2	Decision Forest	94
4.3	Fragment Reconstruction	97
4.4	Modeling and Simulation	102
4.4.1	Incoming Beam Parameters	104
4.4.2	Energy Loss in Silicon Detectors	104
4.4.3	Reaction Parameters	105
4.4.4	Additional parameters	106
4.4.5	Cuts	107
4.4.6	Decay Model	107
4.4.6.1	One neutron decays	109
4.4.6.2	Two neutron decays	109
4.5	Extracting $T_{1/2}$	109
CHAPTER 5 RESULTS AND DISCUSSION		113
5.1	Half-life Measurement	113
5.1.1	Results	114
5.1.2	Implications	117
5.2	Segmented Target Evaluation	117
5.2.1	Target Thickness - Simulation	118
5.2.2	Improved decay energy resolution	120

5.2.3 Resolution Improvements and the Half-life Measurement 121

CHAPTER 6 SUMMARY AND CONCLUSIONS 124

6.1 Half-life measurement 124

6.2 Segmented Target 125

BIBLIOGRAPHY 126

LIST OF TABLES

Table 3.1: Thicknesses for the silicon detectors and beryllium targets. The beryllium targets were measured directly using calipers with a dial indicator and the associated measurement uncertainties are $\pm 4 \mu\text{m}$ ($\pm 0.7 \text{ mg/cm}^2 \text{ Be}$). The silicon wafer thicknesses were reported by the manufacturer with uncertainties of $\pm 1 \mu\text{m}$ ($\pm 0.2 \text{ mg/cm}^2 \text{ Si}$).	29
Table 4.1: Energy loss of eight different fragments in each silicon detector calculated using the ATIMA energy loss calculator included within the LISE++ software package (85). Calculation of these values accounts for the energy loss in the beryllium segments since the targets were always in the beam line. Variations in the material thicknesses correspond to variations in the calculated dE less than $\pm 0.008 \text{ MeV}$, so $\lesssim 0.05\%$, which is smaller than the resolution of the detectors. 49	49
Table 4.2: The second and third columns list parameter values extracted from the fits $dE_{\text{cal}} = p_0 + p_1 dE_{\text{raw}}$, see Figure 4.2. The fit errors are $< 2.0\%$ in the range from 10 MeV to 35 MeV.	50
Table 4.3: CRDC calibration parameters applied to runs before (1038 - 1121) and after (1125 - 1179) the attempted electronics repairs (see text). Bad pads are deficient cathode pads that are removed from the analysis. The pedestal subtraction is summarized by the average of all pedestal values. Similarly, the gain scaling factor is averaged over all good pads. Note that these two values are not actual calibration parameters. The xy slopes and offsets were extracted from spectra taken with the tungsten mask in place.	62
Table 4.4: Final time offsets for each MoNA/LISA table.	79
Table 4.5: Velocities, flight times and fraction of total events in the dE -ToF spectrum for the four most intense beam fragments. The velocities are calculated based on the central rigidity (4.5798 Tm) of the last dipole magnet before the target and the flight times are based on the 983.8 cm flight path between the A1900 and target scintillators. The remaining 23% of events either fall outside the strict 2D graphical cuts or resulted from low Z beam fragments.	80
Table 4.6: Iterative corrections to fragment time-of-flight used to achieve particle identification for the left, middle, and right regions identified in Figure 4.25. Note that two parameters are given for iteration three, the correction via focus x ; this is because that correction had the form $t_{\text{corr3}} = t_{\text{corr2}} - (p_2 x^2 + p_1 x)$ so the first and second values listed correspond to p_2 and p_1 respectively.	87

Table 4.7: Energy addback used to reconstruct the energy of the ^{24}O fragments produced from ^{27}F in one of the ^9Be targets. 102

LIST OF FIGURES

<p>Figure 1.1: The nuclear chart where neutron number is plotted on the x axis and proton number on the y axis. Tile color indicates decay mode: light blue (red) indicates β^- (β^+) decay, neutron (proton) emission is plotted in blue (red), alpha decay is plotted in green, and spontaneous fission in violet. Black tiles indicate stable or long-lived nuclides with $T_{1/2} \gtrsim 10^8$ years. The vertical (horizontal) blue boxes indicate magic neutron (proton) numbers. Data is from Ref. (14).</p>	2
<p>Figure 1.2: Contributions to the total potential (red curve) for a d-wave neutron in ^{16}O. The black solid curve plots the central, spin-independent component parameterized by a Woods-Saxon shape. The blue dotted curve is the spin-orbit component and the green triple dot-dashed curve plots the contribution from the centrifugal barrier. The parameters for the Woods-Saxon are $V_0 = -53$ MeV, $R_0 = 3.15$ fm, $a_0 = 0.65$ fm.</p>	3
<p>Figure 1.3: Neutron single particle energies in ^{208}Pb for three different potential models: harmonic oscillator (left), Woods-Saxon with no spin-orbit (center), and Woods-Saxon with spin-orbit (right). The shell occupancies are indicated by the numbers in square brackets. The total occupancy summed over all lower shells (2, 8, 20, ...) in the Woods-Saxon plus spin-orbit model is indicated in the spaces between groups of states. Image from Ref. (21).</p>	4
<p>Figure 1.4: Binding energy per nucleon as a function of Z for nuclides with $A = 21$. The half-lives for ^{21}C, ^{21}O, and ^{21}Mg are given in the boxes.</p>	6
<p>Figure 1.5: The radial profile for a spherically symmetric potential that approximates the interaction between the α particle and the daughter nucleus. The interaction is attractive at short range ($0 < r < a$) due to the nuclear interaction and repulsive for $r > a$ due to the Coulomb repulsion between the protons in ^4He and in the daughter nucleus.</p>	10
<p>Figure 1.6: An illustration of the three β decay processes: β^- decay is depicted in the top panel while β^+ decay and electron capture are depicted in the bottom left and bottom right panels, respectively.</p>	12
<p>Figure 1.7: Calculated lifetimes for a neutron emitter, ^{16}B, and two proton emitters, ^{16}F and ^{151}Lu, as a function of decay energy for angular momenta $L = 0$ (solid lines), $L = 1$ (dashed lines), $L = 2$ (dash-dotted lines), $L = 5$ (dotted lines). Image from (22).</p>	15

Figure 2.1: Illustrations of the energy conditions characteristic of sequential (top panel) and simultaneous (bottom panel) three body decays. 19

Figure 2.2: Decay width/half-life as a function of decay energy for $2n$ emission from ^{26}O . The gray line assumes a pure orbital [d^2] configuration coupled to the total angular momentum $L = 0$. The solid black curve shows the results for the no FSI, infinite ^{24}O mass. The blue dashed line plots the results for the no FSI calculation. The red dotted line is the calculation with the $n - n$ FSI scaled by 0.25, and the purple short-dashed curve is the full $n - n$ FSI results. The vertical red lines roughly indicate the experimental results from (48). Image adapted from (58). 20

Figure 3.1: Detector layout in the N2 vault. 26

Figure 3.2: Beam production at the Coupled Cyclotron Facility starts by heating a sample of the primary beam material in an ion source. The K500 and K1200 cyclotrons accelerate the beam which is subsequently directed onto a Be target. Fragments resulting from nuclear interactions within the target are filtered by the A1900 to provide the desired secondary beam. Image source: (76). 27

Figure 3.3: Each detector is $11\text{ cm} \times 11\text{ cm} \times 0.32\text{ cm}$ including the frame housing the silicon wafer. The thicknesses of the silicon wafers are $140\text{ }\mu\text{m}$, $135\text{ }\mu\text{m}$, $138\text{ }\mu\text{m}$, and $142\text{ }\mu\text{m}$ for detectors 0, 1, 2, and 3, respectively. The beryllium targets are 2.8 cm tall with thicknesses of 0.41 cm , 0.37 cm , and 0.33 cm for targets 1, 2, and 3, respectively. The spacing between each detector/target is 0.84 cm (0.33 inches) so in total the apparatus extends 5.04 cm along the beam axis. 29

Figure 3.4: Drawing of the segmented target mounted in the beamline: (a) beam viewer plate used to image the beam during tuning (b) base on which all detectors are mounted (c) silicon detector frame (d) beryllium target (e) base on which all targets are mounted. The viewer is mounted to the target base. Both the detector and target mount bases are attached to pneumatic drives so they can be individually inserted into and retracted from the beamline. 30

Figure 3.5: Wiring diagram showing the signal paths for the anode and corner signals from one of the silicon detectors. The anode (black arrows) and corner (blue arrows) signals were routed through separate preamp and shaping amplifiers. All shaped signals were processed by the same analog-to-digital converter. 31

Figure 3.6: Schematic of a Cathode Readout Drift Chamber (CRDC) expanded in the z -direction. The field shaping wires are omitted for visibility. 33

Figure 3.7: Schematic drawing of a single MoNA/LISA plastic scintillator bar. Image source: Ref. (81). 35

Figure 3.8: A diagram of the spatial ordering of the MoNA/LISA bars as they were configured for this experiment. Neutrons from the target travel from left to right. The spacing between groups of layers is not drawn to scale. 36

Figure 3.9: Schematic diagram of the MoNA/LISA-Sweeper electronics modified from Reference (81). Start, stop and gate signals are depicted with green, red and blue arrows respectively. The signal used as the common stop for the MoNA/LISA TDCs is indicated by the red dashed line. Shaping amplifiers are omitted for clarity. 37

Figure 3.10: An (abbreviated) diagram of the MoNA/LISA trigger logic modified from Reference (81). Each Level 1 XLM is connected to 32 CFDs to count the number of times the left and right PMTs on the same bar fire. The nine Level 1 modules (layers J-R) for the LISA array and the eight modules (layers A-H) for the MoNA array are connected to two separate Level 2 modules. The TDCs and QDCs are omitted for clarity. 39

Figure 3.11: The top panel illustrates the case of an extremely short $T_{1/2} \sim 10^{-21}$ s and the bottom panel depicts a longer $T_{1/2} \sim 10^{-12}$ s. The longer ^{26}O exists the more energy it loses as it travels through the target material. This means the neutrons are emitted at a lower velocity than if ^{26}O decays instantaneously. . . . 43

Figure 3.12: Relative speed distributions simulated with three different ^{26}O half-lives where $T_{1/2} = 0$ ps, 4 ps and 8 ps are the red dashed, black solid and blue dotted curves respectively. The relative speed is calculated as $|\vec{v}_n| - |\vec{v}_f|$ where \vec{v}_n is the neutron velocity and \vec{v}_f is the fragment velocity. The centroids of the distributions with $T_{1/2} = 4$ ps, 8 ps are shifted to the left relative to the $T_{1/2} = 0$ ps case. The reaction $^{27}\text{F}(-1p) \rightarrow ^{26}\text{O} \rightarrow ^{24}\text{O} + 2n$ was simulated. 43

Figure 3.13: Average value of the relative speed distributions as a function of half-life using the reaction $^{17}\text{C}(-1p) \rightarrow ^{16}\text{B} \rightarrow ^{15}\text{B} + n$ at 80 MeV/u (left) and 250 MeV/u (right). Image from (55). 44

Figure 3.14: Average value of the relative speed distribution as a function of half-life for $^{17}\text{C}(-1p) \rightarrow ^{16}\text{B} \rightarrow ^{15}\text{B} + n$ and three different combinations of beam energy and target thicknesses. The first number in the legend corresponds to the beam energy in units of MeV/u and the second number is the target thickness in g/cm^2 . The beam energy/target thickness combinations were selected to give approximately the same asymptotic value for very long half-lives. Image from Ref. (55). 45

Figure 4.1:	The upper panel (a) illustrates the silicon lattice structure with covalent electron bonds depicted by the black lines. The bottom panel (b) sketches the electron energy band structure. In semiconductors, $E_g \approx 1$ eV. Both illustrations are adapted from Ref. (28).	48
Figure 4.2:	Black points plot calculated energy loss (y-axis) as a function of fitted centroid of the uncalibrated dE spectrum (x-axis) for eight different fragments. The four panels show the results for the four silicon detectors. The blue lines show the extracted linear fits. The x error bars for the fit errors and the y error bars for the measurement/calculation uncertainties are smaller than the points. The parameters from the fit are listed in Table 4.2.	50
Figure 4.3:	Example target identification plots for $^{27}\text{F}(-1p) \rightarrow {}^A\text{O}$ meaning that all events plotted here enter the segmented target as ^{27}F and leave as an oxygen isotope. The top row of plots show the measured energy loss in each silicon detector. The left panel in the bottom row of plots shows the measured energy loss in the second silicon detector vs. the measured energy loss in the first silicon. The middle panel plots the third silicon energy loss vs. the second and the right panel shows the fourth silicon energy loss vs. the third.	52
Figure 4.4:	Schematic of a silicon detector and the coordinate convention used for the position calibration. The size of the arrows illustrates the signal size at each of the four corners for an ion interacting at the location of the red cross.	53
Figure 4.5:	The top panel shows an example TDC spectrum measured using an Ortec time calibrator set to deliver start and stop signals separated by integer multiples of 40 ns. The bottom panel plots the start-stop time intervals versus the peak locations from the top panel. The red line is a linear fit used to extract the conversion factor from TDC channel number to time in nanoseconds. The slope of the line is 0.0625 ns/ch and the fit error is negligible.	55
Figure 4.6:	Charge collected (black points) as a function of CRDC 2 pad number for a single event. The red curve is a Gaussian fit and the red vertical line is the centroid extracted from the fit.	57
Figure 4.7:	CRDC pedestal subtraction. The raw pad signals for CRDC 1 (left) and CRDC 2 (right) are shown in the top row. The centroid of a Gaussian fit to the charge distribution of each pad is subtracted to shift the center of each distribution to zero. The result of the pedestal subtraction is shown in the bottom row: CRDC 1 (left) and CRDC 2 (right).	58
Figure 4.8:	Example spectra showing the total charge read out by two pads in CRDC 2. Pad 68 (right) is an example of a correctly functioning pad; pad 24 (left) is deficient.	59

Figure 4.9: Calibrated position spectrum with the mask pattern overlaid. The same y offset extracted from the unreacted beam position is applied to the mask pattern.	61
Figure 4.10: Uncorrected (top row) and corrected (bottom row) drift times for CRDC1. The discontinuity at run 1125 is due to the two separate calibration parameters described in the beginning of Section 4.1.2.2.	63
Figure 4.11: The charge collected by the ionization chamber pads for unreacted ^{27}F events before (left) and after (right) gain matching.	64
Figure 4.12: The average of the ion chamber pad signals before (left) and after (right) the correction. A ^{27}F beam gate has been applied. The horizontal bands correspond to reaction products with different Z . The band between the red horizontal lines corresponds to oxygen reaction products. The correction was made to straighten this band in order to more cleanly select oxygen reaction products.	64
Figure 4.13: Diagram of the thin scintillator with its four PMTs.	65
Figure 4.14: The raw, uncorrected ToF between the target and thin PMT 0 is plotted versus charge deposited in the target scintillator. There is no correlation between the two measurements. The spectra for the other three thin scintillator PMTs are similar to this one.	66
Figure 4.15: Left column: raw energy loss versus ToF between target and thin scintillators; a scale factor was applied to the x-axes to convert TDC channel number to ns. Right column: results of correcting each ToF measurement against the signal size in each PMT. The raw energy loss signals did not need to be gain matched since independent corrections were extracted separately for each PMT.	68
Figure 4.16: Left column: q-corrected ToF versus x position measured in CRDC2. Right column: results of the x position correction.	69
Figure 4.17: Left column: qx-corrected ToF versus y position measured in CRDC2. Right column: results of the y position correction.	70
Figure 4.18: The uncorrected (black dotted histogram) and corrected (solid red histogram) ToF distributions for unreacted ^{27}F calculated as the event-by-event average of the thin PMT signals. An offset has been applied to center the velocity distribution on the value determined from energy loss calculations of the ^{27}F beam through the segmented target (see text).	71

- Figure 4.19: Example raw (left) and calibrated (right) QDC spectra. The pedestal visible in the left spectrum is suppressed using a hardware threshold during the experiment and while recording a subsequent cosmic run used to generate the right plot. The red curve is a Gaussian fit to the cosmic peak. The QDC channel numbers of the pedestal and the cosmic peak determined a scaling to convert QDC channel number to light deposited in units of MeVee. The muon peak appears ~ 20 MeVee in the calibrated spectrum. 73
- Figure 4.20: An example of an uncalibrated TDC spectrum (top panel) generated using the time calibrator. The narrow peaks represent recorded events where the time between the start and stop pulses is an integer multiple of 40 ns. The known time intervals are plotted against the peak locations (bottom panel) to extract a scale factor that converts TDC channel number to a time. The right panel displays histograms of the calculated TDC slopes. 75
- Figure 4.21: In the left panel, the black histogram plots the difference between calibrated times $t_{\text{left}} - t_{\text{right}}$, the blue curves are Fermi function fits to the left and right edges of time difference distribution and the red vertical lines are the edges extracted from the fits. The right panel shows the resulting x position spectrum. Events plotted in these spectra are required to have a calibrated light deposited signal > 4 MeVee. 76
- Figure 4.22: A χ^2 minimization routine was used to fit Gaussian functions to the fragment and neutron velocity distributions; the centroids and fit errors are plotted for data (black circles) and simulation (open blue diamonds). The fit results for the fragment velocities are plotted in the top row and the neutron velocities in the bottom row. The left, middle and right columns correspond to fit results where the distributions are made from events where the reaction occurred in the first, second and third beryllium target, respectively. 78
- Figure 4.23: Spectrum used for beam fragment identification. The faster fragments (see Table 4.5) have a shorter ToF (x -axis) and fragments with a higher Z deposit more energy in the first silicon detector (y -axis). 80
- Figure 4.24: Energy loss (dE) measured in the ionization chamber versus the time-of-flight from the target to the thin scintillator. Only events that fall inside the ^{27}F beam gate (see Figure 4.23) are plotted here. The most intense region corresponds to unreacted ^{27}F beam fragments ($Z = 9$); the band immediately below corresponds to oxygen ($Z = 8$) reaction products $^{27}\text{F}(-1p) \rightarrow^A \text{O}$ 82
- Figure 4.25: CRDC1 x position versus CRDC2 x position; Two functioning detectors would display a smooth, positive correlation. The red lines outline 2D gates that attempt to select events with a good CRDC1 position measurement. 84

Figure 4.26: The correlation between ToF dispersive angle and position is shown for oxygen beam fragments on the left and oxygen reaction fragments from ^{27}F on the right. 85

Figure 4.27: The top panel is a projection onto the 2D dispersive position versus dispersive angle plane. The iso-time-of-flight contour is shown in black. In the bottom panel the dispersive plane emittance parameter displays a linear correlation with measured ToF and can be projected onto an axis perpendicular to the red line for the purpose of making a 1D gate. 86

Figure 4.28: The top three panels plot the corrected ToFs for the three different regions. For each region a 1D gate is indicated by the red lines and arrows, and is applied to the CRDC 2 x distributions plotted in the bottom panel. The red, black, and blue points plot the CRDC2 x distributions for events under the left, middle, and right region gates respectively. These gates select events where the oxygen reaction products have a long ToF and are detected on the high rigidity ($+x$) side of CRDC2. 89

Figure 4.29: The top three panels plot the corrected ToFs for the three different regions. For each region a 1D gate is indicated by the red lines and arrows, and is applied to the CRDC 2 x distributions plotted in the bottom panel. The red, black, and blue points plot the CRDC2 x distributions for events under the left, middle, and right region gates respectively. The gates shown here select events with a slightly shorter flight time and CRDC2 x distributions that are shifted to the left compared to the gates shown in Figure 4.28. 90

Figure 4.30: The top three panels plot the corrected ToFs for the three different regions. For each region a 1D gate is indicated by the red lines and arrows, and is applied to the CRDC 2 x distributions plotted in the bottom panel. The red, black, and blue points plot the CRDC2 x distributions for events under the left, middle, and blue region gates respectively. The gates applied to these plots select events with the shortest ToFs for oxygen reaction products. Note that the CRDC2 x distributions are shifted further to the left than the other two sets of gates. 91

Figure 4.31: An illustration of A^2 versus A/Z for $10 \leq A \leq 30$ and $Z \leq A$. Each point is a separate nucleus (some unphysical). The red curves indicate curves of constant Z . Three nuclei with $A/Z = 3$ that are in the Sweeper acceptance are highlighted with gray circles. 92

Figure 4.32: Ion chamber ΔE versus global corrected ToF for all events from the ^{27}F beam that fall inside one of the region gates shown in Figure 4.25. The red line corresponds to the $A/Z = 3$ line in Figure 4.31. 93

Figure 4.33: One dimensional particle identification for the oxygen reaction products. Events plotted here are required to fall inside the oxygen reaction product gate shown in Figure 4.24 and inside one of the “good” CRDC1 gates shown in Figure 4.25. In addition, coincidence with one of the MoNA/LISA bars is required. 94

Figure 4.34: An illustration of the relevant position vectors calculated in a two-neutron event. The position vector \vec{d}_0 (\vec{d}_1) is from the target to the location of the first (second) interaction in MoNA/LISA; $\vec{d}_{01} = \vec{d}_1 - \vec{d}_0$ 95

Figure 4.35: Schematic view of a decision tree. At each node a binary cut is made on one of the parameters $x_{i,j,k,\dots}$. Image source: (95). 96

Figure 4.36: The classifier output is plotted to examine the reliability of the decision forest. In the top panel, the classifier output distributions for simulated, labeled true two-neutron (blue) and one-neutron scattering (orange) events are plotted. The black curve is the sum of the two distributions. In the bottom panel, the decision forest is compared to the causality cuts; the green histogram plots the classifier output for events that the causality cuts identify as true two-neutron events. The gray histogram shows the classifier output for events that the causality cuts identify as one-neutron scattering events. The red line indicates the final cut on the classifier output used in the analysis. . . . 98

Figure 4.37: The correlation between path length as a function of CRDC2 x is plotted in the upper right panel. The abscissa for each point is the mean of a Gaussian fit to the CRDC2 x distribution. The ordinate of each point is the mean of a Gaussian fit to the calibrated ToF distribution multiplied by the velocity of ^{27}F after the segmented target; the error bars represent the fit error and the uncertainty in the velocity calculation introduced by the uncertainties in the silicon and beryllium thicknesses, $\pm 1 \mu\text{m}$ and $\pm 4 \mu\text{m}$ respectively. The left and bottom right panels are examples of the ToF and CRDC2 x spectra, respectively. Red curves plot the Gaussian fits. 100

Figure 4.38: The left panel plots the simulated distribution of angles θ between the lab-frame fragment momentum vector and the beam axis. The middle and right panels plot the three-body decay energies reconstructed from the simulated detector responses where the decay energy available for every simulated event was 50 keV (middle) and 1 MeV (right). The red curves plot the decay energies calculated with the fragment angle $\theta = 0$ and the black curves include the angle information. 101

Figure 4.39: The $(x, y, \theta_x, \theta_y)$ profile for the simulated beam was set through comparisons to the experimental distributions plotted from the unreacted ^{27}F data set. The first silicon x, y position distributions are shown in the top row and the CRDC2 x, y distribution are plotted in the bottom row. Orange points are data and blue lines are simulation.	105
Figure 4.40: Energy loss of ^{27}F beam fragments measured in the four silicon detectors is plotted by the black dots, red triangles, blue diamonds, and brown crosses; solid curves plot the simulation output. The resolution of the silicon detectors is simulated using a Gaussian with $\sigma = 0.9$ MeV.	106
Figure 4.41: Fragment and neutron position spectra for ^{24}O events in coincidence with two hits in MoNA/LISA. Simulated position spectra (blue curves) are overlaid on the corresponding experimental spectra (black points). The top left and right panels plot the CRDC2 x and y spectra respectively. The middle left and right panels show the x and y distributions for the first time-sorted hit in MoNA/LISA. The bottom left and right panels show the x and y distributions for the second hit in MoNA/LISA.	108
Figure 4.42: Negative LnL curves extracted from a pseudo data set with $T_{1/2} = 2$ ps (left) and a second pseudo data set with $T_{1/2} = 4$ ps (right). In both panels, range values of 0.005 cm/ns, 0.050 cm/ns, 0.100 cm/ns, and 0.500 cm/ns correspond to the black dots, red triangles, blue diamonds, and gray crosses respectively.	112
Figure 5.1: Half-life extracted from $^{23}\text{O}^* \rightarrow ^{22}\text{O} + n$ data. The left panel shows the relative speed distribution for data (black points) and three simulations with $T_{1/2} = 0$ ps, 4 ps, 7 ps. The right panel shows the negative loglikelihood as a function of half-life. The red line indicates the upper limit of 1.7 ps corresponding to a 95% confidence level.	113
Figure 5.2: The relative speed distributions and LnL curves for two sets of analysis gates used to isolate events corresponding to the $^{26}\text{O} \rightarrow ^{24}\text{O} + 2n$ decay. The top row shows the results for events extracted using the causality cuts and the bottom row shows the results using the decision forest. In the relative speed plots, the black points represent data and the curves are from simulations with $T_{1/2} = 0$ ps, 4 ps, and 8 ps. The vertical red lines on top of the LnL curves denote the 1σ statistical uncertainties.	115
Figure 5.3: The gray vertical lines indicate the upper and lower limits on the half-life obtained from adding, in quadrature, the statistical and systematic uncertainties quoted in Ref. (1). The red vertical lines denote the upper and lower limits and the black points show the negative loglikelihood curve from the current analysis using the causality cuts.	116

Figure 5.4: Decay width/half-life as a function of decay energy for $2n$ emission from ^{26}O . The gray line assumes a pure orbital $[d^2]$ configuration coupled to the total angular momentum $L = 0$. The solid black curve shows the results when no final state interaction (FSI) and an infinite ^{24}O mass is simulated. The blue dashed line plots the results when no FSI and the correct ^{24}O mass is simulated. The red dotted line shows the calculation results when the $n - n$ FSI is scaled by 0.25, and the purple short-dashed curve includes the full $n - n$ FSI. The vertical red lines roughly indicate the experimental results from (48), and the green shaded area indicates half-life limits obtained in this work. Image adapted from (58). 118

Figure 5.5: Results from a simulation run with a single 11.1 mm target (gray curves) and with a segmented target (red curves). The 11.1 mm target is the sum of the thicknesses of the three beryllium targets used in the segmented target. For the segmented target simulation, the detector and target thicknesses in the simulation are the same as those listed in Table 3.1. The left panel plots the difference in speed $|\vec{v}_n| - |\vec{v}_f|$ between the first detected neutron and the charged fragment and the right panel plots the three body decay energy reconstructed from the simulation. Deviation from the 50 keV input decay energy is due to the energy addback. Neutron resolutions are turned off. . . . 119

Figure 5.6: Measured relative speed and three body decay energy spectra for $^{27}\text{F}(-1p) \rightarrow ^{26}\text{O} \rightarrow ^{24}\text{O} + 2n$ are drawn as black triangles and black circles, respectively. The solid curves are spectra reconstructed from simulation. Two different decay channels were simulated (see inset of top right panel): (1) direct population of the ^{26}O ground state followed by two-neutron emission (red solid line) and (2) population of the ^{26}O first excited state followed by a sequential neutron emission through the ^{25}O ground state (green dashed line). In the top row, the energy addback is chosen event-by-event based on which beryllium segment was identified as the reaction target using the method described in Section 4.1.1.2. In the bottom row, the addback for the middle beryllium segment is applied to all events. 121

Figure 5.7: The top left plot shows the relative speed reconstructed using the target identification (Section 4.1.1.2) to inform the energy addback. The black points are data and the curves represent relative speed distributions simulated assuming various $T_{1/2}$ for ^{26}O - red dashed is 0 ps, black solid is 4 ps and blue dotted corresponds to 8 ps. In the bottom left a single value for the addback (corresponding to the energy loss through half of a single thick target) is used for all measured and simulated events. The right panels show the extracted negative loglikelihood curves for the segmented (top) and single thick (bottom) target reconstructions. 122

CHAPTER 1

INTRODUCTION

In the early twentieth century, remarkable scientific advances were reshaping and expanding humanity's understanding of the physical universe. New experimental findings coupled with a revolutionary new theoretical framework set the stage for the development of modern nuclear physics. Antoine Henri Becquerel's accidental discovery¹ of radioactivity in 1896 (4; 5; 6; 7; 8; 9; 10) followed by Marie and Pierre Curie's work with radioactive elements provided the first hints for the existence of a dynamic system inside the atom that is still being explored today. Ernest Rutherford reported the discovery of the atomic nucleus in 1911 based on the results of an experiment carried out by his student Ernest Marsden (11), and James Chadwick reported his discovery of the neutron in 1932 (12). These discoveries, together with quantum mechanics and Ernest Lawrence's invention of the cyclotron in 1929 (13) helped shape a new field focused on understanding the atomic nucleus.

Atomic nuclei are composed of protons and neutrons, and each species of nucleus is uniquely identified by its number of protons (Z) and number of neutrons (N). The >3000 currently known nuclei can be organized graphically by plotting Z as a function of N as shown in Figure 1.1. The total number of nucleons (protons and neutrons) $A = Z + N$ and Z are commonly used to refer to a nucleus. A convenient shorthand notation identifies a nucleus as A_ZX_N or more compactly AX where X is the atomic symbol that identifies the number of protons. Different nuclei with the same number of protons and different N are referred to as isotopes. The isotopes of a single element (constant Z) occupy one row in Figure 1.1. Nuclei with the same number of neutrons and different Z are referred to as isotones. The term nuclide refers to an atom containing the nucleus AX .

Atomic nuclei account for 99.9% of the mass of visible matter, and they involve length scales

¹It should be noted that the same effect that Becquerel observed was also observed by photographer Abel Niepce de Saint Victor 40 years earlier, but there were no follow-up investigations of the phenomenon until after Becquerel's report (2). Becquerel shared the 1903 Nobel Prize with Marie and Pierre Curie (3).

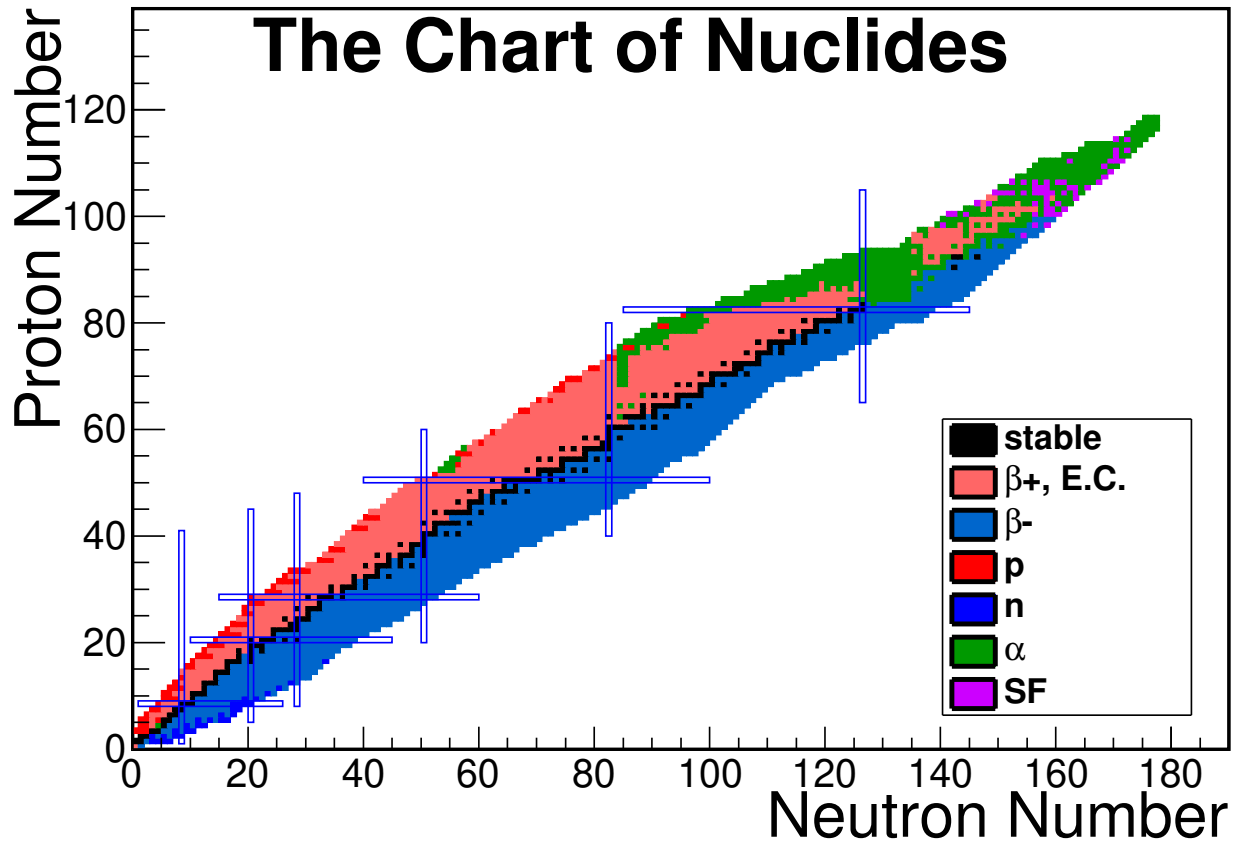


Figure 1.1: The nuclear chart where neutron number is plotted on the x axis and proton number on the y axis. Tile color indicates decay mode: light blue (red) indicates β -(+) decay, neutron (proton) emission is plotted in blue (red), alpha decay is plotted in green, and spontaneous fission in violet. Black tiles indicate stable or long-lived nuclides with $T_{1/2} \gtrsim 10^8$ years. The vertical (horizontal) blue boxes indicate magic neutron (proton) numbers. Data is from Ref. (14).

$\sim 10^{-15}$ m, densities of order 2.3×10^{17} kg/m³ and energies ranging from a few keV to a few MeV. The time scale for nucleon motion inside the nucleus is $\sim 10^{-22}$ s. Time scales for nuclear decays vary over an enormous range from picoseconds to billions of years. Furthermore, since a nucleus can be comprised of anywhere from 1 to ≈ 300 nucleons, it qualifies as a dynamic many-body quantum system.

1.1 The Shell Model

Due to the mathematical complexities associated with solving the many-body problem, simplified models were constructed to interpret empirical observations. One such model sought to describe how nuclei with certain “magic” numbers (2, 8, 20, 28, 50, 82, and 126) of neutrons or

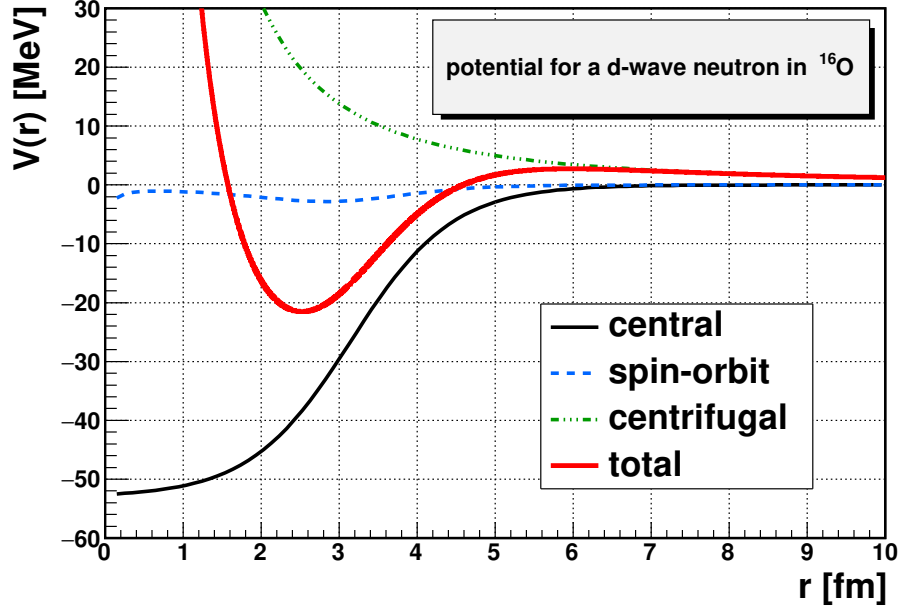


Figure 1.2: Contributions to the total potential (red curve) for a d-wave neutron in ^{16}O . The black solid curve plots the central, spin-independent component parameterized by a Woods-Saxon shape. The blue dotted curve is the spin-orbit component and the green triple dot-dashed curve plots the contribution from the centrifugal barrier. The parameters for the Woods-Saxon are $V_0 = -53$ MeV, $R_0 = 3.15$ fm, $a_0 = 0.65$ fm.

protons are particularly stable (15; 16). A similar effect is observed for atomic electrons where more energy is required to remove an electron from atoms of the noble gases than from atoms of other elements. This similarity inspired the idea of nucleon orbitals or shells in analogy to those of atomic electrons.

The first step in building a nuclear shell model is to choose a form for the potential that binds nucleons together. Since the force between nucleons is short-ranged and the nuclear density is constant (17), a nucleon in the center of the nucleus will interact with the same number of neighbors regardless of its position. Therefore, the potential should be roughly constant and negative inside the nucleus. At the surface of the nucleus, there are fewer neighbors with which a nucleon can interact, therefore the potential should decrease towards the edge. This qualitative behavior is often parameterized using a Woods-Saxon potential, see the black curve in Figure 1.2,

$$f(r) = \frac{V_0}{1 + \exp[(r - R_0)/a_0]}$$

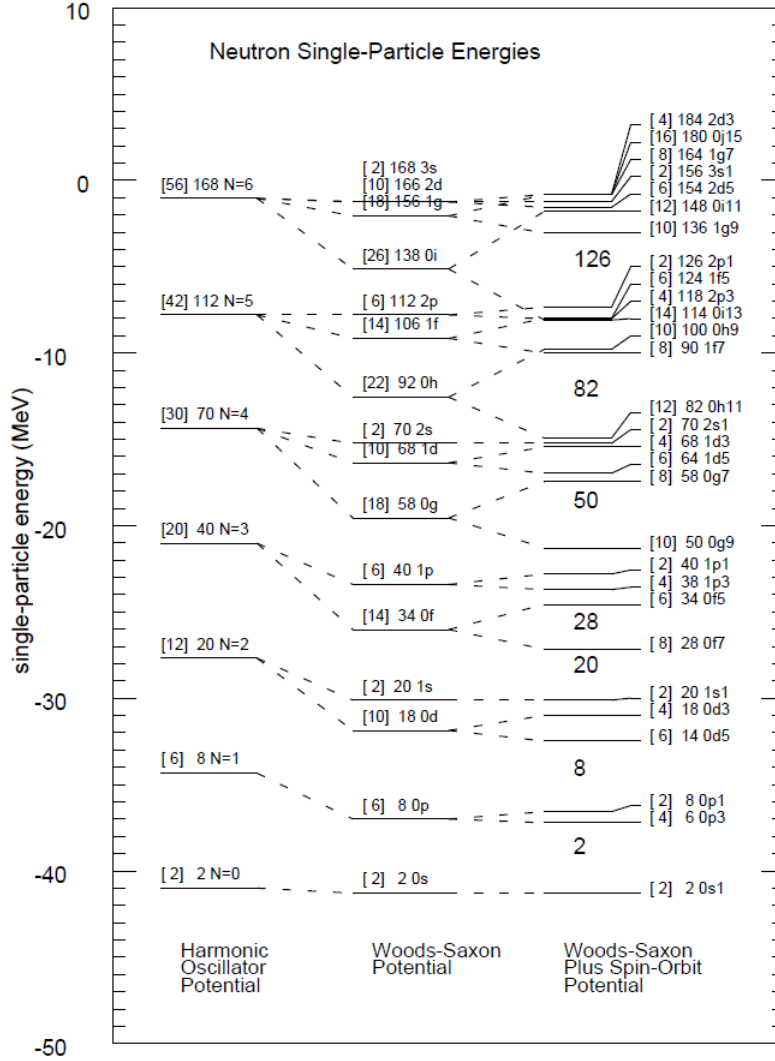


Figure 1.3: Neutron single particle energies in ^{208}Pb for three different potential models: harmonic oscillator (left), Woods-Saxon with no spin-orbit (center), and Woods-Saxon with spin-orbit (right). The shell occupancies are indicated by the numbers in square brackets. The total occupancy summed over all lower shells (2, 8, 20, ...) in the Woods-Saxon plus spin-orbit model is indicated in the spaces between groups of states. Image from Ref. (21).

with parameters V_0 , R_0 , and a_0 fixed through comparison to experimental data. Adding a spin-orbit term results in energy levels spaced such that their occupancies reproduce the observed magic numbers (18; 19; 20), see Figure 1.3.

The resulting model describes a single particle moving in a mean-field $V(r)$. The eigenstates of the single-particle Hamiltonian that includes the potential described above are characterized by their energies and a set of quantum numbers, see Figure 1.3. Properties of the nucleus are

determined by filling the single-particle levels according to the Pauli exclusion principle. Modern versions of the shell model define a Hamiltonian matrix as the sum of one- and two-body operators that can be diagonalized to find the eigenvalues of a particular few-body system. Since the number of basis states grows factorially with the number of orbitals included in the calculation, nucleons in filled shells are often approximated as a single core and truncations of the basis space are made to circumvent computational limitations.

1.2 Nuclear Stability

1.2.1 Binding Energy

The atomic mass is a basic quantity that can be measured for the ground states of nuclei. The mass energy of a nucleus A_ZX_N is the mass energy of the atom minus the mass energy of Z electrons minus the total electronic binding energy. The decay and reaction energies typically dealt with in nuclear physics involve differences in mass energies so the electron binding energies (which are $\sim 10^{-6}$ times the typical atomic mass energies) tend to cancel (17). The nuclear binding energy is defined as the mass difference between a nucleus and its constituent Z protons and N neutrons

$$B \equiv \left[Zm({}^1\text{H}) + Nm_n - m({}^A\text{X}) \right] c^2$$

where the proton and electron masses are grouped into Z neutral hydrogen atoms. The conversion factor $c^2 = 931.494273 \text{ MeV/u}$ can be convenient when masses are given in atomic mass units (u). The binding energy, B , is the energy needed to break a nucleus into its constituent nucleons, and it represents a quantitative measure for nuclear stability.

The concept of stability can be visualized by plotting the binding energy as a function of Z for nuclides with a given mass number, A . The black points in Figure 1.4 plot the binding energy per nucleon for nine nuclides with $A = 21$ and different (N, Z) . A local maximum is clearly seen at $Z = 10$ corresponding to ${}^{21}\text{Ne}$ which is the most tightly bound of this group.

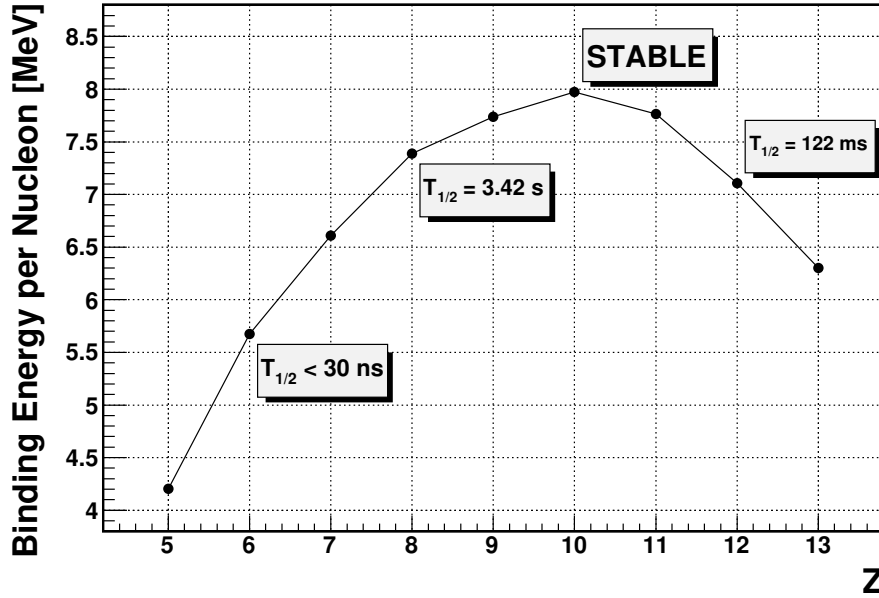


Figure 1.4: Binding energy per nucleon as a function of Z for nuclides with $A = 21$. The half-lives for ^{21}C , ^{21}O , and ^{21}Mg are given in the boxes.

1.2.2 Half-life

The stability of a nucleus can also be quantified in terms of its half-life, mean lifetime or decay rate. Consider a collection of identical unstable nuclei ^AX that decay at some rate λ disintegrations per unit time. The total number of decays per unit time will be proportional to the number of ^AX nuclei in the sample which is itself a function of time. This situation is modeled using a first order ordinary differential equation (Eq. 1.1) for which the solution may be written as in Eq. 1.2.

$$-dN(t) = \lambda N(t) dt \quad (1.1)$$

$$N(t) = N(0)e^{-\lambda t} \quad (1.2)$$

The half-life is defined as the amount of time for half of the nuclei to decay. The mean lifetime is the average time that a nucleus survives before decaying. The relationship between half-life ($T_{1/2}$), mean lifetime (τ) and decay rate (λ) is given by

$$T_{1/2} = \frac{\ln 2}{\lambda} = \tau \ln 2.$$

More stable nuclei will typically have longer half-lives (see Figure 1.4). Nuclides that have not been observed to decay are considered stable, and all other nuclei are converted into these stable nuclei through various decay processes (see Section 1.3) with half-lives that range from picoseconds to billions of years.

Another way to quantify the stability of a nuclear state comes from considering the time-dependent wave function

$$|\Psi(r,t)|^2 = |\Psi(r,0)|^2 e^{-\lambda t}$$

and its Fourier transform

$$P(E) = k \int_{-\infty}^{+\infty} \exp[-iE_0 t/\hbar - \lambda t/2 + iEt/\hbar] \quad (1.3)$$

where λ is the same decay constant defined above. Taking $t = 0$ to be the time at which the initial unstable nucleus was created, the integral in Eq. 1.3 can be evaluated. The normalization constant k is found to be $i/(2\pi)$ and the probability of finding the nucleus with energy E is given by the distribution

$$|P(E)|^2 = \frac{1}{4\pi^2} \frac{1}{(E - E_0)^2 + \frac{\hbar^2 \lambda^2}{4}} \quad (1.4)$$

which has a full width at half maximum $\Gamma = \hbar\lambda$. Eq. 1.4 implies that multiple energy measurements made on identically prepared time-evolving states will result in a distribution of energies. Furthermore, a larger decay rate corresponds to a wider range in the measured energies. The width Γ can be related to the half-life/lifetime/decay rate according to

$$\Gamma = \frac{\hbar \ln 2}{T_{1/2}} = \frac{\hbar}{\tau} = \hbar\lambda \quad (1.5)$$

For a state with $T_{1/2} = 1$ ps, Eq. 1.5 gives $\Gamma \approx 10^{-4}$ eV.

1.2.3 Separation Energies

Two quantities related to the binding energy are the neutron and proton separation energies denoted as S_n and S_p , respectively. These values are defined as differences between the binding energies of two nuclei

$$S_n \equiv B \left({}^A_Z X_N \right) - B \left({}^{A-1}_Z X_{N-1} \right)$$
$$S_p \equiv B \left({}^A_Z X_N \right) - B \left({}^{A-1}_{Z-1} X_N \right)$$

where S_n (S_p) determines the amount of energy needed to remove a neutron (proton) from nucleus ${}^A_Z X_N$. These separation energies determine whether or not a particular collection of Z protons and N neutrons can form a bound nucleus. A negative separation energy implies that the nucleus ${}^A_Z X_N$ is unbound with respect to one nucleon emission. The distinction between bound and unbound systems leads to the concept of neutron and proton driplines. There is some debate as to the exact definition of the driplines (see Section 2.1 of Ref. (22)), but this dissertation adopts the convention that the neutron (proton) dripline is defined by the limit where S_n (S_p) crosses zero. The neutron and proton driplines should then be discussed in terms of isotones and isotopes respectively (22). With this convention, the neutron dripline has been measured up to $N = 24$ assuming ${}^{33}\text{F}$ is unbound. The proton dripline has been mapped for odd Z nuclei up to $Z = 91$ but only up to $Z = 12$ for even Z .

These concepts of unbound nuclei and driplines raise the question “at what point is a collection of nucleons considered a nucleus?” There are no established criteria by which this question is typically evaluated. One convention suggests comparing the measured half-life of a nucleus to the typical timescales for nucleon motion (10^{-22} s) (22). Another convention re-casts the question as “what constitutes the existence of a nuclide?” This question incorporates the timescale over which a nucleus acquires electrons. From this standpoint, the authors in (23) define radioactivity to be any nuclear decay process “much slower than filling the K vacancy, whose duration, in principle, can be measured directly, and with a width much smaller than the thermal energy at room temperature.”

By this convention unstable nuclides “exist” if they decay with a $T_{1/2} \gtrsim 10^{-14}$ s. The discussion in this dissertation does not require adopting a specific convention for the existence of a nucleus or nuclide, but it does adopt the definition of radioactivity as a subset of nuclear decay processes for which $T_{1/2} \gtrsim 10^{-14}$ s.

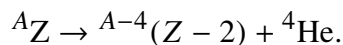
At this point it is important to highlight a distinction between (1) stability for bound nuclei and (2) stability in terms of bound versus unbound systems. In the first case, unstable nuclei will undergo some decay process that results in one or more nuclei with a higher binding energy than the original nucleus. In the second case, the unbound system will emit one or more nucleons to produce a bound system.

1.3 Nuclear Decays

A nucleus is said to be stable if it has not been observed to undergo any processes by which its N and Z spontaneously change or by which it spontaneously disintegrates into smaller nuclei. There are 254 stable nuclides (24) that form the valley of stability on the nuclear chart (Figure 1.1). Currently more than 3000 nuclei have been observed experimentally with as many as 4000 more predicted to exist (25). Most nuclei are unstable and undergo some decay process that emits a characteristic type of radiation. The decaying nucleus is sometimes called the parent nucleus while the decay products are referred to as daughters.

1.3.1 Alpha Decay

Alpha decay is a process through which a helium nucleus ($A = 4$ and $Z = 2$) is emitted from a larger nucleus,



The net energy released in this process (the Q value) is given by the mass difference between the parent nucleus and the daughters,

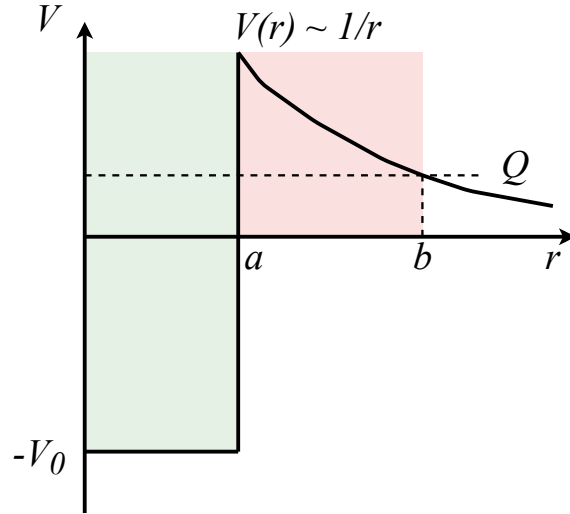


Figure 1.5: The radial profile for a spherically symmetric potential that approximates the interaction between the α particle and the daughter nucleus. The interaction is attractive at short range ($0 < r < a$) due to the nuclear interaction and repulsive for $r > a$ due to the Coulomb repulsion between the protons in ${}^4\text{He}$ and in the daughter nucleus.

$$Q_\alpha = (m_Z - m_{Z-2} - m_\alpha)c^2.$$

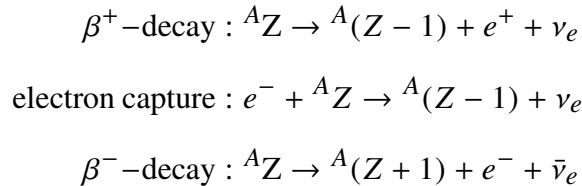
Spontaneous emission of an α particle can occur in cases where Q_α is positive. With the exception of ${}^8\text{Be}$, the condition $Q_\alpha > 0$ holds mainly for nuclides with $Z \gtrsim 50$ and $N \gtrsim 60$.

A straightforward quantum mechanical theory describing alpha decay was presented in 1928 (26; 27). In this theory the alpha particle is approximated as a particle confined in a spherically symmetric potential with the radial profile sketched in Figure 1.5. The attractive potential created by the average nuclear force in the region $0 < r < a$ and the repulsive Coulomb potential in the region $r > a$ create a barrier, and there is a non-zero probability that the α particle will tunnel through the barrier. The transmission probability can be calculated analytically treating the barrier as a sequence of rectangular barriers with heights $\propto 1/r$ and widths dr . Then, after making the assumption that $(Q_\alpha/B) \ll 1$ where B is the height of the barrier at $r = a$, one can arrive at a formula for the half-life of the α decay in terms of Q_α , B , the depth of the attractive well (V_0) and the charge of the daughter nucleus (see Equation 8.18 of Ref. (17)). This approximation is able to reproduce the qualitative trend in 119 experimentally measured α decay half-lives spread over 25

orders of magnitude (21). The calculated half-lives are systematically shorter by roughly 2 orders of magnitude due the various assumptions made, including the spherical shape and mean nuclear radius $1.25A^{1/3}$ of the daughter nucleus. Nevertheless, this approximation highlights several key aspects of the decay-by-particle-emission process. First, the half-life is extremely sensitive to the amount of energy available in the decay, Q_α . The measured (calculated) half-life for the α decay of ^{222}Th is 2.8×10^{-3} s (6.3×10^{-5} s); the measured (calculated) half-life for the α decay of ^{232}Th is 4.4×10^{17} s (2.6×10^{16} s). The Q values are 8.13 MeV and 4.08 MeV for the ^{222}Th and ^{232}Th decay, respectively. A decrease in Q_α by a factor of 2 results in a half-life that is 20 orders of magnitude longer (17). Second, one can see that allowing the α particle to have some non-zero angular momentum l_α will increase the potential energy in the region $r > a$ in Figure 1.5 due to the centrifugal potential $l(l+1)\hbar^2/2mr^2$. The result is a thicker barrier, a decreased probability for the α particle to tunnel through and, therefore, a longer half-life. So, qualitatively, longer half-lives correspond to lower decay energies and larger orbital angular momenta.

1.3.2 Beta Decay

There are three types of beta decay that involve converting a proton into a neutron or vice versa. They are illustrated in Figure 1.6 and can be represented by the following equations:



In β^+ decay, a proton inside the nucleus is converted into a neutron that remains inside the nucleus and a positron and an electron neutrino are emitted. A similar process, referred to as electron capture, occurs when an electron in one of the low-lying atomic orbitals is captured by the nucleus and converts a proton into a neutron and an electron neutrino. The mirror process, β^- decay, involves spontaneous conversion of a neutron into a proton and emits an electron and an electron anti-neutrino. Beta decay processes represent the primary methods by which most of the

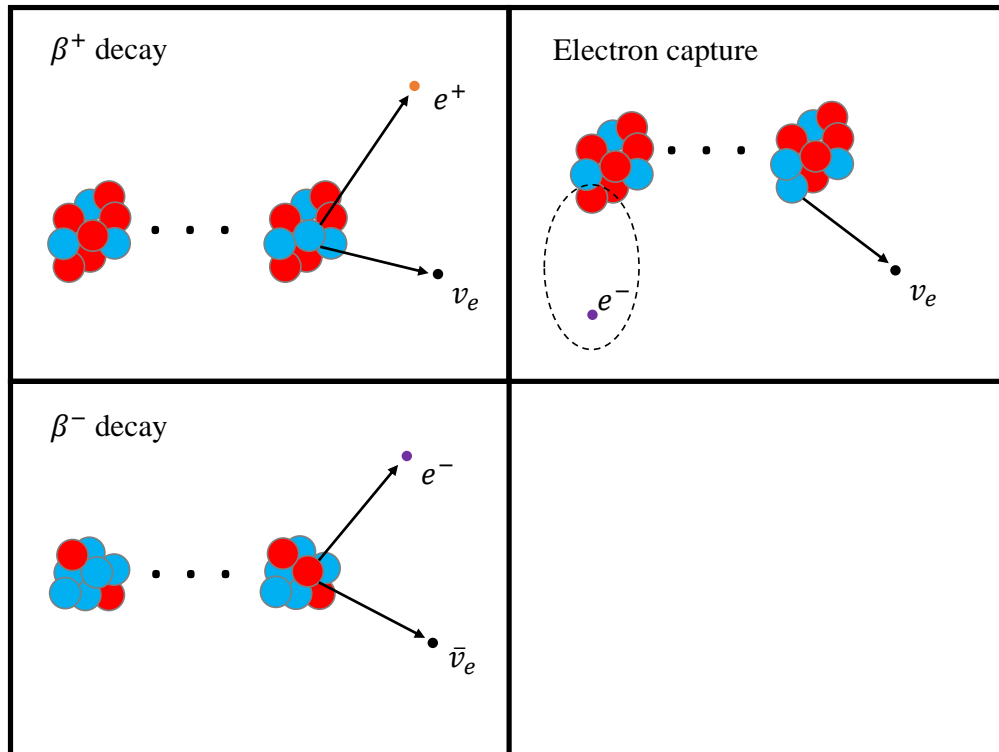


Figure 1.6: An illustration of the three β decay processes: β^- decay is depicted in the top panel while β^+ decay and electron capture are depicted in the bottom left and bottom right panels, respectively.

known, unstable nuclei are converted into stable ones. Unstable nuclei on the proton-rich side of the valley of stability undergo β^+ decay and electron capture while neutron-rich nuclei undergo β^- decay. The electrons or positrons represent the radiation that is easiest to detect from beta decays and were referred to historically as beta rays.

The beta decay processes mentioned in the last paragraph represent a subset of a larger class of transformations that involve quarks and leptons (21). The elementary processes involved in nuclear beta decay are

$$u \rightarrow d + W^+ \rightarrow d + e^+ + \nu_e \quad (1.6)$$

$$d \rightarrow u + W^- \rightarrow u + e^- + \bar{\nu}_e \quad (1.7)$$

where u and d are the up and down quarks, respectively and W^\pm are the gauge bosons that mediate the weak interaction. Since nucleons consist of three valence quarks, (u, u, d) for the proton and (u, d, d) for the neutron, the transformation of a proton into a neutron results from the process described by eq. 1.6. Similarly, eq. 1.7 describes the underlying transformation that converts a neutron into a proton. In terms of the standard model, the characteristic radiation associated with beta decay is due to the decay of the W^\pm bosons.

1.3.3 Other Decay Processes

Gamma-decay refers to the process by which a nucleus in an excited state transitions to a lower energy level and emits a photon with energy roughly equal to the energy difference between the initial and final levels. The decay energy is partitioned between the gamma and the recoil of the nucleus, but the recoil energy is ~ 5 eV for a 1 MeV transition in a nucleus with $A = 100$. This is smaller than the energy resolution for a high-purity germanium detector (see Figure 12-9 of Ref. (28)) so it is neglected. The de-excitation process can involve single particle states, multiple nucleon excitations, rotational states or vibrational states (29). The origin of the electromagnetic radiation produced in these transitions can be understood by picturing the transitions as re-organizations of charge and current distributions inside the nucleus. In terms of classical electrodynamics, the temporal dynamics of these distributions will produce radiation. It is useful to write the charge and current distributions in terms of a multipole expansion. A quantum mechanical model can be built from this basic picture by replacing the multipole moments with operators. Various assumptions can be made about the initial and final state wavefunctions in order to calculate a decay rate corresponding to each term in the multipole expansion for a given transition energy.

Nuclear fission is a process in which a nucleus splits into two or more lighter nuclei. One or

more neutrons can also be emitted in this process. Fission can be spontaneous or induced by some reaction, for example, absorption of an incident neutron. Alpha decay (Section 1.3.1) is a special case of fission where one daughter product is ^4He . Fission can be understood using the same model of Coulomb barrier tunneling that was introduced to study alpha decay. The daughter nuclei are assumed to reside in a potential well like the one shown in Figure 1.5. There is some probability of tunneling through the Coulomb barrier, and it is extremely sensitive to the height of the barrier.

1.3.4 Neutron and Proton Emission

The decay processes mentioned so far are the primary methods by which bound, unstable nuclei are converted into stable nuclei. Beyond the driplines and/or at high enough excitation energies, neutron or proton emission are possible decay channels. The decay energy is determined by the absolute value of the separation energy $E_{\text{decay}} = |S_{n,p}|$ because $S_{n,p}$ is negative for unbound nuclei. Figure 1.7 plots the calculated lifetime as a function of decay energy for a neutron-unbound nucleus and two proton-unbound nuclei. Qualitatively, the half-life for the neutron/proton emission will be determined by the barrier created by the interaction between the emitted particle and the daughter nucleus. The height of the barrier is determined by the decay energy, the angular momentum of the neutron/proton, and, for proton emission, the Coulomb interaction. Neutron emission is inhibited only by the angular momentum barrier so half-lives are orders of magnitude shorter than proton emission for decay energies $\lesssim 100$ keV. To summarize the discussion from Section 1.2.3, special cases of neutron/proton emission for which $T_{1/2} \gtrsim 10^{-14}$ s will be referred to as radioactivity.

1.3.4.1 One- and Two-Proton Radioactivity

The combination of Coulomb and angular momentum barriers results in potentially long half-lives for proton emission (see Figure 1.7), and this process can successfully compete with other decay processes (β^+ , α) in certain cases. In these cases, the half-life is long enough to qualify as proton radioactivity. This process occurs in odd- Z nuclei beyond the proton dripline. It was first observed from an isomeric state in ^{53}Co in 1970 (30). Proton radioactivity from the ground state of ^{151}Lu

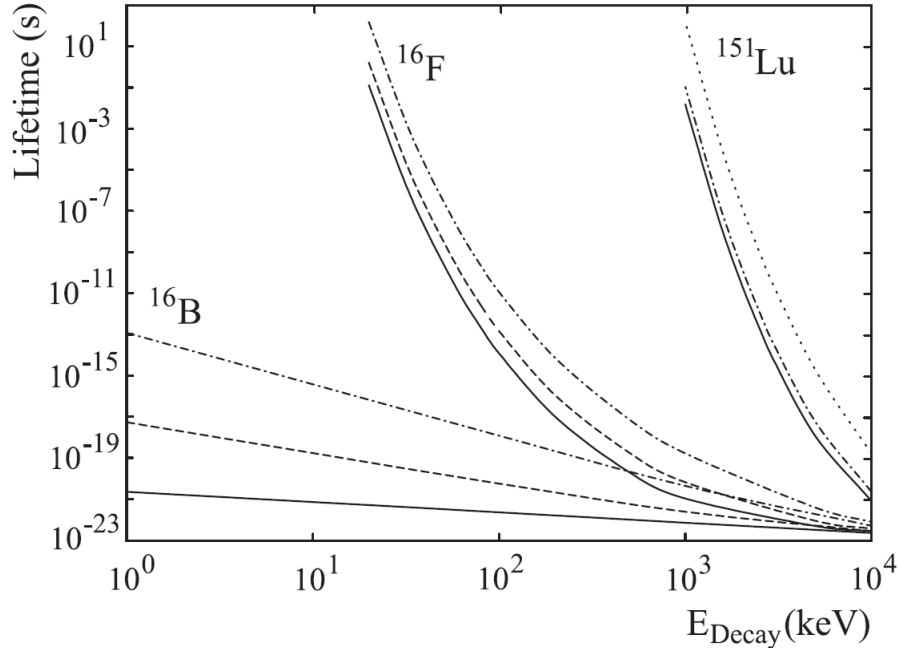


Figure 1.7: Calculated lifetimes for a neutron emitter, ^{16}B , and two proton emitters, ^{16}F and ^{151}Lu , as a function of decay energy for angular momenta $L = 0$ (solid lines), $L = 1$ (dashed lines), $L = 2$ (dash-dotted lines), $L = 5$ (dotted lines). Image from (22).

was first reported in 1982 (31). There are more than 40 known proton emitters including emission from long-lived isomeric states.

Two-proton ($2p$) emission was first suggested by Zeldovich and Goldansky in 1960 (32; 33). Experimental studies of light $2p$ unbound systems ^6Be (34; 35), ^{12}O (36; 37), and ^{16}Ne (36) uncovered states with broad widths corresponding to $2p$ decay half-lives too short to be classified as radioactivity. The short half-lives in these cases result from the low Coulomb barrier for these systems. The first observation of $2p$ radioactivity was reported for ^{45}Fe with $T_{1/2} = 3.2^{+2.6}_{-1.0}$ ms (38). See Ref. (23) and references therein for detailed reviews of one-proton and two-proton radioactivity.

1.3.4.2 Prospects for Two-Neutron Radioactivity

One- or multiple-neutron emission from a neutron-unbound nucleus has been observed for twenty different cases, see Table 16.1 in Ref. (24). In particular, two-neutron emission has been observed from ^{10}He (see Chapter 2 of Ref. (39) for a summary of the ^{10}He measurements), ^5H , (40; 41; 42),

^{13}Li (43; 44), ^{16}Be (45), and ^{26}O (46; 47; 48). A width ~ 1 MeV for the ^5H ground state has been extracted from various measurements of ^HH , see Table I in Ref. (49). This corresponds to $T_{1/2} \sim 10^{-22}$ s which is too short to be considered radioactivity. Extracting a width from the ground state measurements of ^{13}Li and ^{16}Be is precluded by the experimental resolution. Theoretical calculations presented in Ref. (50) suggested that ^{26}O is currently the best candidate for observing $2n$ radioactivity, see the discussion in Section 2.2.3, and the experiment to attempt this observation is the subject of this dissertation.

1.4 Dissertation Overview

The experiment described here utilized a new segmented target system to produce two-neutron-unbound ^{26}O from a ^{27}F beam at the National Superconducting Cyclotron Laboratory. The half-life for the ground state of ^{26}O was extracted from measurements of the decay products, and the performance of the segmented target system was evaluated. This document is organized as follows: Chapter 2 presents the motivations for this experiment, Chapter 3 describes the detector systems used to collect data, Chapter 4 discusses the methods and procedures used to analyze the data, Chapter 5 presents the results, and final remarks and conclusions are given in Chapter 6.

CHAPTER 2

BACKGROUND AND MOTIVATION

The purpose of this experiment was two-fold. First, a measurement of the half-life for the decay of the ^{26}O ground state could determine if this decay qualifies as two-neutron radioactivity. The second goal was an evaluation of the new segmented target system. This chapter discusses these two motivating factors. First a brief summary of previous ^{26}O measurements is given followed by an overview of the theoretical motivations for a half-life measurement on this neutron-unbound system. A final section discusses the motivations for building the segmented target.

2.1 Previous Experiments

The non-observation of ^{26}O in experiments (51; 52; 52; 53; 54) dating back to 1990 suggested that this oxygen isotope is unbound. The MoNA Collaboration reported the first observation (46) of the unbound ^{26}O ground state. The experiment used invariant mass spectroscopy to measure the decay energy of the $^{24}\text{O} + 2n$ system and provided definitive evidence establishing the particle-instability of ^{26}O . The best fit to the decay energy spectrum included a resonance for the ^{26}O ground state at 150_{-150}^{+50} keV above the $2n$ separation energy for ^{24}O . The fit was insensitive to the width of this resonance. The distribution of relative speeds between neutrons and ^{24}O fragments $|\vec{v}_n| - |\vec{v}_f|$ was analyzed to extract a half-life of $4_{-1.5}^{+1.1}$ (stat) ± 3 (syst) ps at an 82% confidence level, and these results were reported in a subsequent publication, Ref. (1). A description of the method used for the half-life analysis is given in Ref. (55) and Section 3.10.

The $^{24}\text{O} + 2n$ system has also been measured using the R3B-LAND setup at GSI. The results reported in Ref. (47) give an upper limit of 120 keV for the ^{26}O ground state and an upper limit of 5.7 ns for its lifetime, both at a 95% confidence level. An experiment using the SAMURAI spectrometer and NEBULA at RIKEN measured ^{26}O with the highest statistics to date (48). The ground state was found to lie 18 ± 3 (stat) ± 4 (syst) keV above the $2n$ separation energy of ^{24}O . In addition, the first 2^+ state was observed at $1.28_{-0.08}^{+0.11}$ MeV above threshold.

2.2 Theoretical Background

2.2.1 Two-body decay

The decay of a parent system into two daughter particles $M \rightarrow m_1 + m_2$ is a simple process where the energy sharing between the daughters is uniquely determined. In its rest frame, the parent has four-momentum $(M, \vec{0})$ and the daughters have

$$P_{1,2} = (E_{1,2}, \vec{p}_{1,2}), \quad E_{1,2}^2 = m_{1,2}^2 + p_{1,2}^2 \quad (2.1)$$

Momentum conservation in the M rest frame implies the daughters' 3-momenta are equal and opposite.

$$\vec{p}_1 = -\vec{p}_2 \quad (2.2)$$

Squaring both sides of 2.2 and using the relation $p^2 = E^2 - m^2$,

$$E_1^2 - m_1^2 = E_2^2 - m_2^2 \quad (2.3)$$

The second equation needed to solve for E_1, E_2 is the conservation of energy $M = E_1 + E_2$. With these two relations, the daughter energies can be expressed in terms of the rest masses of the particles,

$$E_1 = \frac{M^2 + m_1^2 - m_2^2}{2M}, \quad E_2 = \frac{M^2 + m_2^2 - m_1^2}{2M} \quad (2.4)$$

2.2.2 Three-body decay

In contrast to a two-body decay, the energy partitioning among daughter particles in a three-body decay is not uniquely determined. For example, in the case of nuclear β -decay, a distribution of β -particle energies will be observed instead of a single value like in the case of α -decay. Such an observation prompted Wolfgang Pauli to postulate the existence of the electron neutrino, thus

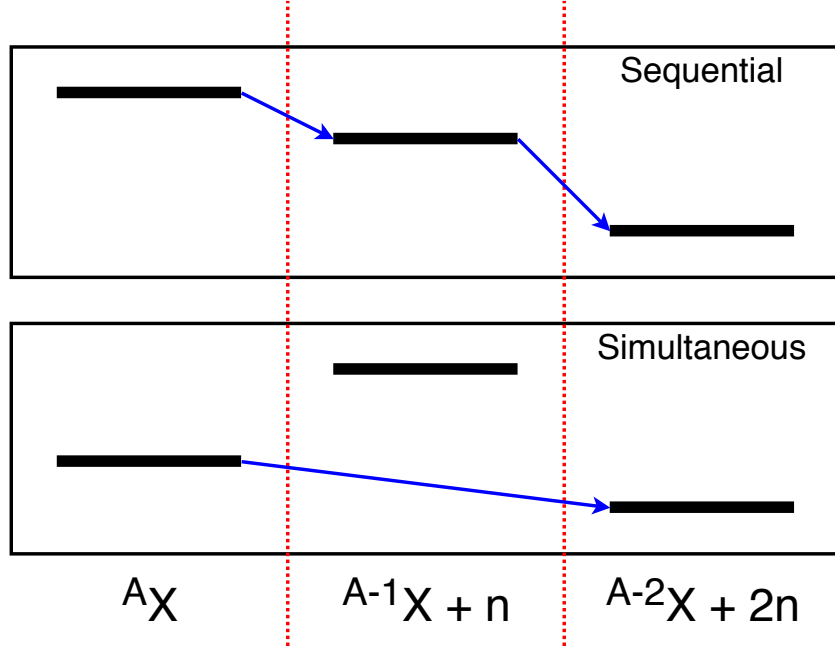


Figure 2.1: Illustrations of the energy conditions characteristic of sequential (top panel) and simultaneous (bottom panel) three body decays.

describing β -decay as a three-body process (56). Nevertheless, the energies and rest masses of the parent and daughter particles do restrict the allowed phase space of the kinematical variables. For example, the maximum allowed momentum for each daughter particle can be calculated in the rest frame of the parent

$$p_{i \max} = \frac{1}{2M} \sqrt{[M^2 - (m_i + m_j + m_k)^2][M^2 - (m_j + m_k - m_i)^2]}$$

where M is the rest mass of the parent and m_{ijk} are the rest masses of the daughters. A cyclic permutation of the indices i, j, k gives p_{\max} for the other particles j, k . For a complete derivation of this and other kinematical limits for three-body decay the reader is referred to Ref. (57).

2.2.3 $2n$ Decay of ^{26}O

Three body decays can be characterized by either simultaneous or sequential particle emission depending on the relative spacing of energy levels in the parent, intermediate and daughter nuclei, see Figure 2.1. The energy conditions for simultaneous (also called true) two-particle decay make

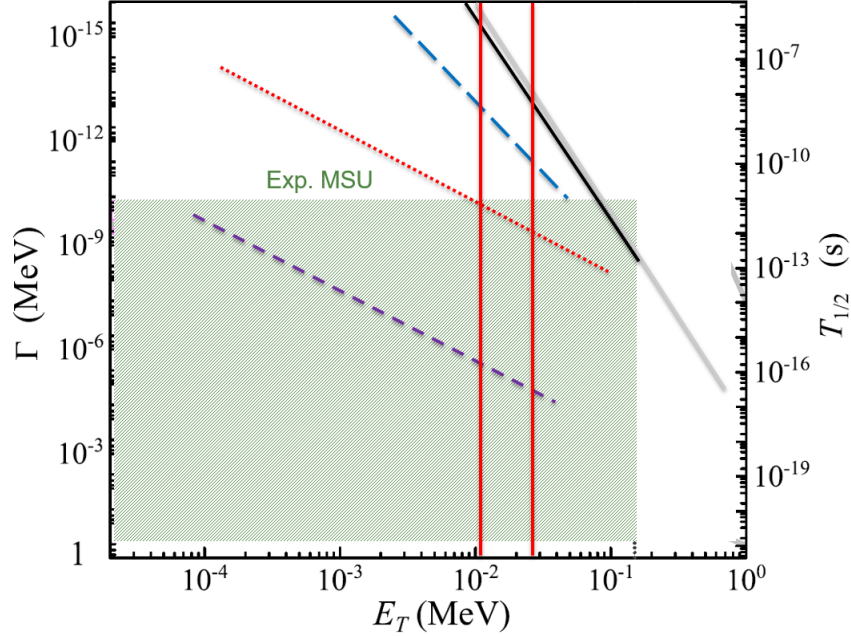


Figure 2.2: Decay width/half-life as a function of decay energy for $2n$ emission from ^{26}O . The gray line assumes a pure orbital [d^2] configuration coupled to the total angular momentum $L = 0$. The solid black curve shows the results for the no FSI, infinite ^{24}O mass. The blue dashed line plots the results for the no FSI calculation. The red dotted line is the calculation with the $n - n$ FSI scaled by 0.25, and the purple short-dashed curve is the full $n - n$ FSI results. The vertical red lines roughly indicate the experimental results from (48). Image adapted from (58).

the emission of a single particle energetically impossible. The requirement that two particles be emitted simultaneously results in longer lifetimes compared to a sequential decay (50).

The ^{26}O ground state was identified as a promising candidate for observing $2n$ radioactivity based on three criteria:

1. a sequential decay through ^{25}O is energetically unfavorable
2. the decay energy is low
3. the angular momentum barrier is maximized since the two valence neutrons are expected to occupy the $0d_{3/2}$ orbital (59; 60)

All of these factors contribute to the effective barrier through which the neutrons have to tunnel which increases the lifetime of the nucleus.

Results from a theoretical model for the $2n$ decay of ^{26}O were presented in (58). The model was adapted from the three-body hyperspherical harmonics cluster model used to study $2p$ radioactivity (61), and it incorporated the experimental information about ^{26}O (46; 47) and ^{25}O (62) that was available at the time. The model calculates a decay width by solving Schrödinger’s equation for a three-body Hamiltonian that describes the ^{24}O cluster and two neutrons. A Gaussian form for the $n - n$ potential was used, and a Woods-Saxon potential was used for the $^{24}\text{O} - n$ potential. The decay width was calculated assuming

1. no $n - n$ final state interaction (FSI) and an infinite mass for ^{24}O
2. no $n - n$ FSI and the correct mass for ^{24}O
3. the $n - n$ FSI scaled by 0.25
4. the full $n - n$ FSI

The results of these calculations are shown in Figure 2.2. Each of these successive approximations decreases the estimated half-life by orders of magnitude. Reducing the uncertainty in the experimental measurement would help inform the theoretical model used to interpret the microscopic dynamics of this decay process.

2.3 The Unbinned Loglikelihood

This section summarizes the method of maximum loglikelihood (LnL) for parameter estimation and statistical uncertainty calculation following the treatment given in Ref. (63). A variation of this method was used in the present analysis. Note that the discussion here follows the convention of standard statistical analysis texts and refers to maximizing the LnL function. However, to be consistent with the previous published work, the analysis discussed later uses the convention of minimizing the negative LnL. The methods are the same for both conventions and differ only by a sign.

Consider a random variable x that has been measured n times in some experiment. Suppose that x is known to be distributed according to some probability density function (p.d.f.) $f(x, \theta)$

with known form but (for simplicity) one unknown parameter θ . Then the probability that each measurement x_i lies in the range $[x_i, x_i + dx_i]$ can be written

$$P = \prod_{i=1}^n f(x_i; \theta) dx_i$$

and P will be at a maximum for the correct choice of the parameter θ . Furthermore, the parameters are independent of each dx_i which permits definition of the likelihood function

$$L(\theta) = \prod_{i=1}^n f(x_i; \theta)$$

When $L(\theta)$ has a simple analytic form, the usual prescription for maximizing a function can be followed, namely finding $\hat{\theta}$ such that

$$\left(\frac{dL}{d\theta} \right)_{\theta=\hat{\theta}} = 0.$$

This solution is referred to as an estimator, denoted as $\hat{\theta}$, for the true parameter θ . When there is no analytic form, numerical methods must be used to calculate $L(\theta)$ and find its maximum.

It is convenient to take the logarithm of the likelihood function as this converts the product of terms into a sum and exponents into multiplicative factors.

$$\ln L(\theta) = \sum_{i=0}^n \ln f(x_i; \theta) \tag{2.5}$$

Since the logarithm is a monotonically increasing function, the value of θ that maximizes $L(\theta)$ will also maximize $\ln L(\theta)$.

The second derivative of $\ln L(\theta)$ can be used to determine the variance of an estimator $\hat{\theta}$:

$$\widehat{\sigma^2}_{\hat{\theta}} = \left(-1 \left/ \frac{\partial^2 \ln L(\theta)}{\partial \theta^2} \right)_{\theta=\hat{\theta}} \right) . \tag{2.6}$$

In cases where the likelihood function has no analytic form it can be useful to employ a graphical method for obtaining the variance of an estimator. To understand how this works consider a Taylor expansion of $\ln L(\theta)$ about the minimum $\theta = \hat{\theta}$

$$\ln L(\theta) = \ln L(\hat{\theta}) + \left(\frac{\partial \ln L(\theta)}{\partial \theta} \right)_{\theta=\hat{\theta}} (\theta - \hat{\theta}) + \frac{1}{2!} \left(\frac{\partial^2 \ln L(\theta)}{\partial \theta^2} \right)_{\theta=\hat{\theta}} (\theta - \hat{\theta})^2 + \dots$$

Since $\hat{\theta}$ corresponds to a maximum, $\ln L(\hat{\theta}) = \ln L_{\max}$ and the second term is 0. Neglecting terms higher than second order, eq. 2.6 can be used to re-write the expansion as

$$\ln L(\theta) = \ln L_{\max} - \frac{(\theta - \hat{\theta})^2}{2\widehat{\sigma}_{\hat{\theta}}^2} \quad (2.7)$$

Changing the argument θ by N standard deviations can be expressed as $\theta \rightarrow \hat{\theta} \pm N\hat{\sigma}_{\hat{\theta}}$ and eq. 2.7 becomes

$$\ln L(\hat{\theta} \pm \hat{\sigma}_{\hat{\theta}}) = \ln L_{\max} - \frac{N^2}{2}$$

2.4 Fragment momentum reconstruction and decay energy resolution

Invariant mass spectroscopy (Section 3.9) experiments to study neutron unbound states are based on radioactive ion beams (RIBs) produced via in-flight projectile fragmentation. The intensity of the fragment beam can be $\sim 10 - 1000$ particles/s (64; 65). The beam is then directed onto the reaction target to induce a one- or two-proton knockout reaction. Typical cross-sections for these knockout reactions are ~ 1 mb and ~ 0.1 mb, respectively (66). Thus certain experiments at the limit of feasibility would greatly benefit from any method that increases reaction yield.

One way to increase reaction yield is to use a thicker target to increase the number density of target nuclei. However, this approach negatively impacts the resolution of the decay energy measurement. A key component that influences the decay energy resolution is the reconstruction of the fragment momentum at the decay vertex. The decay process occurs inside the target material due to its $\sim 10^{-22}$ s time scale. The charged daughter fragment loses energy as it travels through the rest of the target, therefore any subsequent measurement of its momentum will yield a lower value than at the decay vertex. To recover the vertex momentum, the energy lost to the target material must be added back. The decay energy resolution is directly impacted by how well the

energy addback can be estimated which in turn depends on how well the location of the decay is measured.

By using an active target in which the decay position and/or energy lost by the fragment is measured, one could directly measure the energy addback event-by-event. In current active target systems the fill gas acts as both the target and detector material (67; 68; 69; 70). However, to produce the same reaction rate as a 1 cm thick solid beryllium target, an active target filled with an ideal gas would need to be 10^7 m long and operate at 500 kPa (~ 5 atm). This estimate assumes identical reaction cross-sections for beryllium and the ideal gas.

A compact solution is a system composed of multiple solid, thin targets interleaved with energy loss detectors. This system localizes the decay position to one of the target sections which allows for a better approximation of the energy loss through the detector system than for a single thick target. When silicon detectors are used to measure the energy loss, the incident beam rate is limited to ~ 1000 particles per second to avoid pileup and excessive radiation damage.

In summary, segmenting a single thick target offers improved energy resolution because the decay position can be better localized so that the energy addback can be better approximated.

CHAPTER 3

EXPERIMENTAL TECHNIQUE

The experiment described here was performed at the National Superconducting Cyclotron Laboratory (NSCL) between 30 June and 7 July 2016 using the newly developed segmented target, the Modular Neutron Array (MoNA), the Large-area multi-Institutional Scintillator Array (LISA) and the Sweeper magnet. In its first section, this chapter provides an overview of the experimental setup, then it describes the beam production and downstream detectors in detail in the following sections.

3.1 Experimental Setup

A 140 MeV/u ^{48}Ca beam impinged on a 775 mg/cm² Be target to produce a secondary beam of ^{27}F via projectile fragmentation. The A1900 fragment separator was used to select ^{27}F at an energy of 106.2 MeV/u from other products of the fragmentation reaction. This secondary beam was delivered to the experimental area in the N2/N3 vault where it was directed onto a series of position sensitive silicon detectors and beryllium targets, the segmented target. The average ^{27}F beam rate on the target was 17 particles per second.

The reaction of interest for this experiment was a one-proton removal from ^{27}F to produce unbound ^{26}O which then decays through two-neutron emission. The Sweeper magnet sat behind the segmented target and bent the charged ^{24}O fragments into a suite of charged particle detectors inside the Sweeper focal plane box. Two cathode-readout drift chambers (CRDCs), an ionization chamber and a thin timing scintillator were located inside the focal plane box.

The neutrons continued in the general direction of the beam. Unaffected by the magnetic field, they exited the Sweeper vacuum chamber and traveled through air until they interact with the plastic scintillators that comprise the MoNA/LISA arrays. These arrays were arranged in 17 layers with each layer consisting of 16 bars stacked on top of one another. The layers were arranged in groups of two or three across three support tables. All layers were centered on the beam axis. Prior

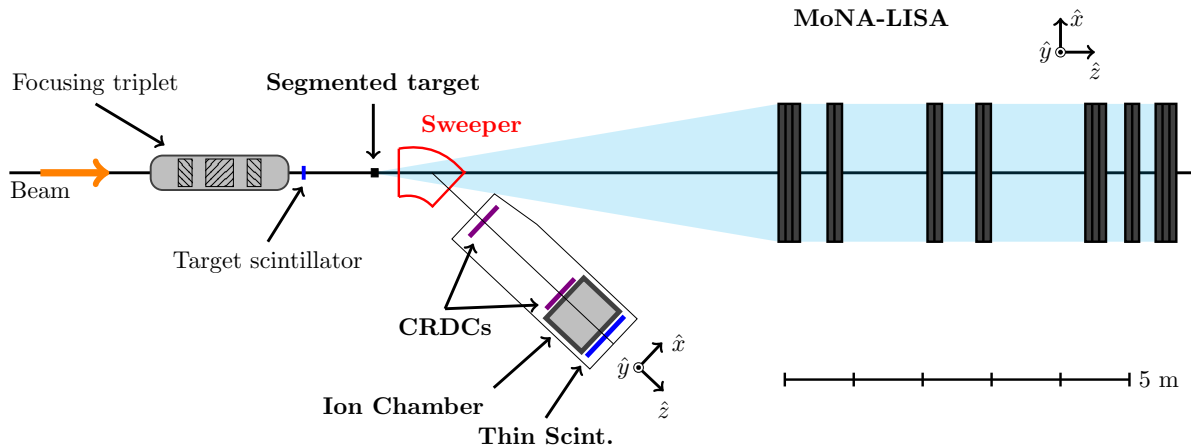


Figure 3.1: Detector layout in the N2 vault.

to the experiment, the eighteenth layer was removed from the experimental area to be used in an experiment at the Los Alamos Neutron Science Center (71).

The Sweeper focal plane detectors and the MoNA/LISA arrays allow for a kinematically complete measurement of the charged fragments and neutrons to which the method of invariant mass spectroscopy (Section 3.9) can be applied to recover information about the unbound ^{26}O nucleus. For this experiment, the difference in magnitude between the neutron and fragment velocities $|\vec{v}_n| - |\vec{v}_f|$ was analyzed to look for a signature that the ^{26}O existed for some measurable amount of time before the two-neutron emission.

3.2 Beam Production

The Coupled Cyclotron Facility (72) and the A1900 fragment Separator (73) provided the ^{27}F beam via fast projectile fragmentation (74). Since ^{27}F has a half-life of 5.0(2) ms (75) it cannot be accelerated directly and must be produced in flight, in this case, via fragmentation of ^{48}Ca on ^9Be .

A stable ^{48}Ca beam was accelerated to 140 MeV/u in the coupled K500 and K1200 cyclotrons then directed onto a 775 mg/cm^2 Be target where the fragmentation occurred. A wide variety of nuclei were produced by this process. The A1900 was used to extract ^{27}F from the fragmentation products. The A1900 has four dipole magnets with focusing elements in between them to filter nuclei by their magnetic rigidity and select a specific momentum to charge ratio. An achromatic

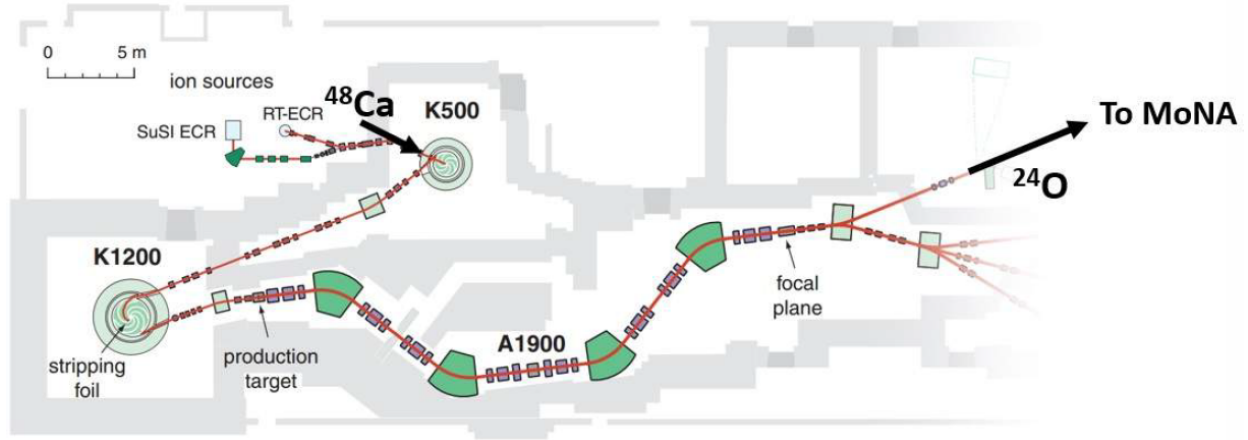


Figure 3.2: Beam production at the Coupled Cyclotron Facility starts by heating a sample of the primary beam material in an ion source. The K500 and K1200 cyclotrons accelerate the beam which is subsequently directed onto a Be target. Fragments resulting from nuclear interactions within the target are filtered by the A1900 to provide the desired secondary beam. Image source: (76).

aluminum wedge with thickness 450 mg/cm^2 was placed at the dispersive mid-plane between the second and third dipoles to improve separation; the energy loss in the wedge is proportional to Z^2 so different elements entering the wedge with the same rigidity exit with different rigidities. The ^{27}F was then delivered to the experimental vault with an energy of 106.2 MeV/u corresponding to a rigidity of 4.58 Tm . Three major contaminants (1) ^{28}Ne ($E = 121.5 \text{ MeV/u}$) (2) ^{29}Ne ($E = 113.6 \text{ MeV/u}$) (3) ^{30}Na ($E = 127.7 \text{ MeV/u}$) arrived with the same rigidity. It should be noted that the beam was delivered at a higher rigidity than the Sweeper can accommodate. However, the increased (relative to previous MoNA experiments) target thickness means that unreacted beam and reaction products enter the Sweeper below its 4 Tm limit.

3.3 A1900 and Target Scintillators

A plastic timing scintillator is located at the focal plane of the A1900 fragment separator 10.9 m upstream from the segmented target. For this experiment, the A1900 scintillator was a $144 \mu\text{m}$ thick BC-400 scintillator optically coupled to a PMT. The target scintillator (see Figure 3.1) was located 1.03 m upstream from the segmented target and consisted of a $420 \mu\text{m}$ thick BC-404 scintillator coupled to a PMT. In both cases, the charged ions passing through the plastic excite

molecules that de-excite producing photons. The photons that reach the PMT are converted into an electrical signal. The signal rise times are ~ 1 ns, so the time at which the ion passes through the plastic can be marked with a resolution ~ 1 ns. With the information from the two timing scintillators, an ion's time of flight from the A1900 to the N2 vault was measured.

3.4 Segmented Target

Section 2.4 discussed how segmenting a single thick solid target offers improved energy resolution because the decay position can be better localized so that the energy addback can be better determined. The following subsections detail the setup and electronics of the segmented target system used during this experiment.

3.4.1 Silicon Detectors and Beryllium Targets

The segmented target consists of four position-sensitive silicon detectors and three beryllium targets arranged as shown in Figure 3.3. Each silicon detector is a $62 \text{ mm} \times 62 \text{ mm} \times \sim 140 \mu\text{m}$ phosphorus-doped n-type silicon wafer. The front face is a boron-implanted p-type layer resistive anode and is bordered by 0.5 mm resistive ion-implanted strips. The resistances between adjacent corners is $\sim 5.6 \text{ k}\Omega$. Aluminum contacts at each corner provide electrical connections that read out the four signals which can be used to reconstruct the interaction position. A fifth signal is taken from the rear face non-resistive layer via an aluminum-evaporated contact to provide an independent measurement of the total energy deposited with better resolution than can be obtained from the sum of the corner signals.

The thicknesses of the three beryllium targets were chosen to optimize the production rate of the nucleus of interest and decay energy resolution. The linear thicknesses and area densities of the beryllium and silicon targets are listed in Table 3.1.

Segment	Thickness [μm]	Area Density [mg/cm^2]
Si 0	140	32.5
Be 1	4100	758.5
Si 1	135	31.3
Be 2	3736	691.2
Si 2	138	32.0
Be 3	3302	610.9
Si 3	142	33.0

Table 3.1: Thicknesses for the silicon detectors and beryllium targets. The beryllium targets were measured directly using calipers with a dial indicator and the associated measurement uncertainties are $\pm 4 \mu\text{m}$ ($\pm 0.7 \text{ mg}/\text{cm}^2 \text{ Be}$). The silicon wafer thicknesses were reported by the manufacturer with uncertainties of $\pm 1 \mu\text{m}$ ($\pm 0.2 \text{ mg}/\text{cm}^2 \text{ Si}$).

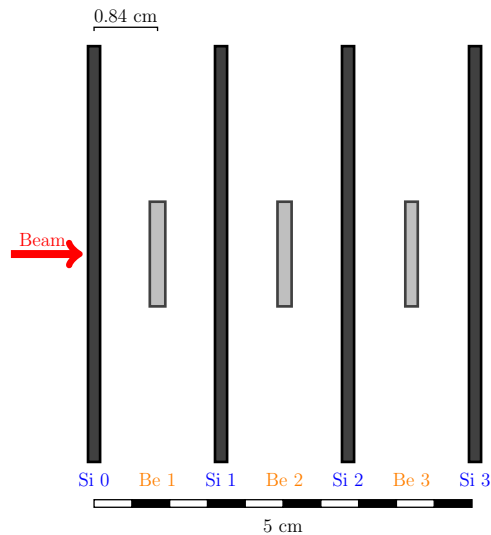


Figure 3.3: Each detector is $11 \text{ cm} \times 11 \text{ cm} \times 0.32 \text{ cm}$ including the frame housing the silicon wafer. The thicknesses of the silicon wafers are $140 \mu\text{m}$, $135 \mu\text{m}$, $138 \mu\text{m}$, and $142 \mu\text{m}$ for detectors 0, 1, 2, and 3, respectively. The beryllium targets are 2.8 cm tall with thicknesses of 0.41 cm , 0.37 cm , and 0.33 cm for targets 1, 2, and 3, respectively. The spacing between each detector/target is 0.84 cm (0.33 inches) so in total the apparatus extends 5.04 cm along the beam axis.

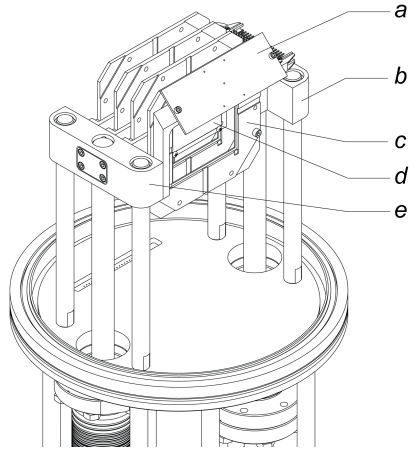


Figure 3.4: Drawing of the segmented target mounted in the beamline: (a) beam viewer plate used to image the beam during tuning (b) base on which all detectors are mounted (c) silicon detector frame (d) beryllium target (e) base on which all targets are mounted. The viewer is mounted to the target base. Both the detector and target mount bases are attached to pneumatic drives so they can be individually inserted into and retracted from the beamline.

3.4.2 Signal readout and electronics

The four silicon detectors generate 20 signals consisting of 16 corner signals and 4 anode signals. The signals from the aluminum contacts mentioned previously are carried by AWG 28 wire to a custom-made PCB board (one for each detector) that subsequently routes the five signals from each detector to a specific section of a 60-conductor ribbon cable.

Each anode signal is routed to a preamplifier that has a typical output signal around 30 mV with a $0.05 \mu\text{s}$ rise time and a $500 \mu\text{s}$ fall time when a 5.5 MeV α source was placed 7.1 cm in front of the detector under vacuum. The anode signals are then routed to a Tennelec 241S shaping amplifier with a shaping time of $6 \mu\text{s}$. The shaped anode signals are routed to a Mesytec MADC-32 analog-to-digital converter with a 4 V range.

Each corner signal is floated above ground by a $10 \text{ k}\Omega$ resistor on the PCB. The corner signals are routed to one of 16 Mesytec MMPR1 preamplifiers. The corner signals are some fraction of the anode signal depending on the interaction location of the passing ion. The preamplifier outputs are connected to a single 16-channel Mesytec MSCF-16 shaping amplifier. The shaping time is $2 \mu\text{s}$ for all corner channels. The shaped signals are routed to a bank of 16 inputs on the same

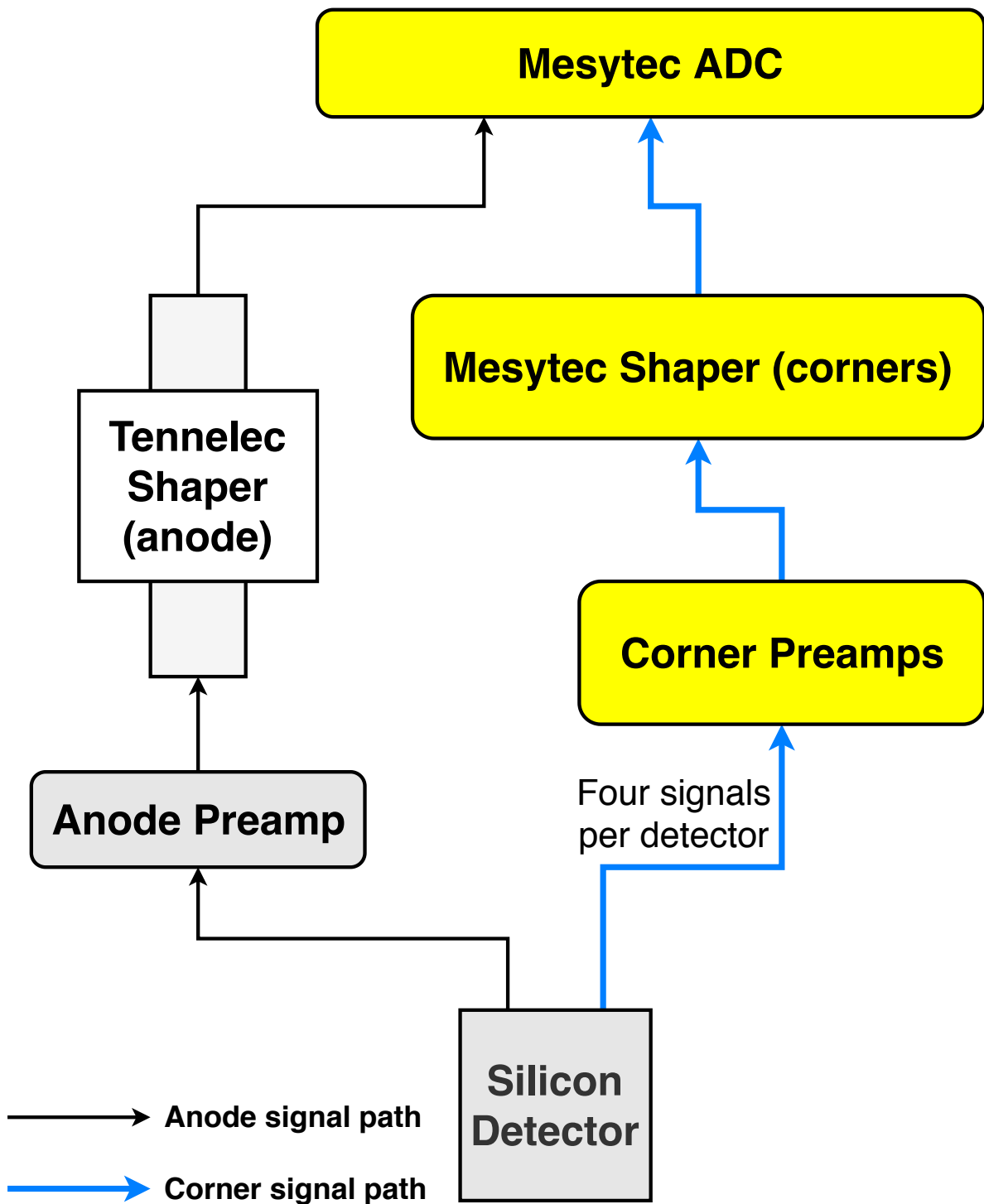


Figure 3.5: Wiring diagram showing the signal paths for the anode and corner signals from one of the silicon detectors. The anode (black arrows) and corner (blue arrows) signals were routed through separate preamp and shaping amplifiers. All shaped signals were processed by the same analog-to-digital converter.

MADC-32 that receives the anode signals.

3.5 Sweeper magnet

The Sweeper magnet is a large-gap superconducting dipole magnet with a bending radius of approximately 1 meter and a bending angle of 43.3° (77). The magnetic field is monitored using a Hall probe and has been mapped in previous work (78). For this experiment, the magnet was set to a current of 306 A which corresponded to a central rigidity of 3.445 Tm, which was the expected rigidity of ^{24}O fragments produced from the ^{27}F beam. In general, unreacted beam, reaction fragments and neutrons all exit the target in a forward-focused cone. The Sweeper magnet bends the charged particles away from the neutron flight path and into a suite of charged particle detectors (described in the next section). The neutrons continue along the beam axis through a vertical gap of 14 cm and into the neutron detectors (described in Section 3.7).

3.6 Charged Particle Detectors

Immediately downstream from the Sweeper magnet was a collection of charged particle detectors contained in a large vacuum box. The positions of reaction products deflected by the magnet were measured in two Cathode Readout Drift Chambers (CRDCs) separated by 1.54 m. Behind the CRDCs sat an ionization chamber to measure energy loss followed by a large area plastic scintillator to determine particle timing.

3.6.1 CRDCs

The distance from the target to the first CRDC was 1.86 m measured along the arc of the central trajectory through the magnet. The second CRDC was positioned $\Delta z = 1.54$ m downstream from the first. The CRDCs measure the x and y positions of particles passing through their volumes. The angle in the xz plane between the particle's trajectory and the z -axis can be calculated from the two x measurements and the known distance between the CRDCs $\tan \theta_x = (x_2 - x_1)/\Delta z$. A similar calculation using the two y measurements gives an angle θ_y with respect to the z -axis in

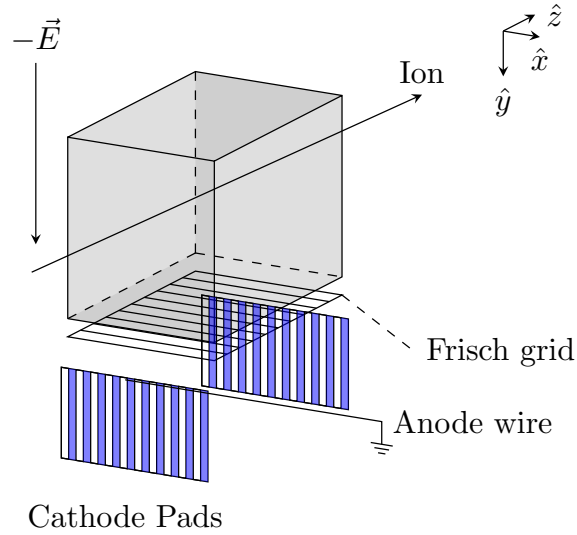


Figure 3.6: Schematic of a Cathode Readout Drift Chamber (CRDC) expanded in the z -direction. The field shaping wires are omitted for visibility.

the yz plane. These angles can be used to trace the particle's path back through the magnet to the target. A schematic of the detector is shown in Figure 3.6.

A CRDC functions in a manner similar to that of an ionization chamber. It is filled with a 1:4 mixture of isobutane and CF_4 gas at a pressure of 40 Torr (0.05 atm) and sealed with two windows. When a particle passes through it ionizes the gas and creates ionization pairs that are separated due to a uniform applied electric field. This drift field is produced by a 1000 V potential difference between a plate at the top of the detector and a Frisch grid near the bottom. Field shaping wires parallel to the x -axis are placed at specific intervals in y along each face of the detector. Below the Frisch grid is an anode wire and a series of 116 aluminum cathode pads with a pitch of 2.54 mm in width that run parallel to the x direction.

Electrons drift from the interaction point of the passing particle towards the Frisch grid. As they pass through the Frisch grid they enter a strong electric field created by the anode wire and produce an electron avalanche which is collected at the anode. An induced charge is distributed across the cathode pads, and the x position is extracted from the distribution of this induced charge. The y position is determined from the drift time of the electron which is measured as the difference between a signal in the thin timing scintillator and a signal on the anode wire. The active area of

each CRDC is $30 \times 30 \text{ cm}^2$ in the xy plane.

3.6.2 Ionization Chamber

The ionization chamber is a gas-filled detector similar to a CRDC but with 16 charge collecting pads segmented along the z direction. The active volume of the detector is $40 \times 40 \times 65 \text{ cm}^3$. It is filled with P-10 gas (10% CH_4 and 90% Ar) and held at 400 Torr (0.53 atm). The windows are thin to allow particles to pass through with negligible energy loss; they are made of Kevlar filament and $12 \mu\text{m}$ PPTA and are mounted with epoxy. The upstream window is $30 \times 30 \text{ cm}^2$ to match the acceptance of the CRDC and the downstream window is $40 \times 40 \text{ cm}^2$ to allow for dispersion of the beam.

The ion chamber has a plate on top and 16 charge collecting pads on the bottom. A charged particle passing through the fill gas creates ionization pairs and a drift voltage of 1500 V is applied to collect the ionization pairs. The electrons are collected on the 16 pads at the bottom. The energy lost in the gas is proportional to the total charge collected on the pads.

3.6.3 Thin Timing Scintillator

The thin timing scintillator is mounted just downstream from the ion chamber. It is a plastic scintillator (EJ-204) with dimensions $55 \times 55 \times 5 \text{ cm}^3$ and has four photomultiplier tubes attached via light guides - two along the top edge and two along the bottom edge. It measures time of flight and triggers the data acquisition system. The light guides are trapezoidal and optically connected to the PMTs. A diagram of the thin scintillator is shown in Figure 4.13.

3.7 MoNA LISA

Neutron position and time-of-flight (ToF) measurements were made with the Modular Neutron Array (MoNA) and the Large-area multi-Institutional Scintillator Array (LISA) (79; 80; 66). The MoNA array consisted of 128 Bicron-manufactured BC-408 plastic scintillator bars measuring $200 \text{ cm} \times 10 \text{ cm} \times 10 \text{ cm}$. The LISA array consisted of 144 Eljen EJ-200 plastic scintillator bars

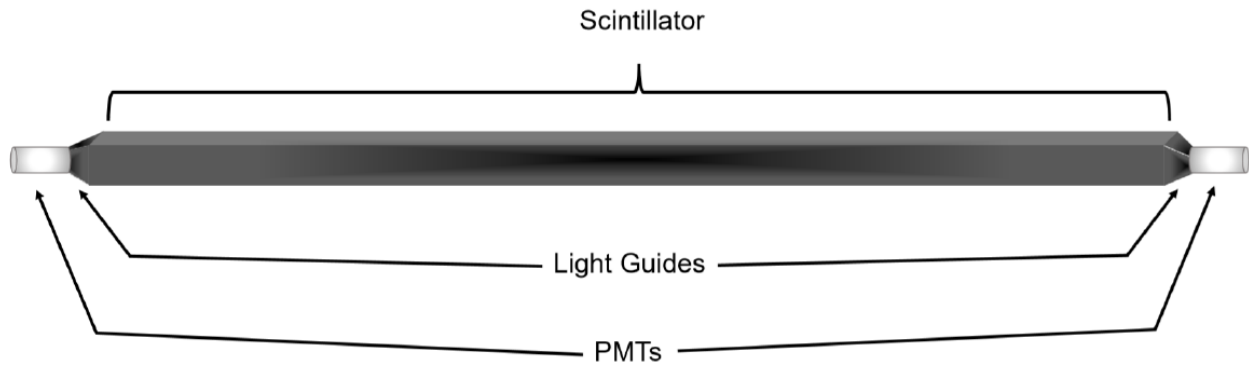


Figure 3.7: Schematic drawing of a single MoNA/LISA plastic scintillator bar. Image source: Ref. (81).

with the same dimensions. The two materials are physically and chemically equivalent. Each bar is wrapped in reflective material to reduce light loss then covered with black plastic to prevent ambient light from inducing signals. A schematic of a single bar is shown in Figure 3.7.

Neutrons are detected in the scintillator bars when they interact with the atomic nuclei in the plastic. The neutron-to-hydrogen mass ratio (~ 1) is roughly an order of magnitude larger than the neutron-to-carbon mass ratio (~ 0.08) so the probability is larger for neutron-hydrogen interactions. Therefore most of the scintillation light is produced in neutron-hydrogen scattering processes; the recoiling proton perturbs the electronic structure of the atoms in the scintillator material resulting in fluorescence as described in Section 3.6.3. The light propagates to both ends of the bar and is collected in photomultiplier tubes (PMTs). MoNA was outfitted with Photonic XP2262/B PMTs and LISA was constructed with Hamamatsu R329-02 PMTs. The PMTs convert the scintillation light to an electronic signal. Each PMT housing has three connectors to accommodate two signal outputs and one high voltage connection. The two output signals are used to measure (1) the time at which an interaction occurs in the bar relative to some trigger signal and (2) the amount of scintillation light produced by the interaction.

MoNA and LISA are modular systems that can be arranged in a variety of ways. For this experiment, 16 bars were stacked one on top of another to form a layer. Seventeen total 16-bar layers were configured as shown in Figure 3.8. Layers were arranged in groups of two or three across three tables. Individual bars were labeled by their Table (LISA-2, LISA-1, MoNA), Layer

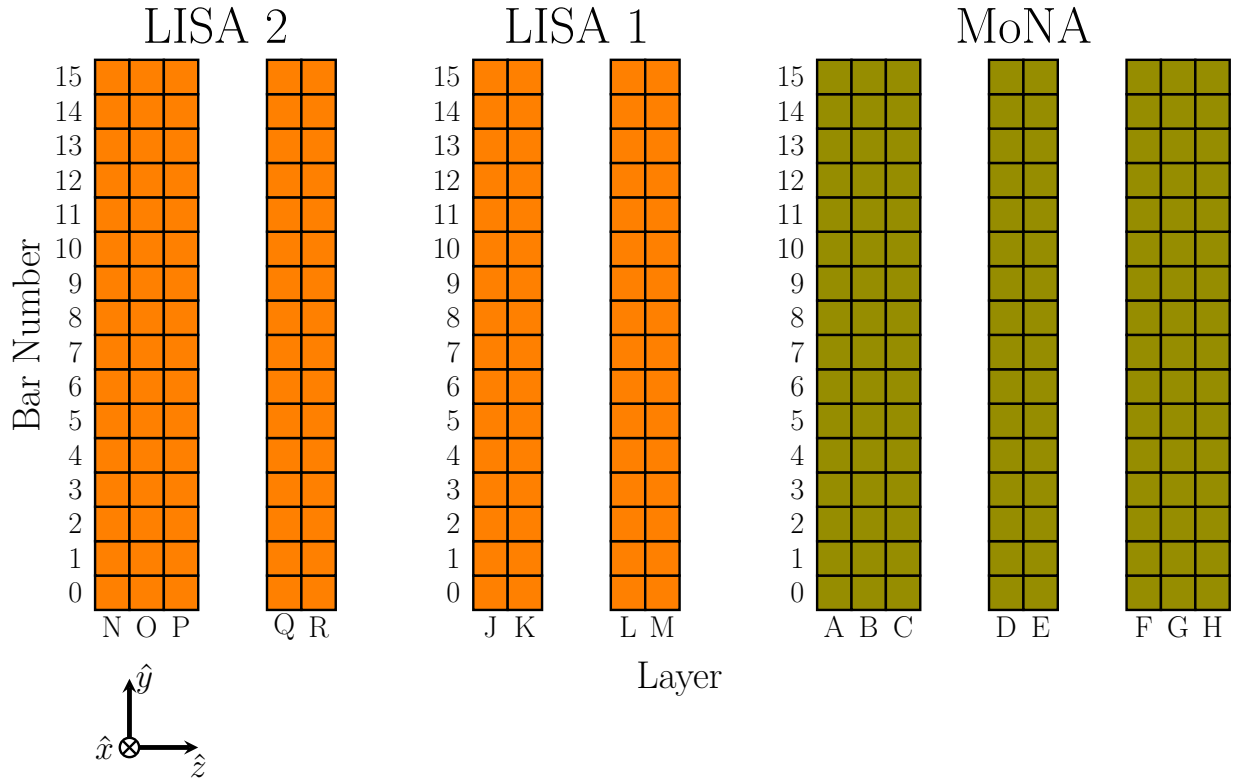


Figure 3.8: A diagram of the spatial ordering of the MoNA/LISA bars as they were configured for this experiment. Neutrons from the target travel from left to right. The spacing between groups of layers is not drawn to scale.

(A, B, C, etc.) and number (0, 1, ..., 14, 15).

Placement of the bars relative to the target is shown in Figure 3.1. The center of the front layer on the most-forward-positioned LISA table was 596 cm from the target; the center of the front layer on the next LISA table was 812 cm from the target. The center of the front MoNA layer was 1041 cm from the target. In the xy plane, each front layer's center was within 3 cm of the theoretical beam axis.

3.8 Electronics and DAQ

The electronics and data acquisition (DAQ) systems are described in detail in References (78; 82; 83). This section gives a brief overview of these systems and describes their settings for this experiment.

MoNA, LISA and the Sweeper detectors operated as three independent subsystems. These

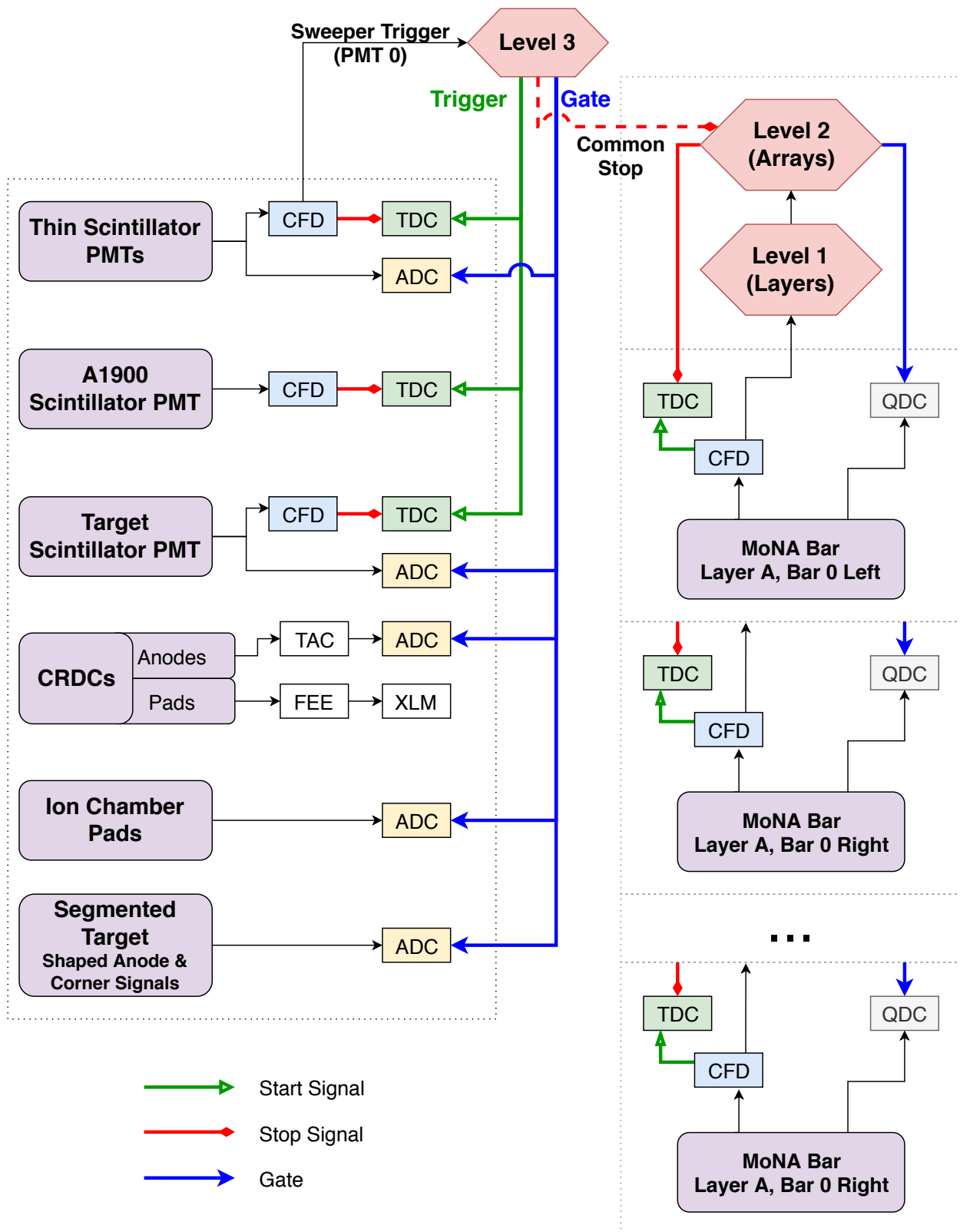


Figure 3.9: Schematic diagram of the MoNA/LISA-Sweeper electronics modified from Reference (81). Start, stop and gate signals are depicted with green, red and blue arrows respectively. The signal used as the common stop for the MoNA/LISA TDCs is indicated by the red dashed line. Shaping amplifiers are omitted for clarity.

subsystems were connected to a “Level 3” logic system that generated a system trigger and an event tag. The Level 3 system generated a trigger when it received a signal from the channel 0 PMT of the thin scintillator. Each event tag was a unique 64-bit number generated by the Level 3 logic and distributed to each of the three subsystems. Each subsystem independently read out its data and the event tag upon receiving the system trigger. The three data sets were merged offline by matching event tags. For this experiment, receiving a signal from the thin scintillator was the only condition for generating a Level 3 trigger. Therefore, data were recorded even if there was no signal from the neutron detectors.

The MoNA and LISA electronics setups were independent but identical. Each PMT output two signals, an “anode” and a “dynode” signal. The dynode signal was routed from the PMT through an inverter into a charge-to-digital converter (QDC) that integrated the charge produced by the PMT to measure the amount of scintillation light that the PMT registered. The anode signal was sent to a constant fraction discriminator (CFD). The CFD output two copies of a logic pulse: one triggered the start of a time-to-digital converter (TDC) and the other was delivered to a logic module (described in the next paragraph). The TDC modules operated in common stop mode where a signal from the CFD started the timer and a signal from the Level 3 logic system stopped the timer. This signal path was replicated for each of the 288 LISA PMTs and 256 MoNA PMTs. Charge and timing information for each PMT was read out from the QDCs and TDCs, respectively, by the DAQ computer through a VME interface.

An overview of the MoNA-LISA-Sweeper electronics setup and signal routing for the Level 3 logic is depicted in Figure 3.9. Programmable Xilinx Logic Modules (XLMs) handled the trigger logic which was divided into three levels. In the first level, one XLM for each layer counted the number of coincident left-right CFD signals in that layer and passed this information up to Level 2. The Level 1 module also sent the integration gate to the layer’s QDCs as soon as the first signal arrived from the CFD. There were two Level 2 XLM modules - one for each array. A Level 2 module collected the left-right coincidence information and if at least one layer had good timing signals in both PMTs on a single bar (the definition of a valid event) the system was prepared to

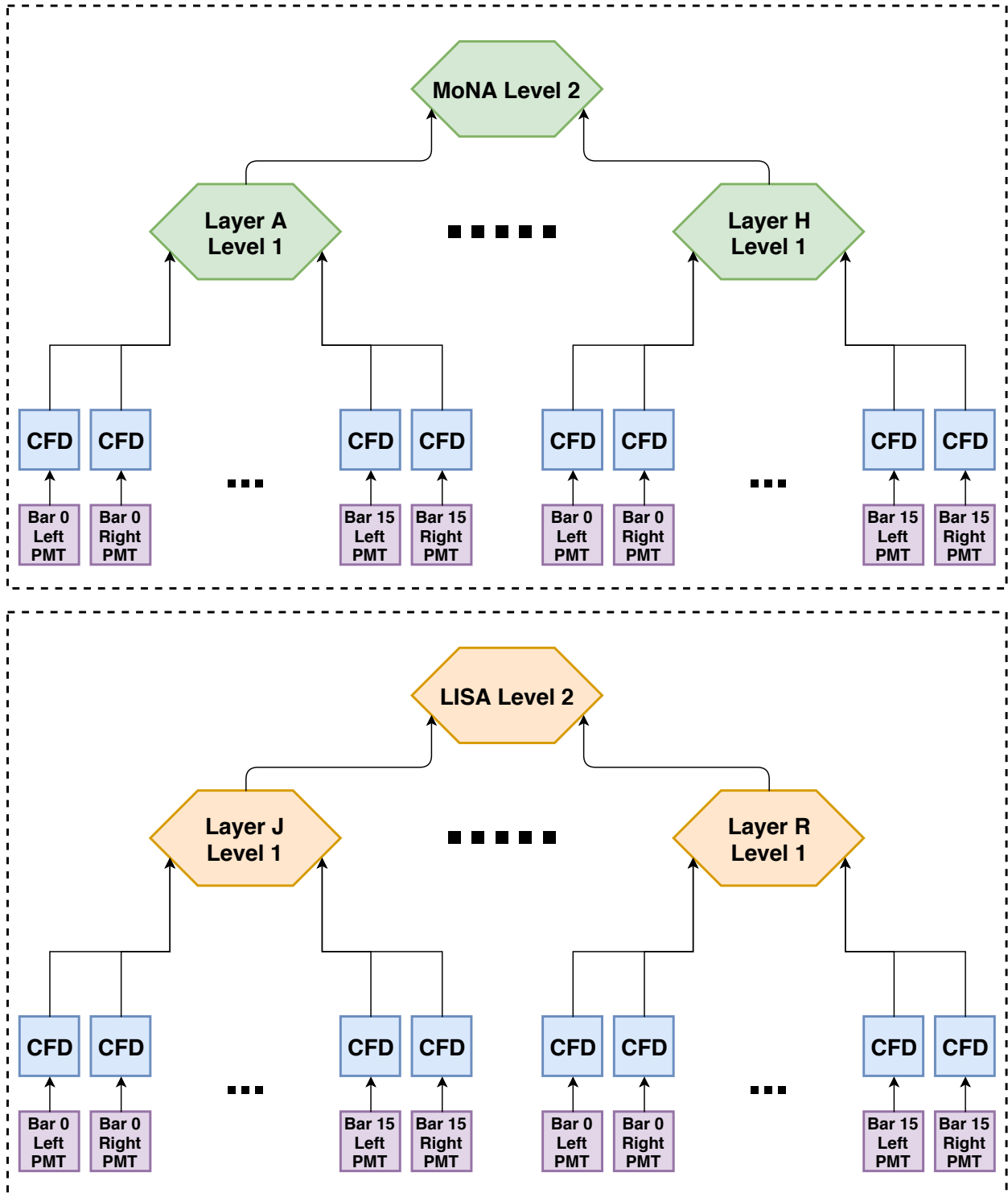


Figure 3.10: An (abbreviated) diagram of the MoNA/LISA trigger logic modified from Reference (81). Each Level 1 XLM is connected to 32 CFDs to count the number of times the left and right PMTs on the same bar fire. The nine Level 1 modules (layers J-R) for the LISA array and the eight modules (layers A-H) for the MoNA array are connected to two separate Level 2 modules. The TDCs and QDCs are omitted for clarity.

read out data. When Level 3 received a signal from the channel 0 PMT on the thin scintillator it generated an event tag and opened a coincidence gate. If Level 2 registered a valid event during this window, MoNA/LISA and Sweeper data were read out. If Level 2 did not register a valid event during the coincidence window, only Sweeper data were read out. If MoNA/LISA registered a valid event but no Level 3 trigger was generated Level 2 generated a fast clear of the MoNA/LISA TDCs and QDCs. Figures 3.9 and 3.10 are schematics of the MoNA-LISA-Sweeper electronics and MoNA-LISA electronics setups respectively.

The electronics for the Sweeper detectors were set up to read out signals from three timing scintillators, two CRDCs, the ionization chamber and the silicon detectors in the segmented target. Timing signals from the PMTs on the A1900, target and thin scintillators were routed through CFDs to TDCs. All Sweeper TDCs operated in common start mode where the Level 3 trigger began the timer and the individual CFD signals stopped the timer. Separate signals from the PMTs on the target and thin scintillators were delivered to QDCs to measure the total light collected. The pad signals from the CRDCs were digitized by Front-End-Electronics (FEE) modules which sampled the pad's signal and sent the information to an XLM for readout. Each ion chamber pad signal was processed through a shaping amplifier into an analog-to-digital converter (ADC). The signal path for the silicon detectors was described in Section 3.4.2.

3.9 Invariant Mass Spectroscopy

Invariant mass spectroscopy can provide information about systems that decay on extremely short time scales. Neutron emission from an unbound system typically occurs on the order of 10^{-21} s, so a direct measurement of the parent system is impossible. Invariant mass spectroscopy reconstructs the energy difference (E_{decay}) between the initial nucleus and the decay products. Energy and momentum are conserved in the decay process that converts an initial nucleus with $A+n$ nucleons into a daughter fragment A and n neutrons. The rest masses of the initial system, daughter fragment and neutron are M , M_A , and m_N respectively. Energy and momentum conservation is expressed as

$$E_{\text{initial}} = E_{\text{parent}} = E_{\text{final}} = E_A + \sum_i^n E_N$$

$$P_{\text{initial}}^\nu = P_{\text{final}}^\nu$$

where P_{initial}^ν is the total four-momentum of the unbound nucleus before the decay and P_{final}^ν is the sum of the four-momenta of the decay products. The Lorentz invariant quantity $P^\nu P_\nu = M^2$ is independent of reference frame. Squaring both sides of the momentum conservation equation gives

$$\begin{aligned} (P^\nu P_\nu)_{\text{initial}} &= M^2 \\ (P^\nu P_\nu)_{\text{final}} &= \left(\sum_i^{n+1} P_i^\nu \right) \left(\sum_j^{n+1} P_{j\nu} \right) \\ &= M_A^2 + \sum_i^n m_N^2 + 2 \sum_i^n \sum_{j=i+1}^{n+1} (E_i E_j - \vec{p}_i \cdot \vec{p}_j) \end{aligned}$$

where the total $n + 1$ terms correspond to the n neutrons plus one fragment M_A , with i and j in the double sum indexing over all of the daughter particles. The conservation of momentum gives an expression for the invariant mass of the initial system M .

$$M^2 = M_A^2 + \sum_i^n m_i^2 + 2 \sum_i^n \sum_{j=i+1}^{n+1} (E_i E_j - \vec{p}_i \cdot \vec{p}_j) \quad (3.1)$$

The decay energy is defined as the difference between the energy of the initial nucleus and the energies of the decay products

$$E_{\text{decay}} \equiv M - M_A - \sum_i^n m_N. \quad (3.2)$$

For the specific case of single neutron emission, there are two particles emitted: a fragment with mass M_A and a neutron m_N . Therefore Eq. 3.1 reduces to

$$M^2 = M_A^2 + m_N^2 + 2(E_A E_N - \vec{p}_A \cdot \vec{p}_N).$$

Taking the square root of this expression and substituting the result in for M in Eq. 3.2 gives

$$E_{\text{decay}} = \sqrt{M_A^2 + m_N^2 + 2(E_A E_N - \vec{p}_A \cdot \vec{p}_N)} - M_A - m_N$$

For two neutron emission, Eq. 3.1 is written

$$M^2 = M_A^2 + 2m_N^2 + 2(E_2^2 - \vec{p}_2^2)$$

where

$$E_2^2 = E_A E_{n1} + E_A E_{n2} + E_{n1} E_{n2}$$

$$\vec{p}_2^2 = \vec{p}_A \cdot \vec{p}_{n1} + \vec{p}_A \cdot \vec{p}_{n2} + \vec{p}_{n1} \cdot \vec{p}_{n2}$$

so the decay energy is

$$E_{\text{decay}} = \sqrt{M_A^2 + 2m_N^2 + 2(E_2^2 - \vec{p}_2^2)} - M_A - 2m_N \quad (3.3)$$

The key point is that the decay energy can be expressed in terms of the energies and momenta of the daughter products, and these quantities can be measured in the lab.

3.10 The Decay in Target Technique

The decay in target technique is illustrated in Figure 3.11 and described in detail in Ref. (55). It has been used to measure the half-life of two-neutron unbound ^{26}O (1). If the decay of ^{26}O does not proceed instantaneously, then the nucleus will slow down as it travels through the target material. As a result, the neutrons are emitted from a nucleus traveling at a slower speed than if the decay did happen instantaneously. The daughter fragments and neutrons are detected after the target, and in the analysis, the fragment speed at the center of the target is reconstructed. The slower neutron speed resulting its delayed emission shifts the centroid of the relative speed distribution $|\vec{v}_n| - |\vec{v}_f|$ below zero. The longer the half-life for the decay the larger the speed difference between the neutrons and the decay fragment, see Figure 3.12.

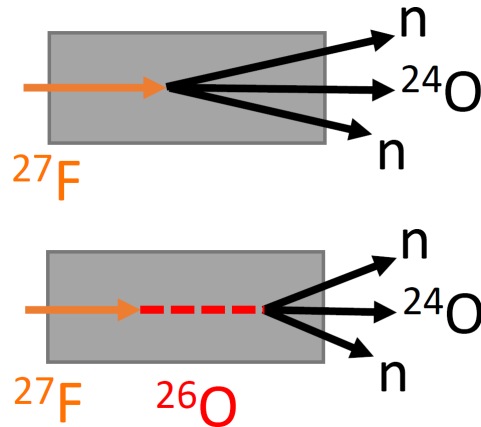


Figure 3.11: The top panel illustrates the case of an extremely short $T_{1/2} \sim 10^{-21}$ s and the bottom panel depicts a longer $T_{1/2} \sim 10^{-12}$ s. The longer ^{26}O exists the more energy it loses as it travels through the target material. This means the neutrons are emitted at a lower velocity than if ^{26}O decays instantaneously.

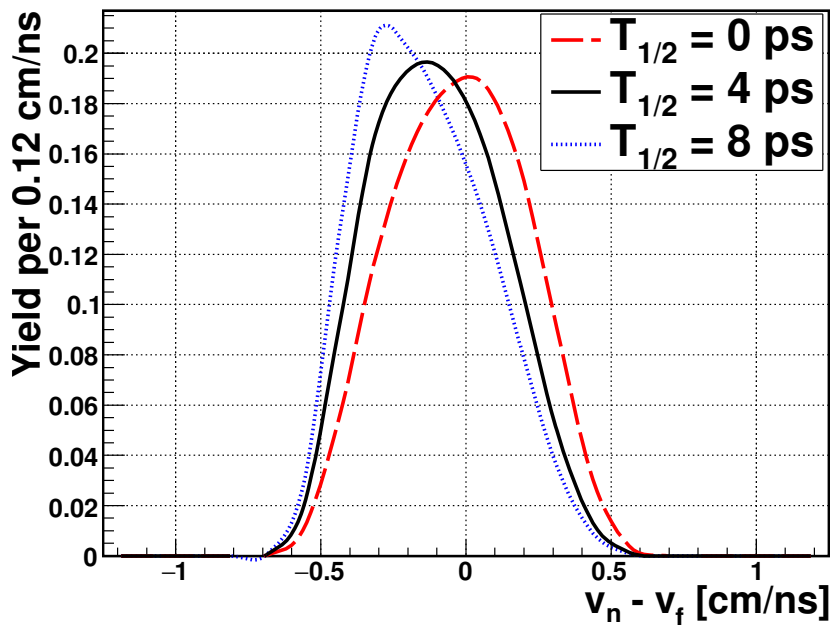


Figure 3.12: Relative speed distributions simulated with three different ^{26}O half-lives where $T_{1/2} = 0$ ps, 4 ps and 8 ps are the red dashed, black solid and blue dotted curves respectively. The relative speed is calculated as $|\vec{v}_n| - |\vec{v}_f|$ where \vec{v}_n is the neutron velocity and \vec{v}_f is the fragment velocity. The centroids of the distributions with $T_{1/2} = 4$ ps, 8 ps are shifted to the left relative to the $T_{1/2} = 0$ ps case. The reaction $^{27}\text{F}(-1p) \rightarrow ^{26}\text{O} \rightarrow ^{24}\text{O} + 2n$ was simulated.

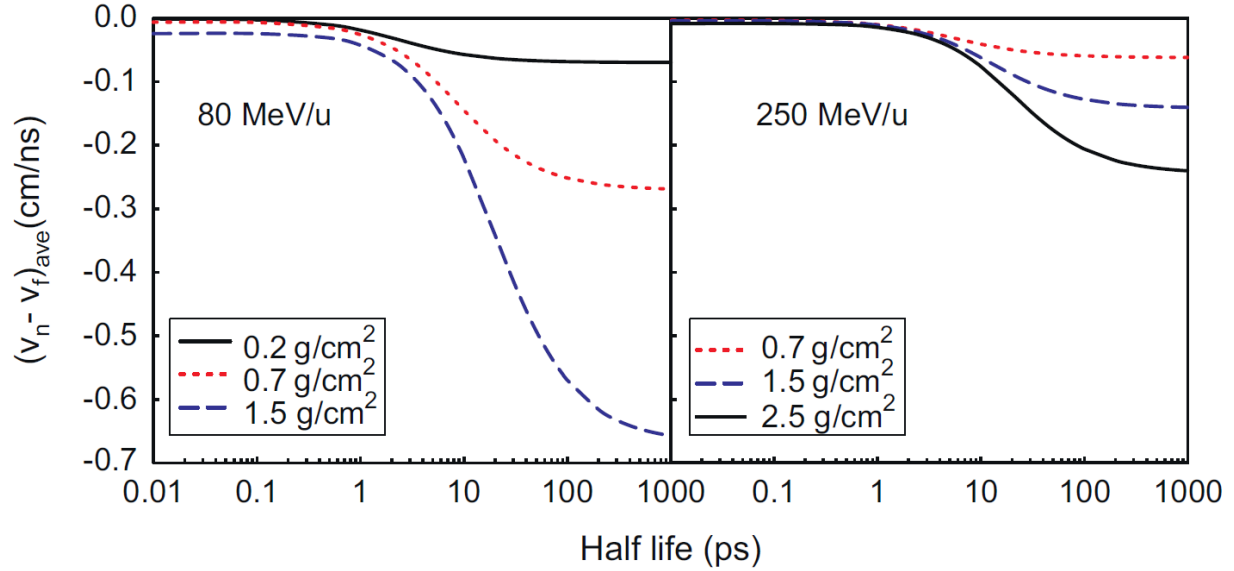


Figure 3.13: Average value of the relative speed distributions as a function of half-life using the reaction $^{17}\text{C}(-1p) \rightarrow ^{16}\text{B} \rightarrow ^{15}\text{B} + n$ at 80 MeV/u (left) and 250 MeV/u (right). Image from (55).

The sensitivity of the method was evaluated in Ref. (55) by examining the average value of the relative speed distribution as a function of half-life for the simulated one-neutron decay of ^{16}B produced from ^{17}C : $^{17}\text{C}(-1p) \rightarrow ^{16}\text{B} \rightarrow ^{15}\text{B} + n$. The simulated relative speed distributions folded in the resolution of the velocity measurements. Figure 3.13 plots the average of the relative speed distribution for two different beam energies and four different target thicknesses. Larger neutron-fragment speed differences correspond to a higher sensitivity. Based on these simulations the decay in target method is sensitive to $T_{1/2} > 1$ ps. Thicker targets are more sensitive because the speed difference depends on the energy lost in the target by the decaying neutron-unbound system. This is also why the method is more effective at lower beam energies. Ultimately, the choice of target thickness for a given beam energy is limited by the requirement that the fragment exit the target with enough energy to allow for clean identification of the fragment and a good energy measurement. Although a higher beam energy will accommodate a thicker target, a beam energy ~ 80 MeV/u and the appropriately selected target thickness was predicted to yield the best sensitivity in the $T_{1/2} \approx 4$ ps region for the ^{16}B decay (see Figure 3.14).

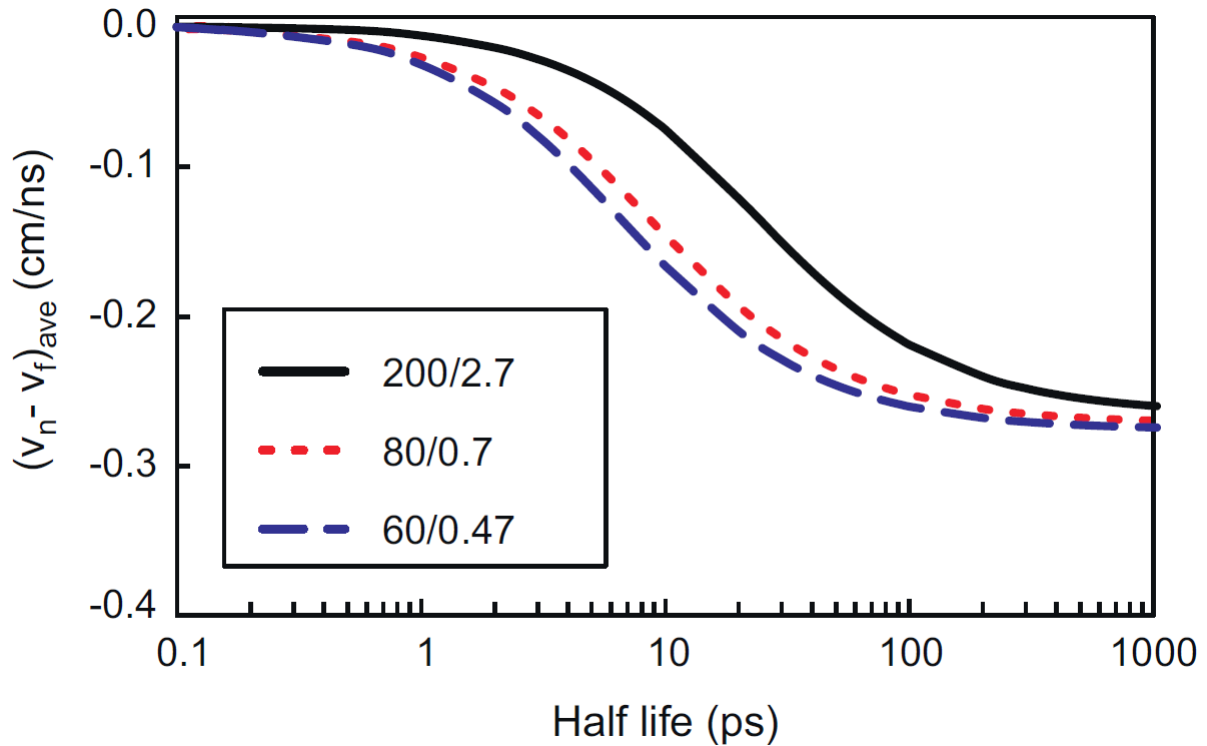


Figure 3.14: Average value of the relative speed distribution as a function of half-life for $^{17}\text{C}(-1p) \rightarrow ^{16}\text{B} \rightarrow ^{15}\text{B} + n$ and three different combinations of beam energy and target thicknesses. The first number in the legend corresponds to the beam energy in units of MeV/u and the second number is the target thickness in g/cm^2 . The beam energy/target thickness combinations were selected to give approximately the same asymptotic value for very long half-lives. Image from Ref. (55).

CHAPTER 4

DATA ANALYSIS

This chapter describes the calibration methods for producing meaningful data from the raw detector outputs of MoNA, LISA, and the Sweeper detectors. After calibrations, the event selection procedure is discussed followed by modeling and simulation.

4.1 Calibrations and Corrections

Information from each detector channel is digitized and written to disk. In order to extract meaningful physics, this information must be converted from raw detector values to physical quantities. For example, TDC channel numbers need to be converted to times. Each type of detector has a specific calibration procedure.

4.1.1 Segmented Target

The segmented target was described in Section 3.4 and was used in this experiment to increase reaction yield without sacrificing decay energy resolution, see the discussion in Section 2.4. Energy loss information from the silicon detectors was used to determine in which beryllium target the reaction to produce ^{26}O and the subsequent $2n$ decay occurred. This section describes how the energy loss signals were calibrated and how the reaction target was identified. Note that a survival time of 10 ps in the lab frame corresponds to a distance of 1 mm for a decaying particle traveling at 10 cm/ns. Therefore, any ^{26}O produced in a beryllium target will decay inside or within 1 mm of the Be segment. For reference, the beryllium targets are ~ 4 mm thick and the distance between elements of the segmented target is 8.4 mm. The probability for producing ^{26}O in a silicon detector is negligible.

4.1.1.1 Energy loss calibration

The Coulomb force between electrons and heavy charged particles is the primary interaction by which the kinetic energy of the heavy ions is transferred to the material through which they are traveling (28). The maximum energy transferred in a single interaction is $4Em_0/m$ where E is the kinetic energy of a charged particle with mass m and m_0 is the electron mass. Since the electron-to-nucleon mass ratio $m_0/m_{np} \approx 1/2000$, the maximum energy transfer for a single interaction is about 1/500 of the KE/A of the heavy particle. Through many of these interactions the particle continuously loses energy in the absorbing material. The energy loss per unit path length, or stopping power, dE/dx is proportional to the square of the charge of the particle divided by its velocity squared

$$-\frac{dE}{dx} \propto \frac{Z^2}{\beta^2} \quad (4.1)$$

where β is the speed of the particle divided by c and Z is the atomic number of the particle. The particles are fully ionized in the cyclotrons, and they maintain a high enough velocity that their charge state does not change during the course of the experiment. The full form of the energy loss (Bethe) equation for a charged particle in an absorber is given in Equation (2-2) of Ref. (28) and Equation (1) in Ref. (84).

In the case of silicon, its semiconductor properties allow a measurement of the energy transferred to the electrons to be made. The brief explanation of this process given here is summarized from Chapter 11 in Ref. (28). The periodic lattice into which silicon atoms organize establishes allowed energy bands for the electrons in the solid; see Figure 4.1. These bands are separated by gaps or ranges of forbidden energies. The lower energy band is called the valence band and corresponds to electrons that are part of covalent bonds between adjacent atoms in the crystalline structure. A higher energy “conduction” band corresponds to electrons that are free to migrate through the crystal. The Coulomb interactions described in the previous paragraph can excite electrons from the valence band into the conduction band where they can move freely through the crystal. These excited electrons leave behind a vacancy in the valence band which, together with

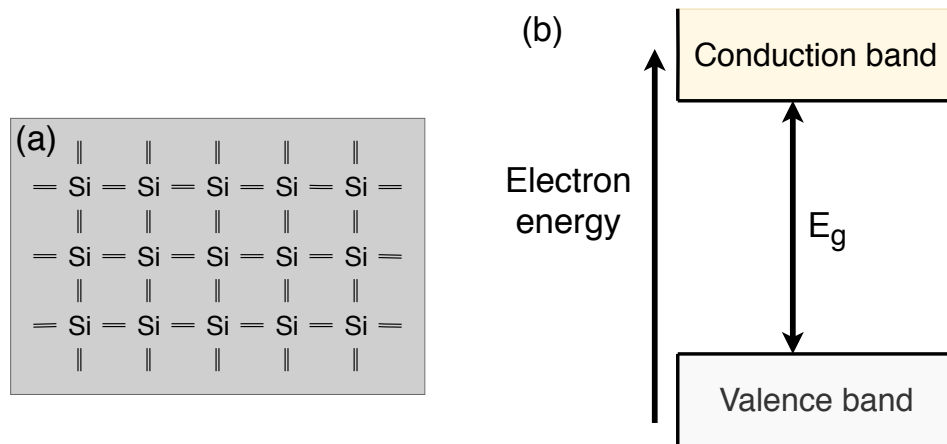


Figure 4.1: The upper panel (a) illustrates the silicon lattice structure with covalent electron bonds depicted by the black lines. The bottom panel (b) sketches the electron energy band structure. In semiconductors, $E_g \approx 1$ eV. Both illustrations are adapted from Ref. (28).

the freed electron, are referred to as electron-hole pairs. Applying an electric field to the crystal causes the electrons and holes to migrate in opposite directions to the edges of the material where they can be collected on electrical contacts to produce a signal that is proportional to the energy transferred from the passing charged particle.

The silicon detector dE signals can be used to identify the reaction target without an absolute calibration, however, one was performed in order to check for consistency between measurement and simulation. From the data recorded during the experiment, a total of eight different beam fragments were identified with energy losses in the same range (5 MeV - 30 MeV) as the energy losses of the oxygen reaction products from ^{27}F . They are listed in Table 4.1 along with their kinetic energies determined by the settings of the A1900 fragment separator (73) used to filter and deliver the beam. The eight beam fragments were used to calibrate the energy loss measured by each of the four silicon detectors and quantify the uncertainty associated with the calibration according to the following four step procedure.

1. For each fragment, events were selected where the fragment charge did not change in the segmented target. This was achieved using two analysis gates: (1) on the first silicon energy loss as a function of A1900-to-target-scintillator time-of-flight (ToF) to identify each incoming fragment and (2) a gate on the energy lost in the ion chamber as a function of the ToF

Fragment	KE [MeV/u]	Energy loss [MeV]			
		Si 0	Si 1	Si 2	Si 3
²⁷ F	105.3	14.838	15.919	18.568	22.649
²⁸ Ne	120.2	16.667	17.732	20.393	24.315
²⁹ Ne	112.8	17.470	18.747	21.939	26.785
³⁰ Na	124.9	19.626	21.006	24.427	29.619
²¹ O	136.8	9.748	10.000	10.946	12.122
²² O	125.3	10.345	10.719	11.863	13.316
²³ O	115.2	10.978	11.485	12.889	14.707
²⁴ O	106.3	11.650	12.298	14.004	16.358

Table 4.1: Energy loss of eight different fragments in each silicon detector calculated using the ATIMA energy loss calculator included within the LISE++ software package (85). Calculation of these values accounts for the energy loss in the beryllium segments since the targets were always in the beam line. Variations in the material thicknesses correspond to variations in the calculated dE less than ± 0.008 MeV, so $\lesssim 0.05\%$, which is smaller than the resolution of the detectors.

between the target and thin scintillators to identify Z after the target.

2. Using a χ^2 minimization routine, Gaussian fits were performed on the uncalibrated ADC spectra to determine the centroid locations for the energy loss (dE) distributions of each detector.
3. Calculations using the ATIMA energy loss calculator embedded in LISE++ (85) determined the expected energy loss for each fragment. The thicknesses of the targets and detectors were varied by $\pm 4 \mu\text{m}$ (targets) and $\pm 1 \mu\text{m}$ (detectors) to quantify an uncertainty in the calculations introduced by the uncertainty in the measured thicknesses of the materials. The thickness variations correspond to dE variations of $\pm 0.05\%$.
4. Calibration curves (see Figure 4.2) were extracted to convert raw ADC channels (dE_{raw}) to units of MeV. The calibrations had the form $dE_{\text{cal}} = p_0 + p_1(dE_{\text{raw}})$ and were extracted from fits to plots of the calculated energy loss from step (3) as a function of the centroids extracted in step (2). The uncertainty from fitting the calibration curves is $< 2.0\%$ in the range of energy losses between 10 MeV and 35 MeV.

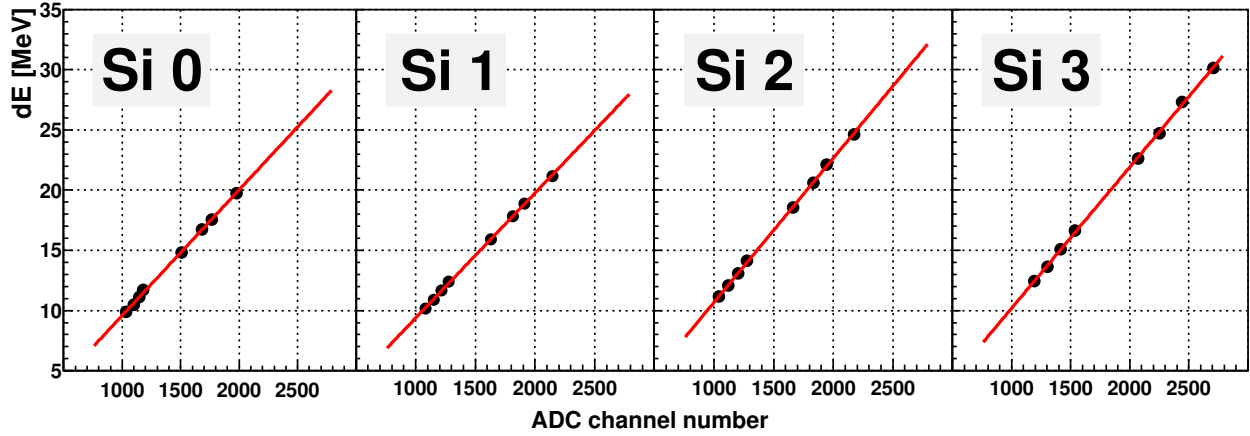


Figure 4.2: Black points plot calculated energy loss (y-axis) as a function of fitted centroid of the uncalibrated dE spectrum (x-axis) for eight different fragments. The four panels show the results for the four silicon detectors. The blue lines show the extracted linear fits. The x error bars for the fit errors and the y error bars for the measurement/calculation uncertainties are smaller than the points. The parameters from the fit are listed in Table 4.2.

Silicon Detector	Slope (p_0) [MeV / ADC ch]	Offset (p_1) [MeV]
0	0.0104(1)	-0.86(2)
1	0.0104(1)	-0.99(2)
2	0.0120(1)	-1.30(2)
3	0.0117(1)	-1.52(2)

Table 4.2: The second and third columns list parameter values extracted from the fits $dE_{\text{cal}} = p_0 + p_1 dE_{\text{raw}}$, see Figure 4.2. The fit errors are $< 2.0\%$ in the range from 10 MeV to 35 MeV.

4.1.1.2 Reaction Target Identification

The segmented target system described in Section 3.4 was used in this experiment to increase the reaction yield by placing three separate beryllium targets in the beam line, thus increasing the number density of target atoms. Energy loss measurements from the silicon detectors were used to identify the beryllium target in which the ^{26}O was produced event-by-event. Events where the incoming fragment was ^{27}F are identified via energy loss measured in the first silicon detector and time-of-flight (ToF) from the A1900 to the target scintillator. Events where a reaction in one of the beryllium targets produced an oxygen isotope are identified from the energy loss measured in the ionization chamber after the Sweeper magnet and the ToF from the target scintillator to the

thin scintillator. This set of analysis gates selects a subset of events where a one-proton knockout reaction occurred. To determine if a particular beryllium target induced the proton knockout, the energy loss measured in the upstream silicon detector must be compared to the energy loss measured in the downstream silicon detector. Consider two cases where (1) a nuclear interaction somewhere in the beryllium target knocks a proton out of ^{27}F and (2) no proton is knocked out: in both cases the energy loss registered by the upstream detector is the same while the downstream detector will record a smaller energy loss in case (1) than it will in case (2) because Z changes from nine to eight and energy loss is proportional to Z^2 .

Figure 4.3 illustrates how the reaction target is identified using the energy loss measurements from the silicon detectors. All events plotted in Figure 4.3 are selected so that the incoming fragment was ^{27}F and the outgoing fragment (after the segmented target) was an oxygen isotope. The top row plots the dE spectra for each silicon detector. The bottom row plots the energy loss measured in one detector versus the energy loss measured in the previous detector; spectra in the top row are 1D projections onto the x and y axes of the bottom row plots. The 1D spectra titled “Si 0 dE ” is the x -axis of the left-most plot in the bottom row. Si 1 dE is the y -axis on the left-most and the x -axis on the middle plot. Si 2 dE is the y -axis on the middle plot and the x -axis on the right-most plot. Si 3 dE is the y -axis on the right-most plot.

In the left-most panels of the top and bottom rows in Figure 4.3, the first silicon detector (Si 0) registered roughly the same energy loss for all events. The spread is introduced by the energy spread of the beam and the resolution of the detector itself. The dE measurement from Si 1 separates events into two distinguishable groups. Events in the upper group on the 2D spectrum (red-highlighted peak in the 1D spectrum) lose more energy in Si 1 because no proton knockout occurred between the two detectors. There are three clusters in the middle panel corresponding to unreacted ^{27}F (top), oxygen reaction products from Be 1 (bottom left) and oxygen reaction products from Be 2 (bottom right); the two lower clusters both contribute to the blue-highlighted peak on the left of the “Si 2 dE ” 1D spectrum. The two groups in the right-bottom panel correspond to oxygen reaction products from Be 1 or Be 2 (left) and oxygen reaction products from Be 3

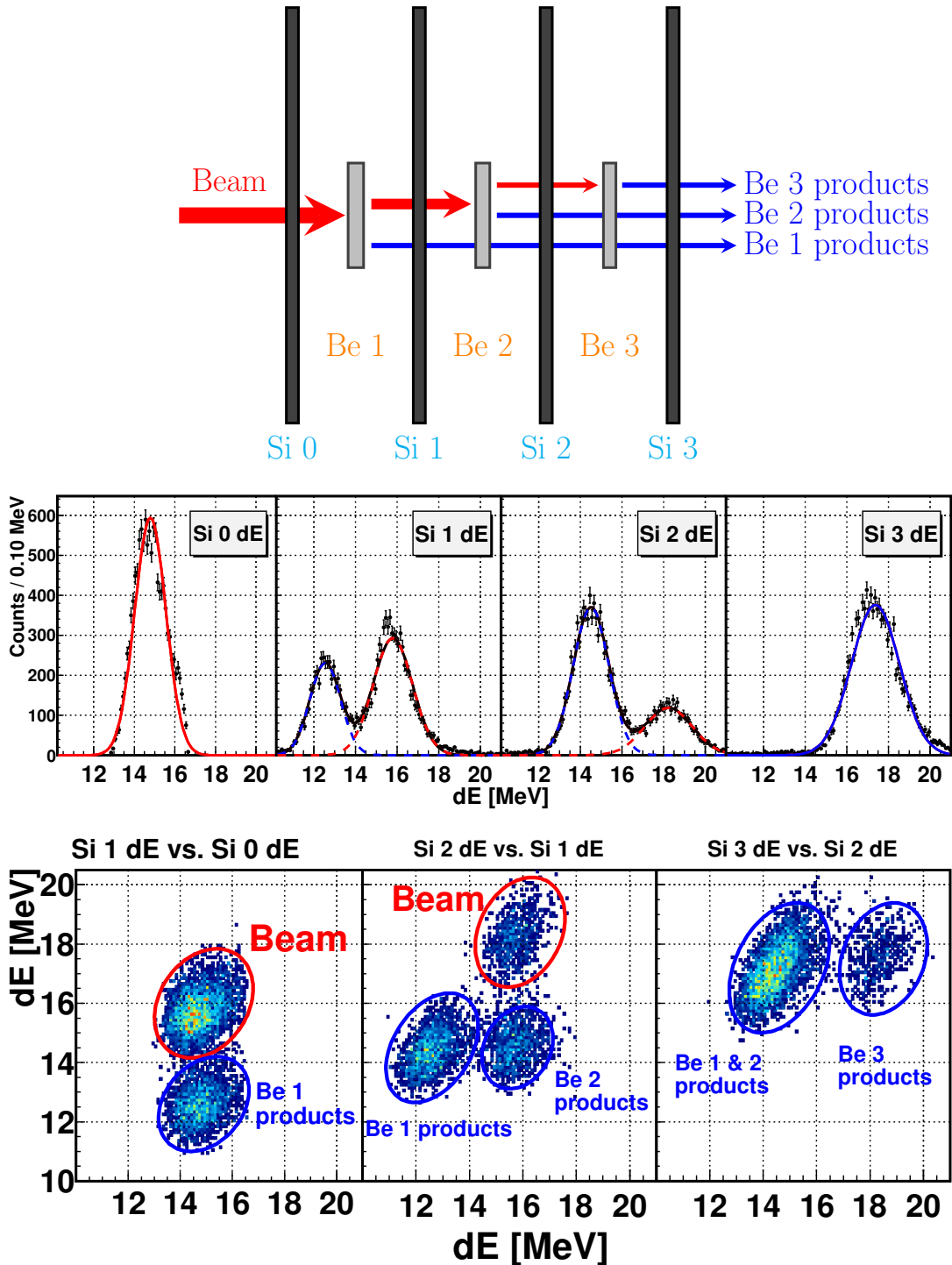


Figure 4.3: Example target identification plots for $^{27}\text{F}(-1p) \rightarrow {}^A\text{O}$ meaning that all events plotted here enter the segmented target as ^{27}F and leave as an oxygen isotope. The top row of plots show the measured energy loss in each silicon detector. The left panel in the bottom row of plots shows the measured energy loss in the second silicon detector vs. the measured energy loss in the first silicon. The middle panel plots the third silicon energy loss vs. the second and the right panel shows the fourth silicon energy loss vs. the third.

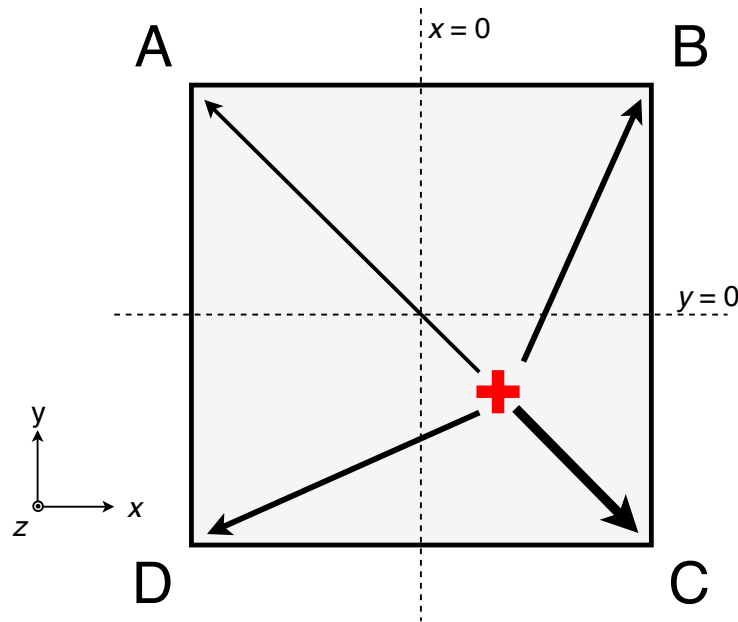


Figure 4.4: Schematic of a silicon detector and the coordinate convention used for the position calibration. The size of the arrows illustrates the signal size at each of the four corners for an ion interacting at the location of the red cross.

(right).

4.1.1.3 Position calibration

The (x, y) coordinates where the charged particle passed through a silicon detector can be reconstructed based on the relative pulse heights of the corner signals recorded by the analog-to-digital converter (ADC). This information was used to set the beam (x, y) profile for the simulation; see Section 4.4.1. The method for calculating x and y event-by-event relies on resistive charge division due to the surface resistance of the boron-implanted front layer where the aluminum evaporated contacts are made at each corner; see Section 3.4.1. Roughly equal-sized signals will be generated at the four corner contacts when a charged particle passes through the exact center of detector. However, a charged particle passing through the detector close to one of the corners will result in a larger signal generated at the contact on that corner.

The x and y coordinates for the interaction point of a charged particle in one of the silicon detectors may be calculated in the following way. With a right handed coordinate system (i.e.

looking into the beam), label the charge collected at the upper left, upper right, lower right and lower left corner contacts A , B , C , and D respectively, see Figure 4.4. Define the following relationships for the signal amplitudes generated at each contact:

$$\Sigma \equiv A + B + C + D$$

$$L \equiv A + D$$

$$R \equiv B + C$$

$$U \equiv A + B$$

$$D \equiv C + D$$

The x and y coordinates are then given by

$$x = S \frac{R - L}{\Sigma}$$

$$y = S \frac{U - D}{\Sigma}$$

where S is the side length of the detector's active area, 31 mm in this case.

4.1.2 Charged particle calibrations and corrections

Upstream from the target are two timing scintillators used to identify the beam. Following the Sweeper magnet are several charged-particle detectors: two CRDCs, an ionization chamber and a thin scintillator.

4.1.2.1 A1900 and Target scintillators

The A1900 scintillator was positioned at the A1900 focal plane and the target scintillator was placed 1.03 m upstream from the segmented target. Both timing scintillators were outfitted with a single PMT that measured time and light output. The A1900 scintillator was located 10.9 m

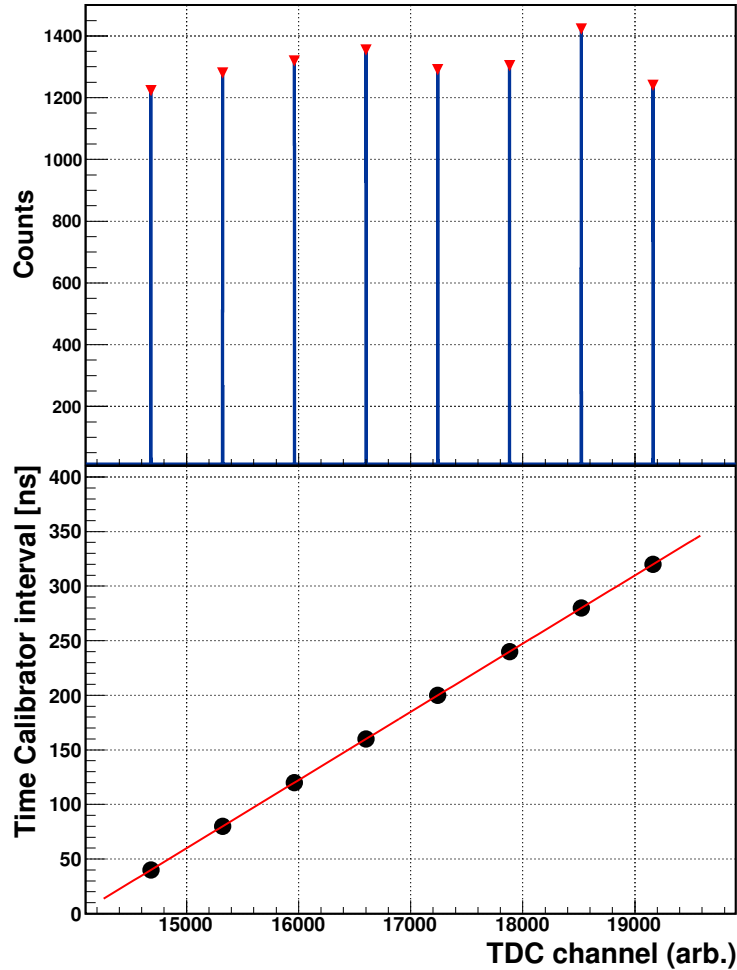


Figure 4.5: The top panel shows an example TDC spectrum measured using an Ortec time calibrator set to deliver start and stop signals separated by integer multiples of 40 ns. The bottom panel plots the start-stop time intervals versus the peak locations from the top panel. The red line is a linear fit used to extract the conversion factor from TDC channel number to time in nanoseconds. The slope of the line is 0.0625 ns/ch and the fit error is negligible.

upstream from the segmented target and only a timing signal from its PMT was recorded. Timing signals from both PMTs were processed by separate time-to-digital converters (TDCs) in the same Mesytec TDC module. These TDCs have manufacturer specified slopes of 0.0625 ns/ch and this was confirmed using an Ortec time calibrator. TDCs measure the time between start and stop signals and the time calibrator provides start and stop signals at precise intervals. The top panel of Figure 4.5 shows an example TDC spectrum taken with the time calibrator set to deliver start and stop signals separated by 40 ns, 80 ns ... 320 ns. This means peaks in the spectrum are separated by

40 ns. The bottom panel in Figure 4.5 plots the start-stop time intervals set by the time calibrator versus the peak position in the TDC spectrum. The slope of a linear fit to these points gives the conversion factor ($0.0625 \pm 6 \times 10^{-16}$ ns/ch) from TDC channel number to time in nanoseconds.

In addition to the A1900 and target scintillator timing signals, four timing signals from the thin scintillator (discussed in Section 4.1.2.4) were processed by the Mesytec TDC module. The slopes for each of these six TDCs were confirmed to be 0.0625 ns/ch, and this conversion factor was used to convert all six timing spectra to units of nanoseconds. After this conversion the difference between the A1900 and target scintillator timing signals corresponded to the time for beam fragments to traverse the 9.87 m distance between the two scintillators.

The light output signal from the target scintillator was left uncalibrated since an absolute measure of the light produced in this detector was not necessary for the analysis. However, the time difference (e.g. between A1900 and target scintillators) was plotted against the raw light output signal for the target scintillator to check for deviations in the measured flight time due, for example, to low light output in the target scintillator. No deviations were observed.

4.1.2.2 CRDCs

The CRDCs measure the (x, y) position of charged particles passing through their active volumes; these detectors were described in Section 3.6.1. The first CRDC was placed 1.86 m from the segmented target (measured along the central arc). The second CRDC was positioned 1.54 m downstream from the first.

During the experiment some of the integrated circuit (IC) chips that process signals from the cathode pads on CRDC 1 overheated. It was determined that replacing these chips and repairing the electronics board within the time allotted for the experiment was not possible. Furthermore, even if repairs were completed the system would likely overheat again and destroy the new chips. This malfunction corrupted the x position information in specific sections of CRDC 1. This information was lost because there was no systematic pattern to the data corruption that would have allowed it to be corrected. During the attempted repair of CRDC 1 the corresponding circuit board for CRDC

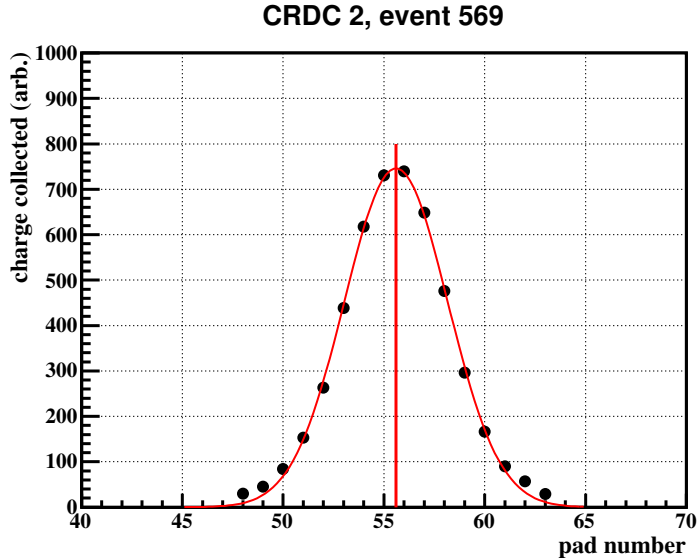


Figure 4.6: Charge collected (black points) as a function of CRDC 2 pad number for a single event. The red curve is a Gaussian fit and the red vertical line is the centroid extracted from the fit.

2 was replaced because it was beginning to show signs of a similar failure. These changes to the electronics necessitated two separate sets of calibrations. The slopes and offsets for the position calibration did not change because the physical location of the pads and the fill gas pressure and drift voltages were the same. However, the pedestals and gain matching scale factors were affected by the electronics changes. The following paragraphs describe the CRDC calibration procedures and Table 4.3 summarizes the calibration parameters.

The CRDC x position for one event is determined by measuring the charge collected on 116 2.54 mm wide pads. The distribution of charge across the pads is approximately Gaussian (see Figure 4.6). In order to extract a reliable position, the pads must be pedestal-subtracted, bad pads must be removed and the pads must be gain matched. The physical size of the detector and its measured position in space determine the conversion from fitted pad number to x relative to the beam axis.

A small leakage current produces signals that vary from pad to pad. This “pedestal” signal must be subtracted to accurately determine the total charge collected. Data were recorded when the electronics were on and the beam was off. The charge distribution for each pad are plotted in the top row of Figure 4.7. A Gaussian fit to the charge distribution of each pad provides a centroid

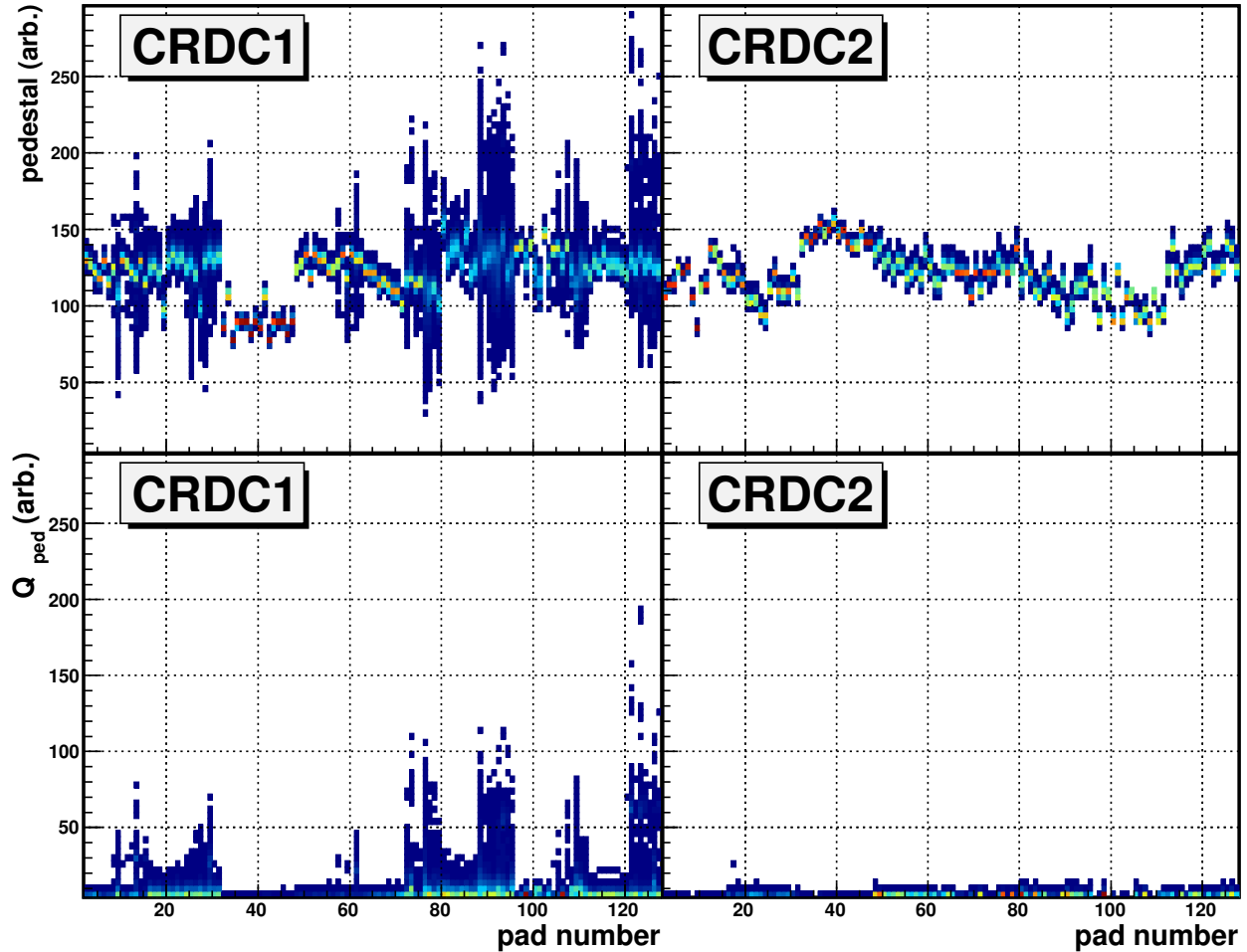


Figure 4.7: CRDC pedestal subtraction. The raw pad signals for CRDC 1 (left) and CRDC 2 (right) are shown in the top row. The centroid of a Gaussian fit to the charge distribution of each pad is subtracted to shift the center of each distribution to zero. The result of the pedestal subtraction is shown in the bottom row: CRDC 1 (left) and CRDC 2 (right).

which is used as an offset to center each pad distribution around zero. The result of this pedestal subtraction is shown in the bottom row of Figure 4.7.

Before calculating positions, the quality of each pad is examined. Pads that show poor charge collection (due to noise, for example) are removed from the analysis, see Figure 4.8.

After subtracting the pedestals, CRDC pads must be gain matched to account for differences in charge collection and amplification between pads. The Sweeper current is continuously ramped up and down in order to sweep the beam across the charged particle acceptance. Since the beam particles have roughly the same energy the energy deposited in a track that passes by pad A should

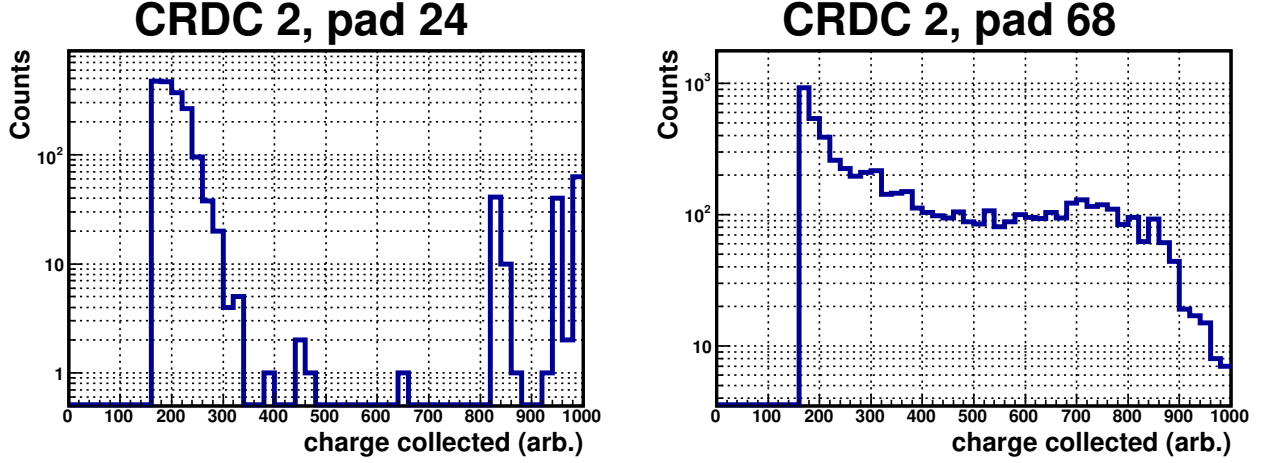


Figure 4.8: Example spectra showing the total charge read out by two pads in CRDC 2. Pad 68 (right) is an example of a correctly functioning pad; pad 24 (left) is deficient.

be the same as the energy deposited in a track that passes pad B. This means that a difference between the signals recorded by pad A and pad B is due to some artifact of the detector or to the electronics that process the pad signals. Gain matching the pads removes these types of systematic differences between pads.

Unreacted ^{27}F beam was used to gain match the CRDC pads because this beam was centered in the A1900 so it had the most nearly uniform kinetic energy distribution. For every event, the pad that registered the most charge out of all 116 pads on the detector was identified. A charge distribution for each pad was built out of events where that pad registered the most charge. These distributions were then scaled to a reference:

$$m_i = \frac{\mu_{\text{ref}}}{\mu_i}$$

where μ_i is the fitted centroid of the charge distribution on pad i and m_i is the scale factor for pad i .

The total charge induced on a pad is estimated by a Riemann sum over four samples taken during the course of the event. The total charge is calculated as

$$Q_i = \frac{1}{n} \sum_{i=0}^n q_i - q_{\text{pedestal}}$$

where n can vary from one to four. The gain matched pad charge is then calculated as

$$Q^{(\text{cal})}_i = m_i Q_i$$

The calibrated charge $Q_i^{(\text{cal})}$ for each pad is plotted for a single event in Figure 4.6. A Gaussian fit to the distribution of charge across the pads determines the x position in terms of pad number.

The y position is determined by the time it takes electrons to drift from the interaction track to the anode wire. The final (x, y) position in the lab frame requires a conversion from pad number/time to distance. This is done using a tungsten mask with a known hole pattern. The mask is placed in front of the detector and stops beam particles before they pass through the CRDC. A position spectrum taken with the mask in place provides a linear transformation from (pad number, drift time) to (x, y) .

The pitch of the pads is 2.54 mm and this determines the slope of a first order polynomial function that converts pad number to lab frame x . An offset to orient the detector relative to the beam axis is determined from the position spectrum taken with the mask in place. The scale factor for converting drift time to y position is determined from the known hole spacing on the mask. The y offset is determined by the measured position of unreacted ^{27}F - this aligns the xz -plane with the beam trajectory. Ultimately, y position measurements did not contribute to the fragment reconstruction because of the faulty CRDC1, therefore, a high-accuracy calibration for absolute y position was not crucial.

The CRDCs are placed in opposite orientations relative to the $+x$ direction. The pad number for CRDC1 increases in the $+x$ direction; the pad number for CRDC2 increases in the $-x$ direction. This is why the x slopes differ by a sign.

The y position measured by a CRDC can drift over time due to fluctuations in the gas pressure and the drift field voltage. These effects are corrected by scaling the raw drift time to a reference run and performing a run-by-run correction. The correction factor is computed as

$$m = \frac{\mu_{\text{TAC}}^{\text{ref}}}{\mu_i}$$

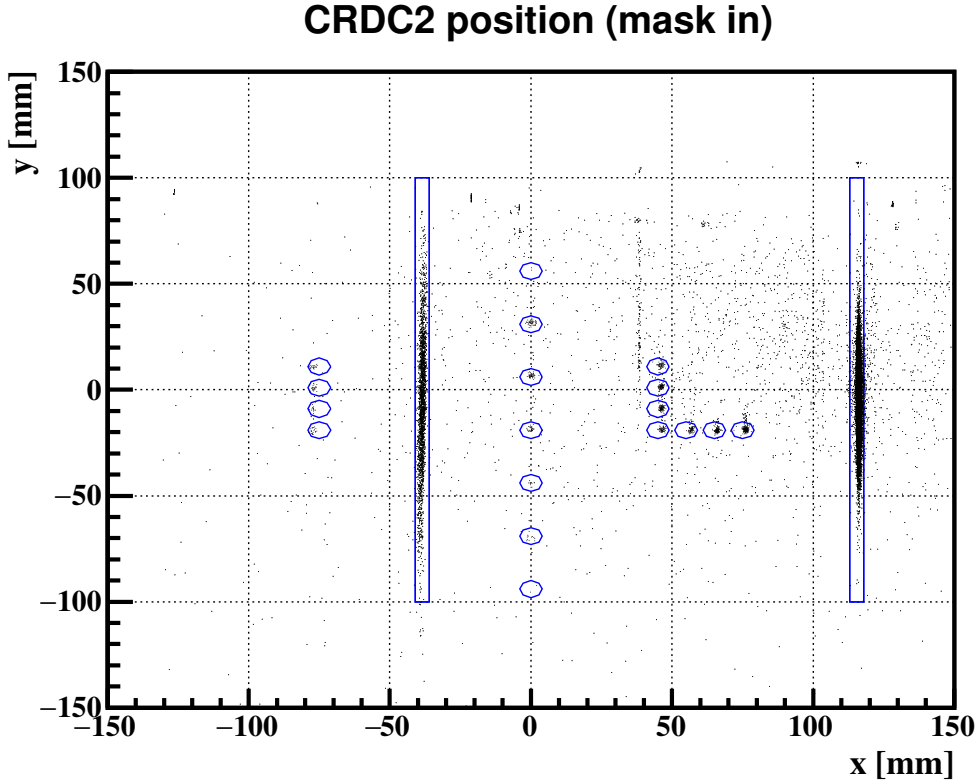


Figure 4.9: Calibrated position spectrum with the mask pattern overlaid. The same y offset extracted from the unreacted beam position is applied to the mask pattern.

where $\mu_{\text{TAC}}^{\text{ref}}$ and μ_i are the centroids of the timing signal distributions in the reference run and the i^{th} run respectively. The results of this correction are shown in Figure 4.10. A similar correction was applied to CRDC2.

4.1.2.3 Ionization Chamber

The ionization chamber was positioned immediately behind the second CRDC. It is segmented into 16 pads along the z direction. During an event each pad collects a charge proportional to the energy lost by an ion passing through the detector. The average of the pad signals is proportional to the total energy deposited and can be used to identify particle Z event-by-event. The pad signals must be inspected to identify malfunctioning pads and remove them from the analysis. Good pads are gain matched to normalize the pad signals. Finally, any drift in the pad responses over time are removed by normalizing to a reference run. Examination of the pad responses showed

Runs 1038 - 1121

	Bad pads	Avg. pedestal		Avg. gain scale factor
CRDC1	0 - 56, 99 - 115	121		1.01
CRDC2	24	120.5		1.01
	x slope [mm/pad]	x offset [mm]	y slope [mm/ns]	y offset [mm]
CRDC1	2.54	-177.9	-0.075	106.0
CRDC2	-2.54	187.0	-0.074	105.7

Runs 1125 - 1179

	Bad pads	Avg. pedestal		Avg. gain scale factor
CRDC1	0-53,54,56,63,64,95 - 115	110.4		1.02
CRDC2	23,24,30,31,32	116.5		1.05
	x slope [mm/pad]	x offset [mm]	y slope [mm/ns]	y offset [mm]
CRDC1	2.54	-177.9	-0.075	106.0
CRDC2	-2.54	186.9	-0.074	110.3

Table 4.3: CRDC calibration parameters applied to runs before (1038 - 1121) and after (1125 - 1179) the attempted electronics repairs (see text). Bad pads are deficient cathode pads that are removed from the analysis. The pedestal subtraction is summarized by the average of all pedestal values. Similarly, the gain scaling factor is averaged over all good pads. Note that these two values are not actual calibration parameters. The xy slopes and offsets were extracted from spectra taken with the tungsten mask in place.

that channels 0, 4, 7 and 15 collected ten times less charge or none at all; see the left panel in Figure 4.11. These pads were removed from the analysis.

The gain matching procedure ensures that the signal from each pad is the same for the same amount of energy deposited. This requires selection of a subset of events where the kinetic energy and type of particle passing through the detector are the same. Unreacted ^{27}F events were used to gain match the ionization chamber pads.

The gain matching is implemented by finding a scale factor m_i for each pad such that

$$m_i = \frac{c_{\text{ref}}}{c_i}$$

where c_{ref} and c_i are the centroids of a reference (pad 12) pad's and the i^{th} pad's charge-collected distribution respectively. The gain matched charge for pad i is then

$$q_i^{(\text{cal})} = m_i q_i^{(\text{raw})}$$

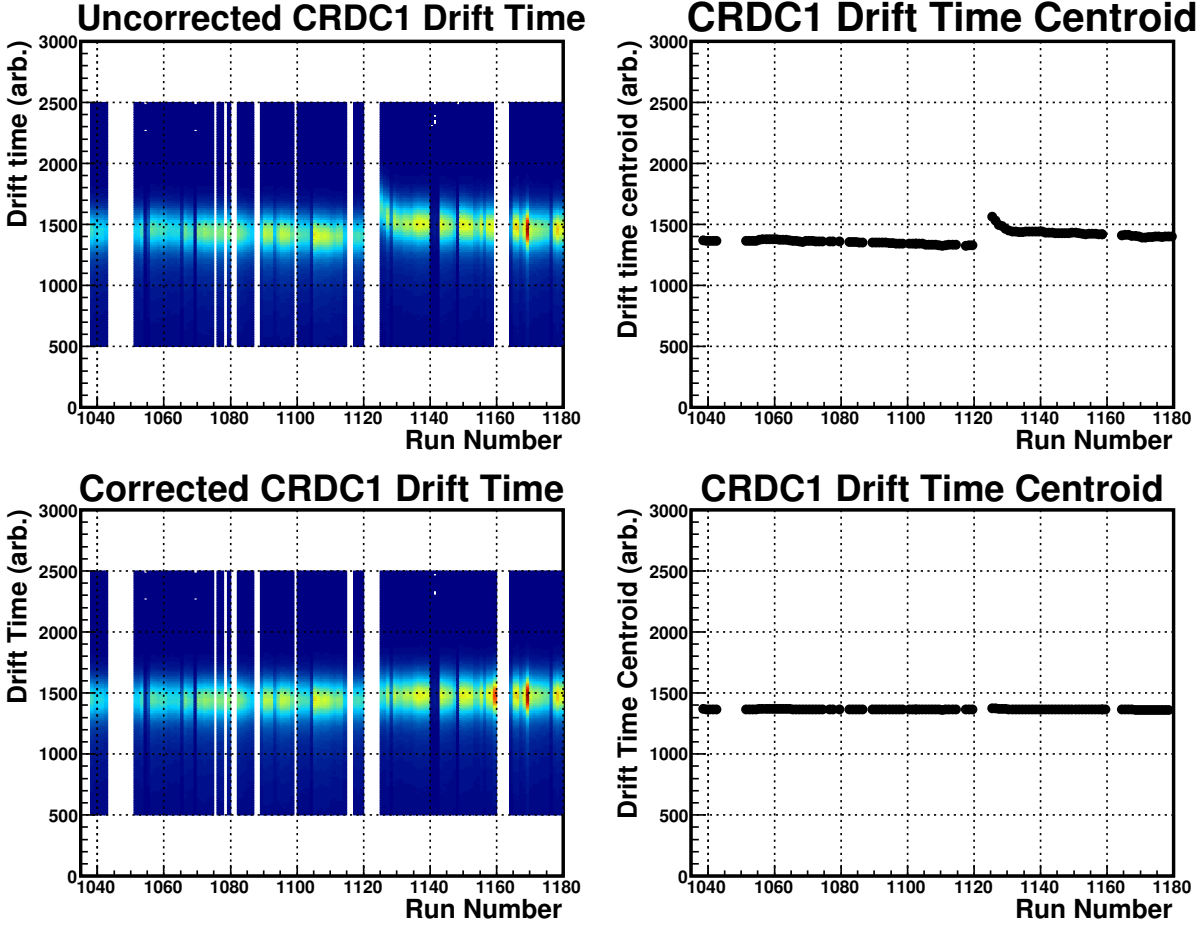


Figure 4.10: Uncorrected (top row) and corrected (bottom row) drift times for CRDC1. The discontinuity at run 1125 is due to the two separate calibration parameters described in the beginning of Section 4.1.2.2.

The results of the gain matching procedure for the ion chamber pads are shown in Figure 4.11. The average of the 12 signals from the good pads is taken event-by-event to measure the energy deposited by the charged fragments in the ion chamber.

A time-dependent drift in the charge collected by each ion chamber pad was observed over the course of the experiment. This was corrected using a run-dependent offset to align the collected-charge distribution of each pad from run to run. With this shift the final calibrated pad signal is given by

$$q_i^{(\text{cal})} = m_i q_i^{(\text{raw})} + b_i(r)$$

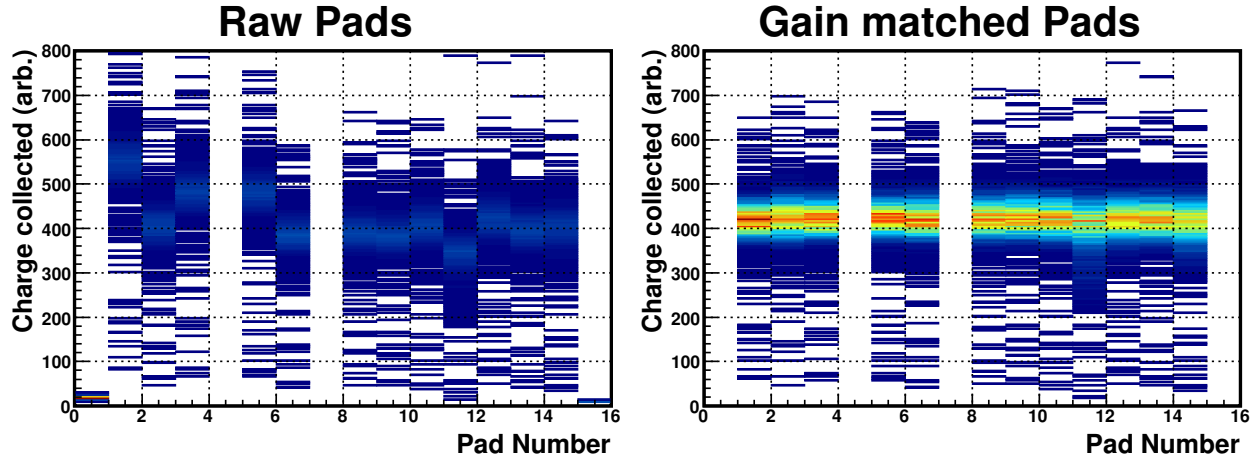


Figure 4.11: The charge collected by the ionization chamber pads for unreacted ^{27}F events before (left) and after (right) gain matching.

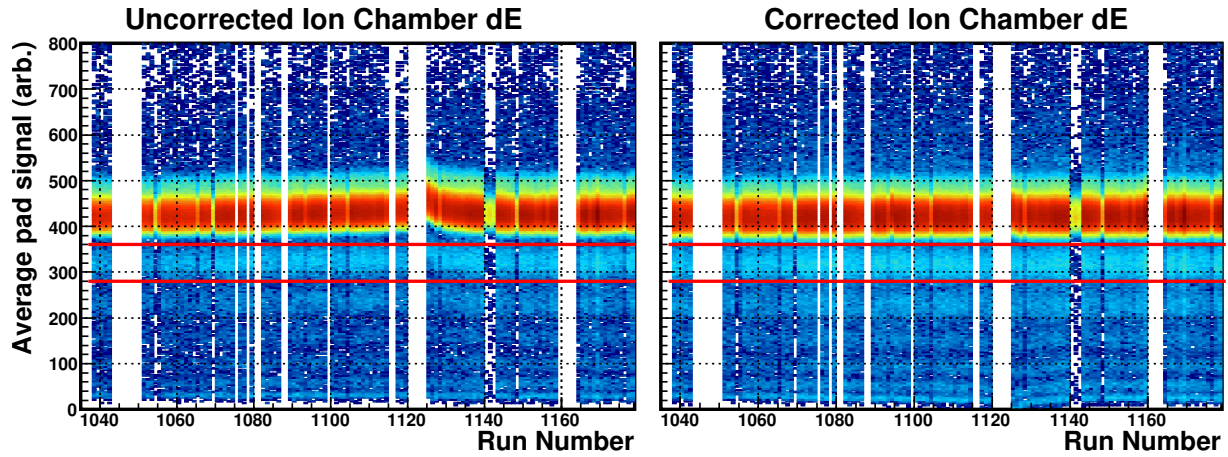


Figure 4.12: The average of the ion chamber pad signals before (left) and after (right) the correction. A ^{27}F beam gate has been applied. The horizontal bands correspond to reaction products with different Z . The band between the red horizontal lines corresponds to oxygen reaction products. The correction was made to straighten this band in order to more cleanly select oxygen reaction products.

where m_i is the gain matching scale factor and $b_i(r)$ is the offset for run r . The result of the drift correction is shown in Figure 4.12.

4.1.2.4 Thin scintillator

The thin scintillator was located 9.5 cm behind the ionization chamber and measures ion energy loss and provides a timing signal for a time-of-flight (ToF) measurement. The detector has four

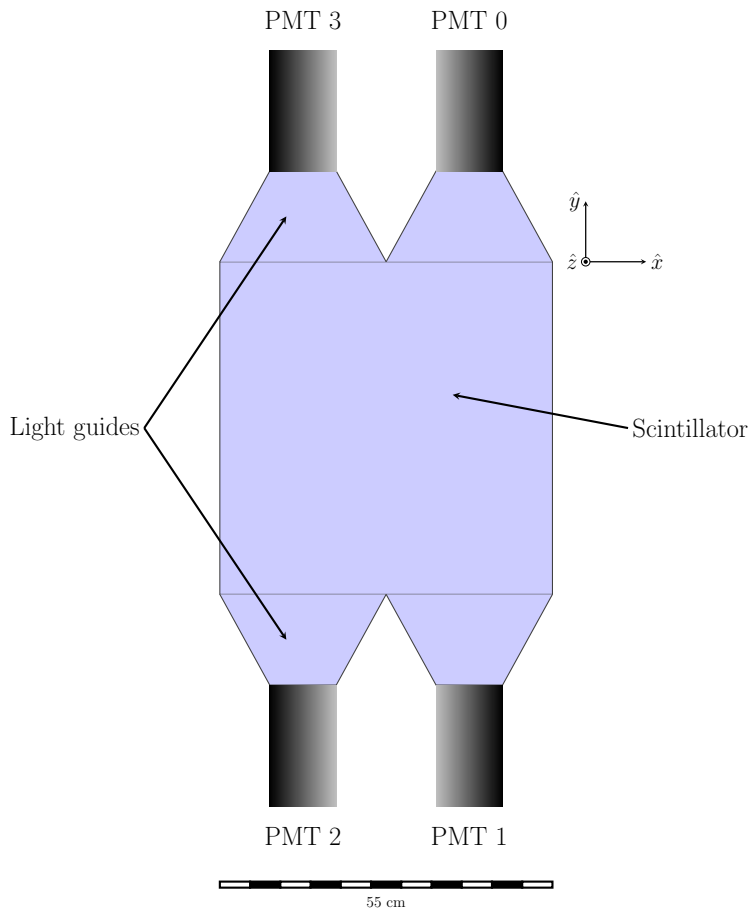


Figure 4.13: Diagram of the thin scintillator with its four PMTs.

PMTs two connected to the top edge of the scintillator and two connected to the bottom edge. Signals from each PMT are split to provide timing and energy loss measurements. The ToF measurement between the target scintillator and the thin scintillator was crucial for the analysis. Inhomogeneity and attenuation in the plastic can introduce small variations in the timing signal from each PMT; this, in turn, affects the ToF measurement. A series of three corrections were made to the ToFs measured between the target scintillator and each of the four thin scintillator PMTs. The four measurements were corrected against the energy loss measurements and the x and y positions measured by CRDC2. After these corrections the timing signals were averaged together and the difference between this average and the target scintillator was taken as the measured ToF.

The raw ToF between the target PMT and each of the thin PMTs was first checked against the charge-collected signal from the target PMT. There was no correlation between the measured en-

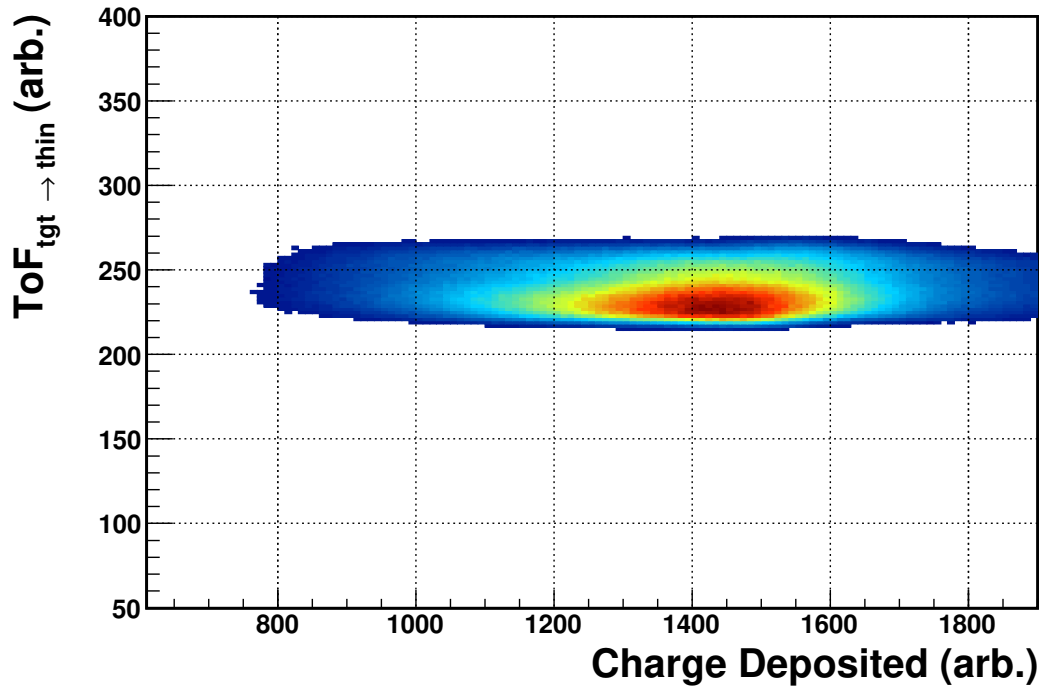


Figure 4.14: The raw, uncorrected ToF between the target and thin PMT 0 is plotted versus charge deposited in the target scintillator. There is no correlation between the two measurements. The spectra for the other three thin scintillator PMTs are similar to this one.

energy loss in the target scintillator and the target-thin ToF, see Figure 4.14. Therefore the measured ToF does not depend on the size of the signal produced by the incoming beam in the target scintillator. This is because the beam spot was small and localized on the smaller (~ 7 cm) target scintillator compared to the large spot size of the unreacted beam after the dispersive Sweeper magnet on the larger thin scintillator. The effects of inhomogeneity and attenuation are much smaller in the small scintillator when the light is always produced in roughly the same place.

Next, the raw ToFs (target to each thin PMT) were plotted against the energy loss signals from each of the thin's PMTs to correct for variations in the ToF due to the signal size. The energy loss versus ToF for each PMT was plotted for a subset of events that were identified as unreacted ^{27}F (see Section 4.2.2) and passed through a $10 \times 10 \text{ cm}^2$ window at the center of the unreacted beam spot as measured on CRDC2. The narrow position gate ensures that events used for the correction have similar fragment trajectories; otherwise the correction could reduce the sensitivity of the ToF measurement. The correlations shown in the left column of Figure 4.15 were found to be identical

for four other position gates. The results of the q-correction are shown in the right column of Figure 4.15.

The q-corrected ToFs were then corrected against CRDC2 x position to compensate for variations in the timing signals generated by light production in different regions of the scintillator. The data used for this correction were recorded while the Sweeper magnetic field was ramped up and down so that the unreacted ^{27}F (at a known velocity of 10.300 ± 0.008 cm/ns) is swept across the charged particle acceptance. The ~ 3 ns variation between the average ToFs measured for events passing through the edges of CRDC2 (see Figure 4.16) is assumed to be due entirely to variations in the timing signal induced by nonuniform light collection. Variation in the ToF due to beam energy spread and different path lengths as well as the ToF resolution contribute to the width of the distribution. A similar procedure generated a final correction from the qx-corrected ToFs versus CRDC2 y (see Figure 4.17).

The final calibrated ToF measurements for unreacted ^{27}F is shown as the red histogram in Figure 4.18. An offset applied to the qxy-corrected distribution was determined in order to center the velocity distribution on the 10.3 cm/ns value determined from energy loss calculations. Starting from the beam energy determined by the A1900 settings, the unreacted ^{27}F beam velocity after the segmented target is determined to be 10.3 cm/ns by computing the energy loss through the materials in the segmented target. The path length along the beam axis from the segmented target through the Sweeper to the thin scintillator was measured to be 429 cm. Calculating the velocities

$$v = \frac{429 \text{ cm}}{t}$$

for events that very nearly follow the beam axis (this is accomplished by gating on a 10×10 cm² central region in the CRDC2 xy spectrum) produces a roughly Gaussian distribution. Finding the offset (41.7 ns) needed to center the distribution on 10.3 cm/ns is the final step in calibrating the ToF measurement.

It is important to note that this offset folds in a second adjustment. Recall that the ToF is the measured time difference between timing signals from the target and thin scintillators. This measurement includes the additional time it takes the beam to travel 103 cm from the target scintillator

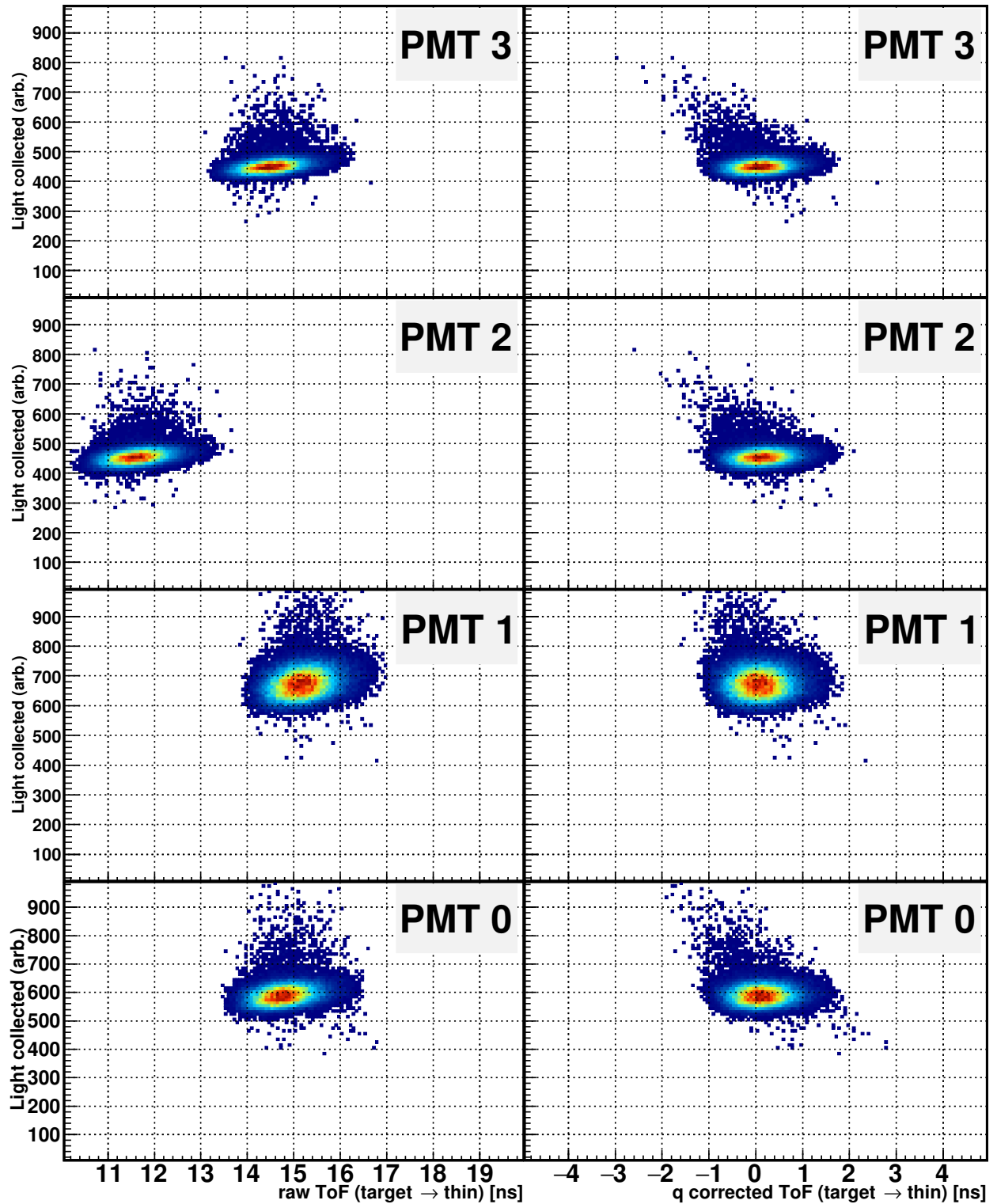


Figure 4.15: Left column: raw energy loss versus ToF between target and thin scintillators; a scale factor was applied to the x-axes to convert TDC channel number to ns. Right column: results of correcting each ToF measurement against the signal size in each PMT. The raw energy loss signals did not need to be gain matched since independent corrections were extracted separately for each PMT.

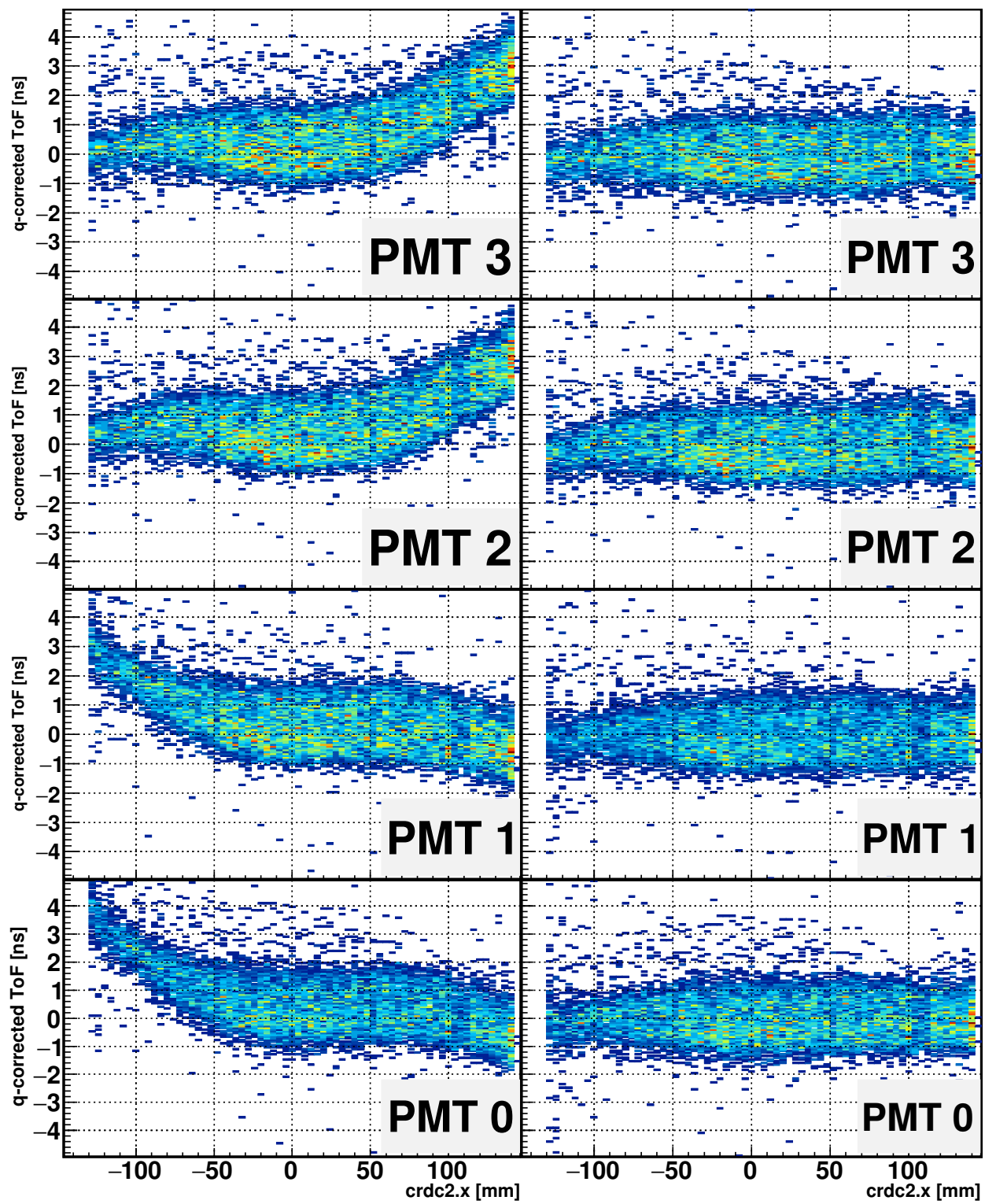


Figure 4.16: Left column: q-corrected ToF versus x position measured in CRDC2. Right column: results of the x position correction.

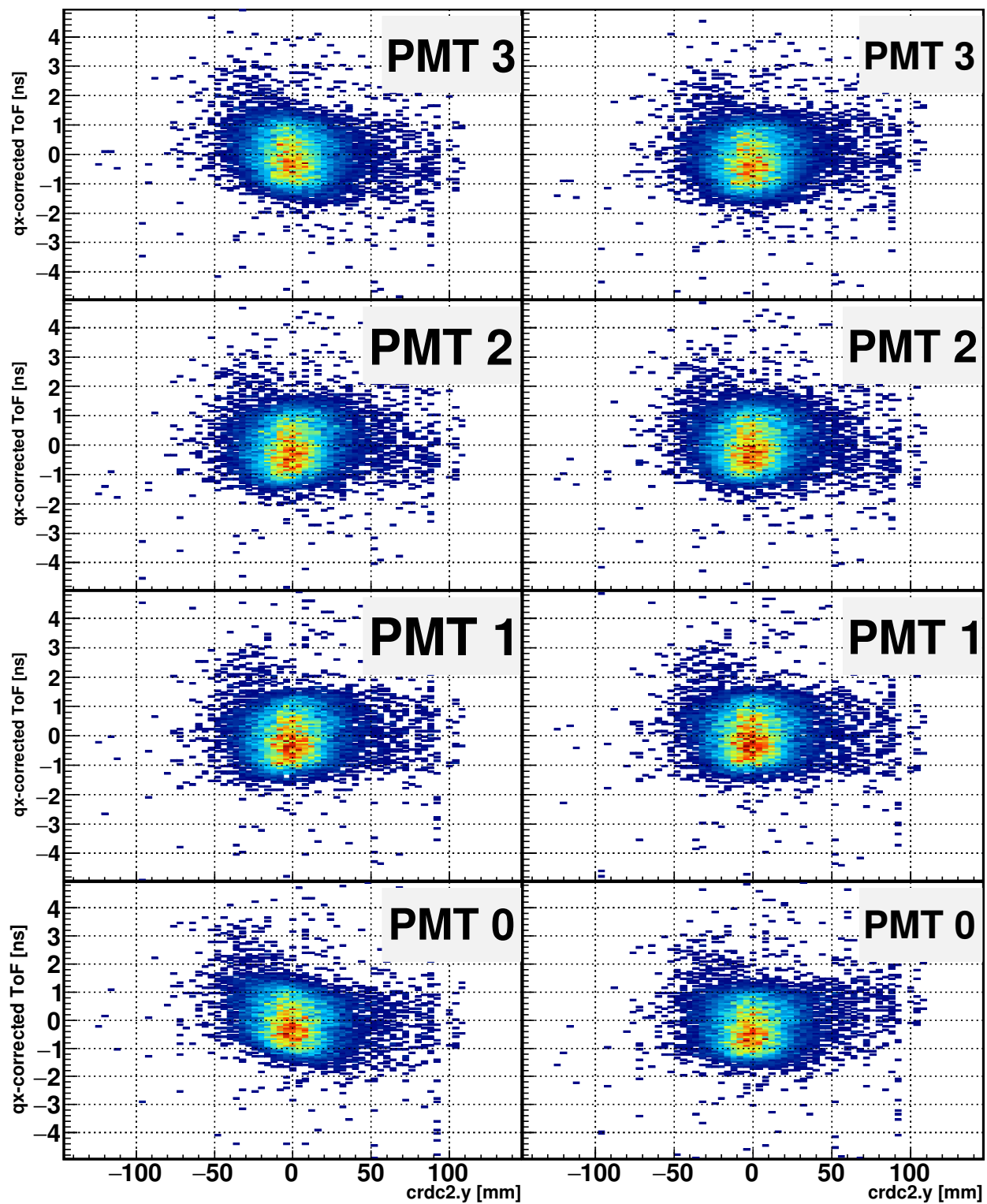


Figure 4.17: Left column: qx-corrected ToF versus y position measured in CRDC2. Right column: results of the y position correction.

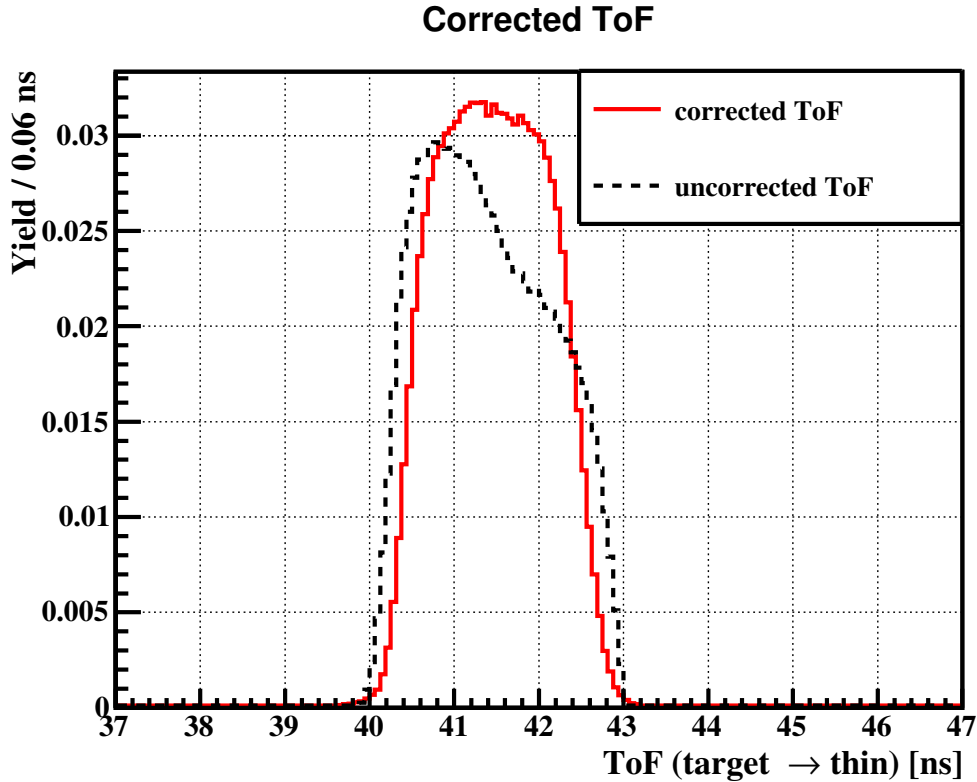


Figure 4.18: The uncorrected (black dotted histogram) and corrected (solid red histogram) ToF distributions for unreacted ^{27}F calculated as the event-by-event average of the thin PMT signals. An offset has been applied to center the velocity distribution on the value determined from energy loss calculations of the ^{27}F beam through the segmented target (see text).

to the segmented target. By setting the offset to reproduce the velocity of unreacted ^{27}F after the segmented target, the flight time from scintillator to target is removed. This means that the offset in the calibration is only valid for events from the ^{27}F beam.

4.1.3 MoNA-LISA

The signal output from each PMT on the MoNA/LISA bars provides a charge and a time measurement. The PMT converts scintillation photons into an electrical signal. One copy of the signal is processed by a constant fraction discriminator (CFD) and used to measure the arrival time of the signal. Another copy is integrated to measure the total amount of scintillation light produced by the interaction of a photon, neutron, or charged particle with the bar. The terms “charge” and “light” are both used to refer to the amount of scintillation light produced. A series of calibrations

are needed to convert these measurements into deposited charge, interaction time and position (x) along the bar. The orientation of the lab frame coordinate axes are shown in Figure 3.1; the y, z coordinates are determined by the positioning and discretization of the bars.

First, each PMT was gain matched and the charge measurements calibrated. Then the TDC for each PMT was calibrated, and subsequently, a conversion from time difference to position along the bar was extracted. A timing offset was then determined to place each bar in time relative to the first layer on each table and finally to place each table relative to the target. All of these calibrations (except for the final timing offset) were performed using cosmic ray muon measurements. Muons produced in the upper atmosphere by cosmic rays uniformly illuminate the arrays and provide a means of calibrating the positions and timing of individual bars. The MoNA/LISA acquisition systems were set to operate in standalone mode for these measurements so no coincidence with the Sweeper detectors was required.

Cosmic ray muon data were taken before and after the experiment using individual layers of MoNA and LISA and using the entire array. Muons from cosmic rays deposit roughly 2 MeV/cm (84) as they pass through about 10 cm of scintillating material depositing approximately 20.5 MeV electron equivalent (MeVee) of light in each bar. Since the light yield in organic scintillators is dependent on the type of particle, units of electron equivalent energy deposited are used to quantify the absolute amount of light produced. One MeVee is equal to the light produced by an electron with 1 MeV of kinetic energy. Since the muons travel at close to the speed of light (86) measuring them provides an ideal metric for calibrating the relative timing between bars.

4.1.3.1 Charge Calibration (QDC)

The first step in calibrating the charge/light deposited was to roughly gain match the PMTs by adjusting the applied voltage. This iterative process involved

1. Taking one hour of cosmic ray muon data
2. Extracting the muon peak from the uncalibrated QDC spectra for each PMT

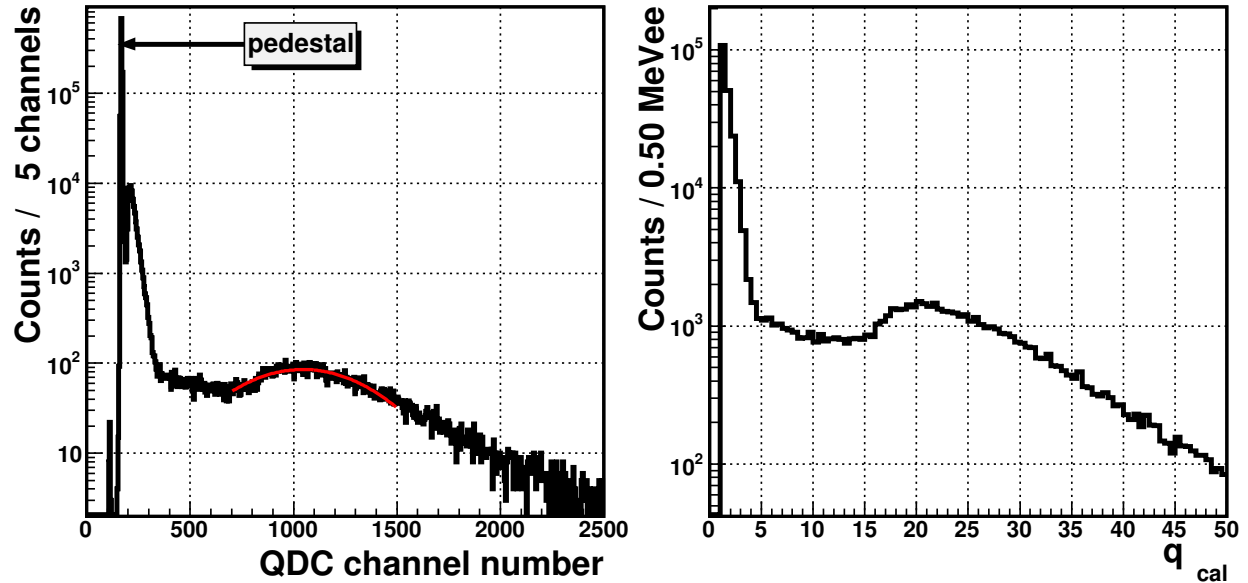


Figure 4.19: Example raw (left) and calibrated (right) QDC spectra. The pedestal visible in the left spectrum is suppressed using a hardware threshold during the experiment and while recording a subsequent cosmic run used to generate the right plot. The red curve is a Gaussian fit to the cosmic peak. The QDC channel numbers of the pedestal and the cosmic peak determined a scaling to convert QDC channel number to light deposited in units of MeVee. The muon peak appears ~ 20 MeVee in the calibrated spectrum.

3. Calculating and applying a new voltage setting to adjust the position of the muon peak

This process was repeated until the cosmic peak was positioned around channel 1000 in all QDC spectra. Final voltage settings ranged from 1400 V to 1950 V.

The charge-to-digital converters (QDC) used to integrate the signal current and determine charge have a small inherent bias current referred to as a pedestal. The pedestal was suppressed during the experiment using a hardware threshold. Without this threshold, every QDC channel would be read out for every event thus causing significant dead time. However, this threshold was turned off when taking cosmic ray data for the QDC calibration so that the uncalibrated QDC bin number of the pedestal could be identified and used to set the thresholds. The pedestal corresponds to a charge signal of zero and was used as one point in a linear calibration, along with the bin number of the cosmic peak, to convert uncalibrated QDC spectra to units of MeVee.

The QDC calibration is extracted from a cosmic ray data set taken after all PMTs have been gain matched. The linear conversion from QDC channel number to MeVee for each PMT is determined

from the pedestal and the fit to the cosmic peak

$$q_{\text{cal}} = m_q(q_{\text{raw}} - q_{\text{ped}})$$

where $m_q = 20.5/(q_{\mu}^{(\text{raw})} - q_{\text{ped}}^{(\text{raw})})$ in units of MeVee/ch is the QDC slope that calibrates the muon peak to 20.5 MeVee; $q_{\mu}^{(\text{raw})}$ is the QDC channel number corresponding to the fitted centroid of the muon peak. The quantity $q_{\text{raw}} - q_{\text{ped}}$ subtracts the integrated charge due to the pedestal from measurement. The hardware threshold is calculated as

$$q_{\text{thresh}} = \frac{q_{\text{ped}}}{16} + 2$$

The factor of 16 converts the pedestal channel from 12 bits to 8 bits since the QDC modules record measurements as 12 bit numbers and store the thresholds as 8 bit numbers. The 2 assures that the threshold is placed above the pedestal. Thresholds ranged from 0.5 to 1.0 MeVee and a post-experiment software threshold of 1.0 MeVee was applied to all PMTs and also to simulation output. An example of the QDC calibration is shown in Figure 4.19 for the right PMT of bar J-14.

4.1.3.2 Timing and x position calibration

The signal from each PMT is processed by a constant fraction discriminator (CFD) to generate a logic pulse that provides the start signal for a time-to-digital converter (TDC) to measure the temporal separation between particle interactions in the arrays. A TDC operates like a stopwatch: when it receives a start signal from the CFD it begins charging a capacitor until it receives a stop signal from the logic system. The amount of charge on the capacitor corresponds to the amount of time between the start and stop signals. There are variations between the capacitors in different TDCs so a slope must be calculated to convert from TDC channel number to time for each TDC. This process used an Ortec NIM Time Calibrator module (Module 462) which provides start and stop pulses separated by specific intervals. The interval was set to 40 ns and the range to 350 ns so that the start and stop signals were separated by an integer multiple of 40 ns no greater than 350 ns (40 ns, 80 ns ... 320 ns). The top panel in Figure 4.20 shows an example of an uncalibrated

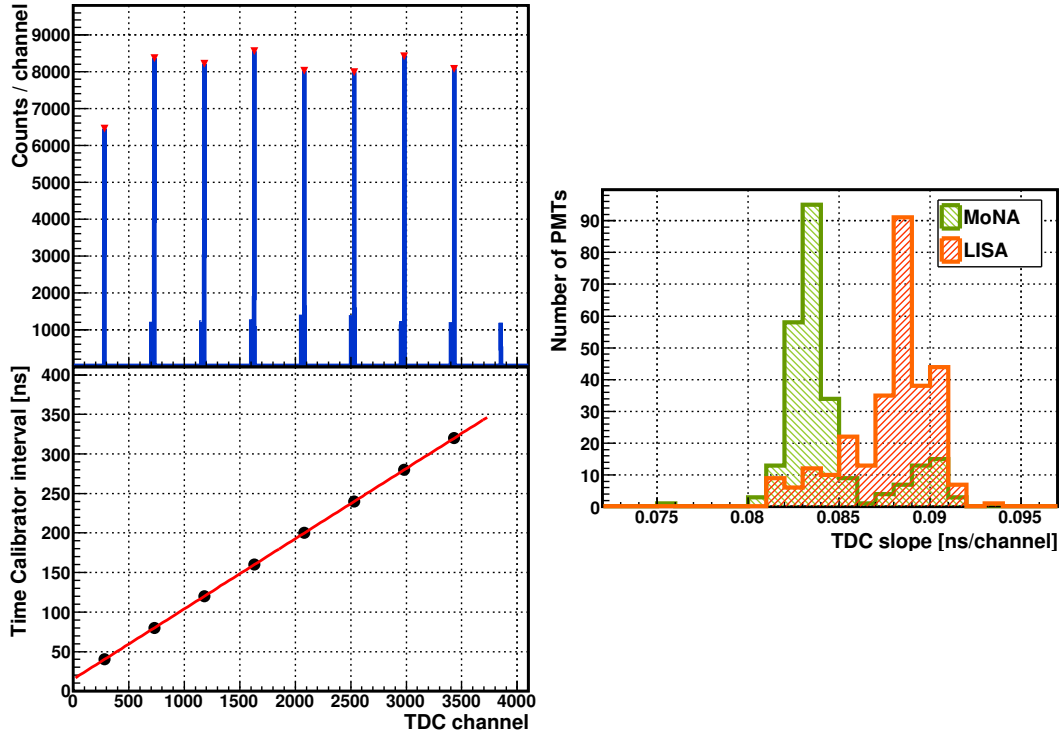


Figure 4.20: An example of an uncalibrated TDC spectrum (top panel) generated using the time calibrator. The narrow peaks represent recorded events where the time between the start and stop pulses is an integer multiple of 40 ns. The known time intervals are plotted against the peak locations (bottom panel) to extract a scale factor that converts TDC channel number to a time. The right panel displays histograms of the calculated TDC slopes.

TDC spectrum produced using the time calibrator. The structure results from the $\Delta t = n \times 40$ ns intervals ($n = 1, 2, \dots, 8$) between start and stop pulses. The time intervals set by the time calibrator are plotted against peak locations (see the bottom panel of Figure 4.20) to extract a conversion from TDC channel number to time. A separate conversion factor is calculated for every TDC channel in MoNA and LISA and they are plotted in the right panel of Figure 4.20.

Once the PMT timing measurements are calibrated, the time difference between left and right PMTs can be used to determine the position along the bar where an interaction produced scintillation light. Cosmic ray muons illuminate the entire length of a bar so the time difference spectrum from a cosmic muon data set is used to calibrate the x positions using the left and right edges of the detector. An example of a left-right time difference spectrum is plotted in the left panel of Figure 4.21. Separate fits of the form

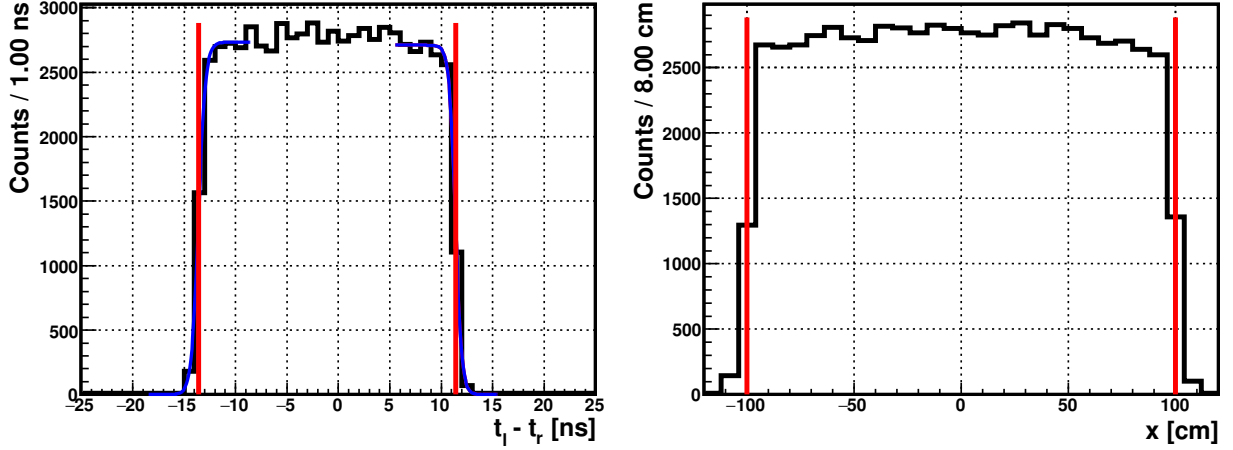


Figure 4.21: In the left panel, the black histogram plots the difference between calibrated times $t_{\text{left}} - t_{\text{right}}$, the blue curves are Fermi function fits to the left and right edges of time difference distribution and the red vertical lines are the edges extracted from the fits. The right panel shows the resulting x position spectrum. Events plotted in these spectra are required to have a calibrated light deposited signal > 4 MeVee.

$$f(x) = \frac{a}{1 + \exp[b(x - c)]},$$

are used to extract the left and right edges of the distribution (a , b , c are fit parameters). The edges are then used to calculate a scale factor that converts time difference to position and an offset that centers the distribution in the bar's reference frame. An example of a calibrated x position spectrum is shown in the right panel of Figure 4.21.

Once the left-right time difference for every bar has been calibrated to an x position, the coordinate system for each bar must be converted to the lab coordinate system. This was achieved using the results from a survey that measured the planes of the front layers on each table (see Section 3.7) relative to the target location. This measurement was used to determine the orientation of the “table coordinate systems” by defining a vector connecting the target location to the center of each of the front layers. Ultimately, the alignment of these vectors with the theoretical beam axis was better than 2° . This translates to an adjustment ~ 0.1 cm which is roughly an order of magnitude smaller than the ~ 7 cm position resolution of the bars. Therefore, the layers were taken to be perpendicular to the beam axis. The coordinate transformations from each bar system to the

lab system have the form

$$x = x' + x_0$$

$$y = y' + y_0$$

$$z = z' + z_0$$

where the unprimed coordinates correspond to the lab system, the primed coordinates correspond to the bar system and (x_0, y_0, z_0) specify the lab coordinates of the bar centers.

4.1.3.3 Timing offsets

The relative timing between signals in each MoNA/LISA bar must be known in order to accurately measure the neutron flight time. The time of a particle interaction inside a bar is determined by the average of the two PMT times, but an offset must be determined to correctly calibrate the measured time relative to the target. The procedure for determining this offset involves finding offsets that correctly set the timing (1) between bars and (2) relative to the target. Offsets between bars (1) can be determined using cosmic ray data while x-rays and γ -rays from the target can be used to determine offset (2). The cosmic ray muon velocity is approximated as 29.8 cm/ns and is used to set the timing for events where the muon passed through all 16 bars in a layer or through multiple bars on a table.

First, offsets are calculated to set the timing of all bars in a layer relative to the top bar. For muons travelling through a layer the travel time is

$$t = \frac{d}{v_\mu} \quad (4.2)$$

where $d = \sqrt{(x_1 - x_0)^2 + (y_1 - y_0)^2}$ is the distance between interactions determined by the calibrated x position and the physical y location of the bars; $v_\mu = 29.8$ cm/ns is taken to be the muon speed. The difference between the observed and the expected time is the offset.

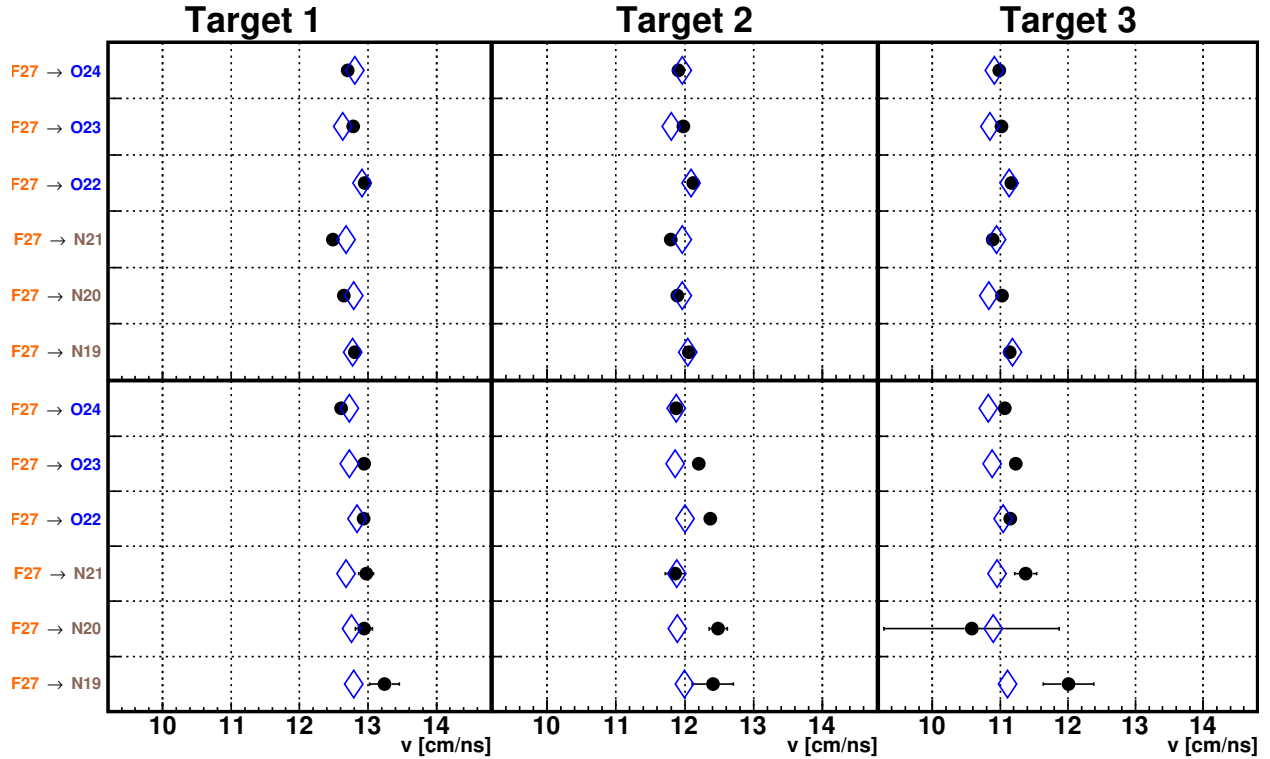


Figure 4.22: A χ^2 minimization routine was used to fit Gaussian functions to the fragment and neutron velocity distributions; the centroids and fit errors are plotted for data (black circles) and simulation (open blue diamonds). The fit results for the fragment velocities are plotted in the top row and the neutron velocities in the bottom row. The left, middle and right columns correspond to fit results where the distributions are made from events where the reaction occurred in the first, second and third beryllium target, respectively.

Next, offsets for each layer are determined to set the relative timing between layers on a single table. Equation 4.2 is again used to calculate the expected time where now

$$d = \sqrt{(x_1 - x_0)^2 + (y_1 - y_0)^2 + (z_1 - z_0)^2}.$$

where z is determined by the physical location of each layer. The difference between the measured and expected times is the offset that sets the timing between layers on a table.

The final step is to determine an offset for each of the three tables that correctly sets the timing relative to the target. Since the rate of muons passing through bars on separate tables was negligible, γ -rays from the target were used to determine this final offset. Just prior to the start of the experiment, a 6.35 mm aluminum block was placed in the target position and a 140 MeV/u ^{48}Ca beam was directed onto it. Neutrons, light charged particles and γ -rays from the fragmentation of

MoNA Offset [ns]	LISA-1 Offset [ns]	LISA-2 Offset [ns]
453.1	443.5	442.5

Table 4.4: Final time offsets for each MoNA/LISA table.

^{48}Ca were measured in MoNA and LISA. These measurements were used to determine one timing offset for each of the three tables such that (1) the gamma peak in the velocity spectrum was located at 29.979 cm/ns and (2) the neutron/light charged particle peak in the velocity spectrum was between 10.0 cm/ns and 14.5 cm/ns corresponding to the beam velocities at the front and back edges of the aluminum block. The global timing offsets extracted for each table in this way needed one adjustment to account for the difference in flight times for the ^{48}Ca ($v = 14.8$ cm/ns) and ^{27}F ($v = 13.2$ cm/ns) beam particles over the 103 cm distance from the target scintillator to the target position. This offset was calculated as

$$\begin{aligned}
 t_{\text{offset}} &= \frac{103}{v(\text{F})} - \frac{103}{v(\text{Ca})} \\
 &= 0.8 \text{ ns.}
 \end{aligned}$$

The final timing offsets were checked by comparing the measured and simulated neutron velocities for six different species of reaction fragments produced from the ^{27}F beam fragments; see Figure 4.22. The final timing offset values are listed in Table 4.4.

4.2 Event Selection

During the experiment, more than 50 million events were recorded. Included in this data set are events resulting from background physics processes, events where one or more of the decay products were not detected and events with incomplete information in one or more detectors. This section describes how the data set was “cleaned” to extract events resulting from a complete and reliable measurement of the $^{27}\text{F}(-1p) \rightarrow ^{26}\text{O} \rightarrow ^{24}\text{O} + 2n$ process of interest.

Beam Fragment	Velocity [cm/ns]	Flight time [ns]	Fraction [%]
^{27}F	13.21	74.5	15
^{28}Ne	13.96	70.5	36
^{29}Ne	13.58	72.5	8
^{30}Na	14.25	69.0	18

Table 4.5: Velocities, flight times and fraction of total events in the dE-ToF spectrum for the four most intense beam fragments. The velocities are calculated based on the central rigidity (4.5798 Tm) of the last dipole magnet before the target and the flight times are based on the 983.8 cm flight path between the A1900 and target scintillators. The remaining 23% of events either fall outside the strict 2D graphical cuts or resulted from low Z beam fragments.

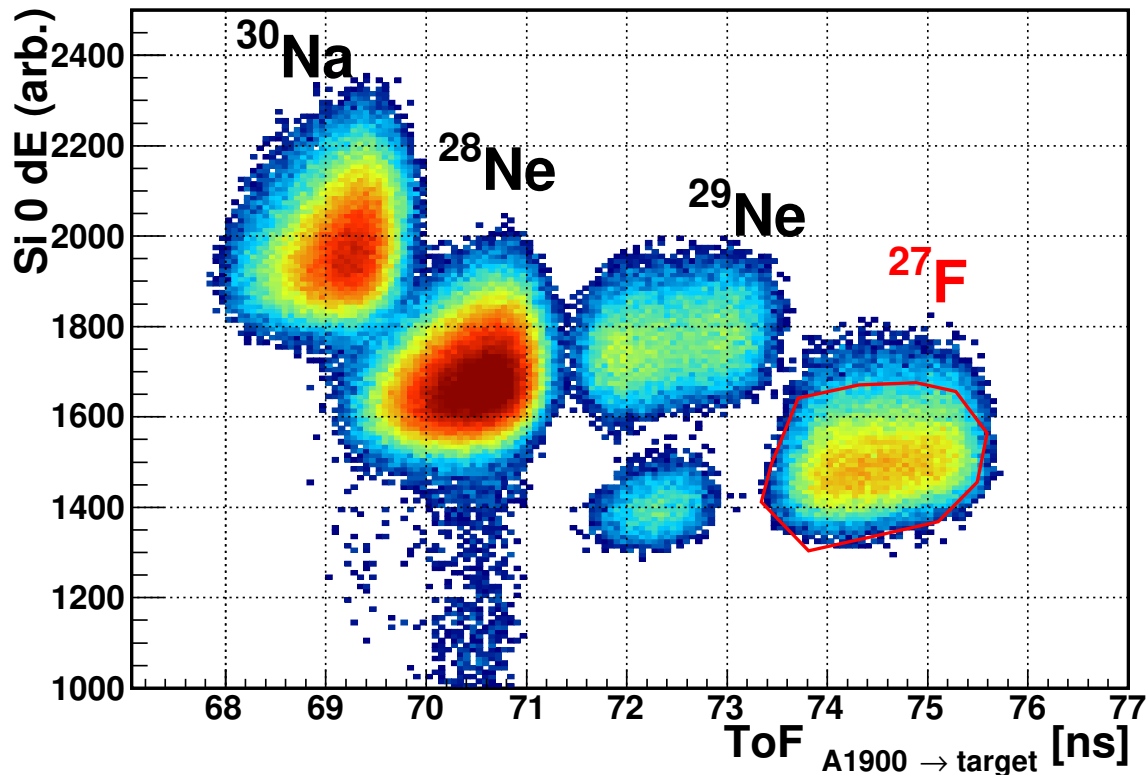


Figure 4.23: Spectrum used for beam fragment identification. The faster fragments (see Table 4.5) have a shorter ToF (x-axis) and fragments with a higher Z deposit more energy in the first silicon detector (y-axis).

4.2.1 Beam Identification

The A1900 delivered the ^{27}F secondary beam along with three additional species of beam fragments: ^{28}Ne , ^{29}Ne , ^{30}Na and a number of other low Z fragments resulting from reactions in the aluminum wedge. The central rigidity of the magnet before the target was set to 4.5798 Tm in order to transport the beam fragments from the A1900 into the experimental area. The velocities at which the beam fragments traveled from the end of the A1900 to the target are listed in Table 4.5. The time-of-flight (ToF) between the A1900 and the target scintillator along with the energy lost by the beam fragments in the segmented target's first silicon detector (Si0) were used to identify beam fragments event-by-event. The ToF measurement was sufficient to separate ^{27}F from the other beam fragments because nuclei with the same $B\rho$ but different A and Z will have different velocities. The light fragments were filtered out using the Si0 energy loss (dE) measurement because the energy lost in the silicon is proportional to Z^2/v^2 . A 2D graphical cut shown in Figure 4.23 was generated to place a tight gate on the ^{27}F events. Using these measurements the fraction of events identified as ^{27}F in the dE -ToF spectrum beam was calculated to be 15%. Table 4.5 summarizes the fraction of events identified as each of the four main beam fragments.

4.2.2 Element Identification

Many reaction products were expected from the fragmentation of ^{27}F in the beryllium targets, but only those reaction products that produced a signal in the thin scintillator were recorded. The Sweeper magnet was set to a central $B\rho = 3.445$ Tm (306 A) corresponding to the expected energy of ^{24}O reaction fragments after the segmented target. The acceptance of the sweeper is $\pm 8\%$ in rigidity so only those reaction fragments with momenta in this range after the segmented target reached the thin scintillator. For this experiment, the fragments of interest were ^{22}O and ^{24}O .

Identifying the charge ($q = Ze$) of a reaction fragment utilizes the correlation between the energy loss (dE) measured in the ionization chamber and the time-of-flight (ToF) from the target to the thin scintillator. Figure 4.24 plots the dE measured in the ionization chamber against the ToF from the target to the thin scintillator requiring the first silicon dE and A1900-to-target-scintillator

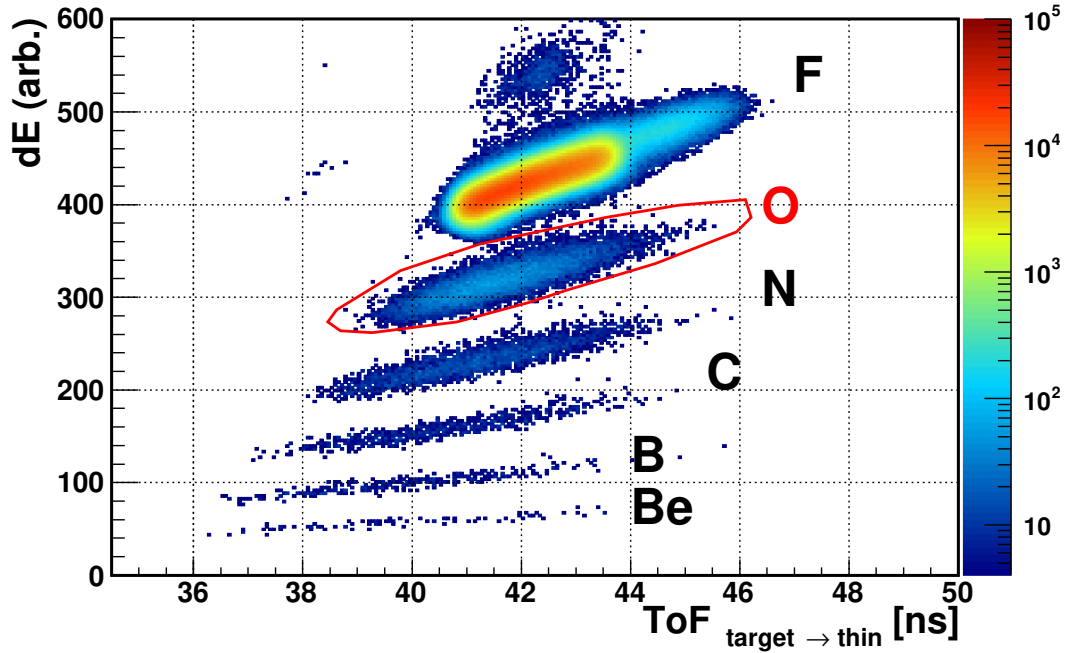


Figure 4.24: Energy loss (dE) measured in the ionization chamber versus the time-of-flight from the target to the thin scintillator. Only events that fall inside the ^{27}F beam gate (see Figure 4.23) are plotted here. The most intense region corresponds to unreacted ^{27}F beam fragments ($Z = 9$); the band immediately below corresponds to oxygen ($Z = 8$) reaction products $^{27}\text{F}(-1p) \rightarrow ^A\text{O}$.

ToF measurements to fall inside the ^{27}F beam gate. Groups with $Z = 9, 8, 7, 6, 5,$ and 4 are discernable and a 2D gate on the oxygen band was used to select events where a one-proton knockout reaction took place. For some calibration procedures a 2D gate was placed on the intense region in the fluorine band to select events where no reaction occurred in the segmented target.

4.2.3 Isotope Identification

Once the charge ($q = Ze$) of the reaction fragment is identified, the mass number (A) must be determined. The magnetic rigidity of a non-relativistic charged particle can be written as

$$B\rho = \frac{mv}{q},$$

and its velocity $v = \Delta L/\Delta t$. With these two relations, it can be shown that the time-of-flight through a magnetic field is proportional to the fragment mass Am_u

$$v = \frac{\Delta L}{\Delta t} = \frac{B\rho q}{m} = \frac{B\rho Ze}{Am_u} \propto \frac{1}{A} \quad (4.3)$$

where $q = Ze$ is the charge, L is the path length of the trajectory through the magnetic field, t is the time-of-flight, A is the number of nucleons and m_u is the nucleon mass. Thus different isotopes with constant $B\rho$ (constant momentum) can, in principle, be mass-separated by measuring time-of-flight.

In reality, the time-of-flight (ToF) distributions for different isotopes are broad and overlap due to variations in both L and $B\rho$. These variations arise from factors including the emittance of the beam, momentum acceptance of the fragment separator, straggling in the targets and silicon detectors, the nuclear dynamics associated with the knockout reaction and the momentum kick from the neutron decay. Additionally, the magnetic field of the Sweeper is not uniform due to its 14 cm vertical gap. Nevertheless, the magnetic rigidity and L of the charged particles are related to their emittance measured after the Sweeper magnet. The correlation between time-of-flight, dispersive angle and position needs to be untangled to produce a “corrected” ToF parameter that can separate the different isotopes present in the oxygen band shown in Figure 4.24. Examples of the ToF-dispersive angle and position correlation is shown in Figure 4.26.

Calculation of the dispersive angle requires two position measurements after the magnetic field. Since the CRDC1 position measurement is unreliable for certain regions, the deconvolution was carried out separately for the lower left, middle and upper right regions outlined in red in Figure 4.25. The procedure is illustrated for the upper right region and the resulting mass-separating “corrected” ToF parameter is plotted in Figure 4.33.

The additional beam fragments that arrived with the ^{27}F included the same oxygen isotopes $^{22-24}\text{O}$ as the reaction fragments of interest. Events where these oxygen beam fragments were measured are selected by gating on the oxygen band in the ionization chamber dE -ToF spectrum and on the Si 0 and A1900-to-target dE -ToF spectrum. The ToF distributions from these unreacted

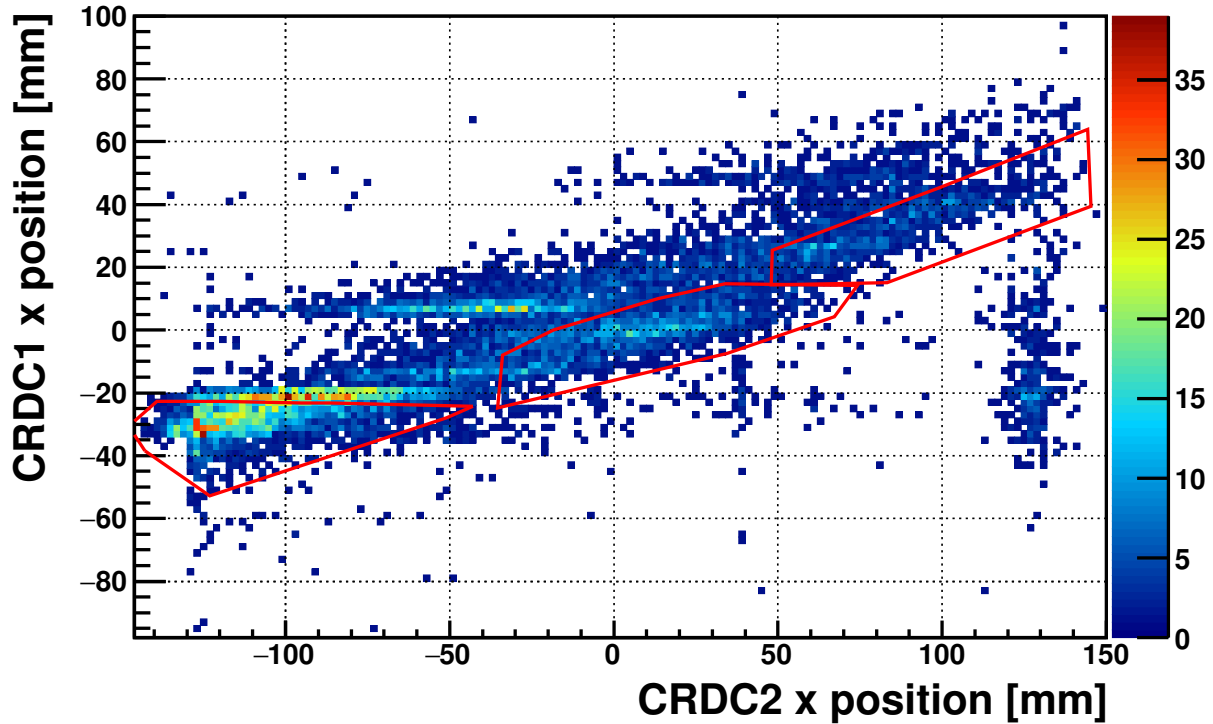


Figure 4.25: CRDC1 x position versus CRDC2 x position; Two functioning detectors would display a smooth, positive correlation. The red lines outline 2D gates that attempt to select events with a good CRDC1 position measurement.

oxygen beam events do not exhibit the same broadening resulting from the nuclear reaction dynamics and the momentum kick since they do not undergo a reaction. As a result they can already be mass-separated using the uncorrected ToF measurement. Furthermore, the oxygen beam fragments lose less energy in the segmented target than the ^{27}F beam, therefore they enter the Sweeper with a higher $B\rho$ than the oxygen reaction fragments which means they are detected on the $+x$ side of CRDC2 ($50 \leq x \leq 150$ mm) while most of the oxygen reaction fragments are detected with CRDC2 $x < 100$ mm. Compared to the oxygen reaction fragments, the beam fragments provide a cleaner starting point for deconvolving the ToF-dispersive angle and position relations (see Figure 4.26) as well as higher statistics especially in the upper right region of Figure 4.25.

The first step in generating the corrected ToF is to construct a single parameter that describes the dispersive plane emittance, both angle and position. This is accomplished by projecting a 3D scatter plot of ToF versus dispersive angle versus dispersive position onto the dispersive angle and

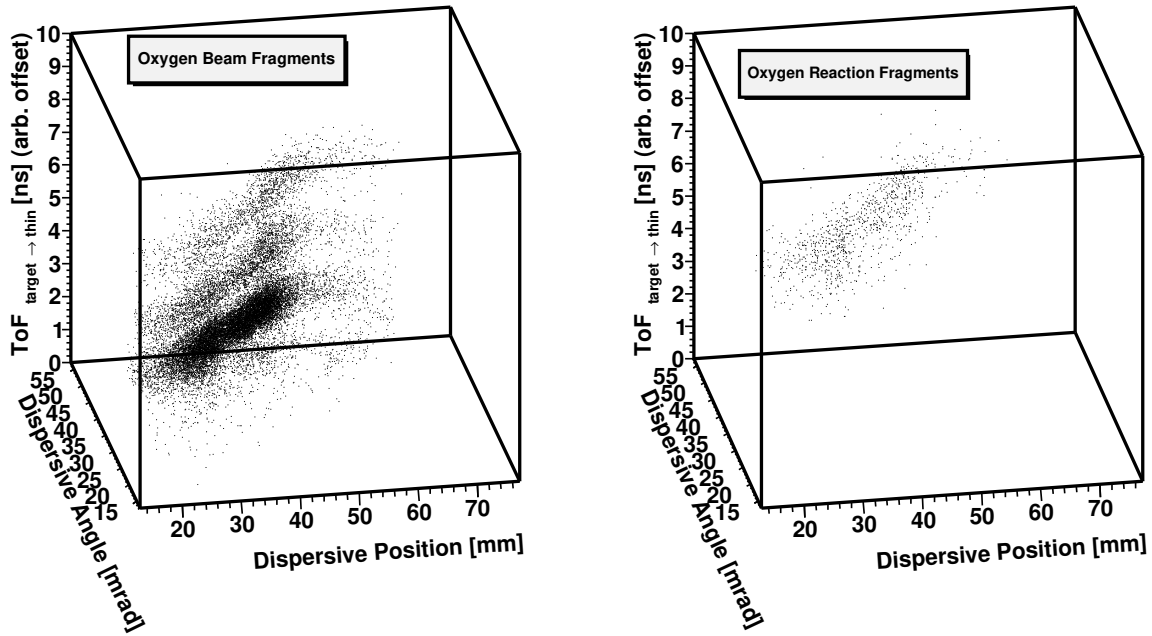


Figure 4.26: The correlation between ToF dispersive angle and position is shown for oxygen beam fragments on the left and oxygen reaction fragments from ^{27}F on the right.

position plane. The projection of the left 3D scatter plot in Figure 4.26 is shown in the top panel of Figure 4.27 where the color of each box in the grid indicates the mean of the distribution formed when the contents of the 3D cell are projected onto the ToF axis. Breaks in color indicate contours of iso-ToF which are fit with a second order polynomial

$$f(x) = p_0 + p_1x + p_2x^2$$

indicated by the black curve in the top panel of Figure 4.27. The fit result is used to construct a parameter describing both position and angle for constant ToF:

$$g(x, \theta_x) = \theta_x - f(x)$$

Plotting this parameter against ToF separates the different isotopes as shown in the bottom panel of Figure 4.27. A corrected ToF is constructed by rotating the ToF axis to lie perpendicular to the red line in the bottom panel of Figure 4.27 which is defined as

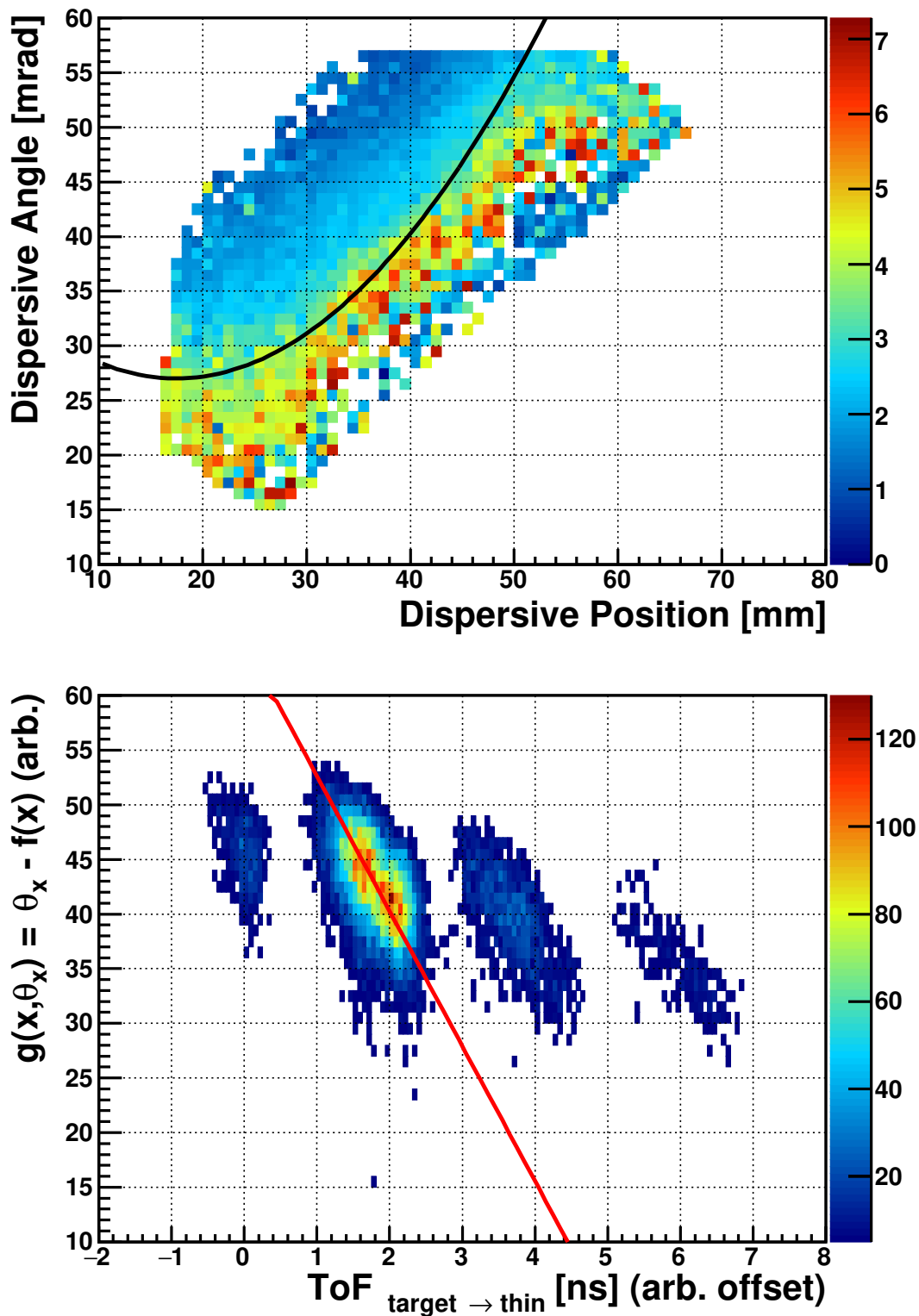


Figure 4.27: The top panel is a projection onto the 2D dispersive position versus dispersive angle plane. The iso-time-of-flight contour is shown in black. In the bottom panel the dispersive plane emittance parameter displays a linear correlation with measured ToF and can be projected onto an axis perpendicular to the red line for the purpose of making a 1D gate.

Iteration	Parameter	Left	Middle	Right
1	$g(x, \theta_x)$	0.13	0.08	0.08
2	Si 0 x	1.59	0.86	0.88
3	focus x	-0.01, -0.94	-0.01, 0.01	-0.01, 0.11
4	focus θ_x	0.01	0.03	0.01

Table 4.6: Iterative corrections to fragment time-of-flight used to achieve particle identification for the left, middle, and right regions identified in Figure 4.25. Note that two parameters are given for iteration three, the correction via focus x ; this is because that correction had the form $t_{\text{corr3}} = t_{\text{corr2}} - (p_2x^2 + p_1x)$ so the first and second values listed correspond to p_2 and p_1 respectively.

$$g(x, \theta_x) = m_0 t_{\text{target} \rightarrow \text{thin}} + b$$

where m_0 is the slope and b is an arbitrary offset. The corrected ToF is then

$$t_{\text{corr}} = t_{\text{target} \rightarrow \text{thin}} - m_0^{-1} g(x, \theta_x)$$

The separation is then improved by iteratively plotting other parameters against corrected ToF and removing any correlations according to the same procedure:

1. Plot a parameter or combination of parameters versus corrected ToF
2. Extract the form for a linear correlation between the corrected ToF and the parameter (combination)
3. Generate a new iteration of the ToF correction (t_i) according to $t_i = m_{i-1}^{-1} y$ where y is the parameter or combination of parameters
4. Compare plots of y versus t_i and y versus t_{i-1} to ensure that the new correction removes the correlation

The procedure for extracting a dispersive plane emittance parameter and then iteratively correcting the ToF was applied separately to each of the three regions outlined in Figure 4.25 using oxygen beam and/or reaction fragments depending on which data set had the best statistics for a given region. The parameters used for the corrections are listed in Table 4.6. The ToF corrections

were then applied to the oxygen reaction fragments from the ^{27}F beam and 1D gates for each of the three regions were generated to select the different isotopes. The CRDC2 x distributions under the isotope gates were then checked for the correct trend between ToF and dispersive position.

Reaction products with different masses produced from the same beam should have roughly the same velocities. This implies that the momentum ($B\rho$) for a heavier reaction product will be larger than that of a lighter mass one. Upon passing through the Sweeper magnet, the heavier reaction products will be bent less and take a slightly longer path through the magnet resulting in a longer flight time. Therefore, the heavier mass reaction products should have a longer ToF and more positive CRDC2 x distributions compared to the lighter reaction products. Figures 4.28 - 4.30 illustrate the trend between ToF and CRDC2 x position.

The corrected ToF is sufficient to separate isotopes but it does not identify masses. Recall from Eq. 4.3 that the energy loss is proportional to Z^2/v^2 . Assuming non-relativistic kinematics and that $B\rho$ remains constant, recall also that $B\rho = p/q = mv/Ze$ from which it follows that

$$v^2 = \frac{(B\rho Ze)^2}{m^2} \propto \frac{Z^2}{A^2},$$

$$\Delta E \propto \frac{Z^2}{v^2} \propto \frac{Z^2}{(B\rho Z)^2} A^2 \propto A^2$$

Since ToF is inversely proportional to velocity, measurements of ΔE and ToF can separate events according to A^2 and A/Z . Figure 4.31 illustrates how nuclei are arranged according to these two parameters. Note that nuclei with integer values of A/Z lie along a vertical line perpendicular to the A/Z axis. It is then straightforward to identify groups of events plotted in Figure 4.32. The group at the top are unreacted ^{27}F and the ^{24}O reaction fragments lie directly beneath them.

The one dimensional corrected ToF is plotted in Figure 4.33 for the oxygen reaction products. A region-dependent offset was applied to the corrected ToF parameter from each of the three separate regions indicated in Figure 4.25 to align the three spectra. This parameter is referred to as the global corrected ToF.

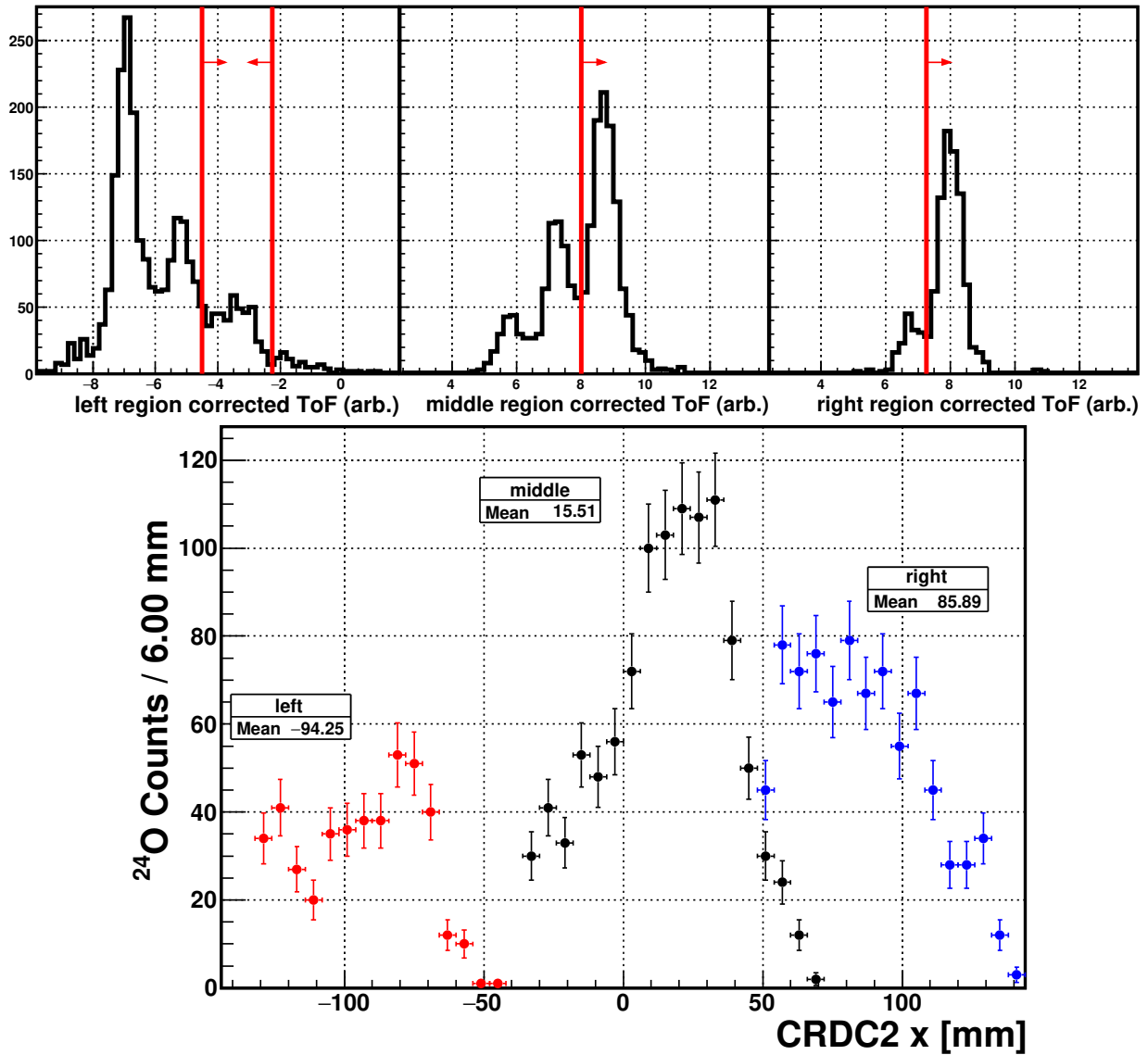


Figure 4.28: The top three panels plot the corrected ToFs for the three different regions. For each region a 1D gate is indicated by the red lines and arrows, and is applied to the CRDC 2 x distributions plotted in the bottom panel. The red, black, and blue points plot the CRDC2 x distributions for events under the left, middle, and right region gates respectively. These gates select events where the oxygen reaction products have a long ToF and are detected on the high rigidity (+ x) side of CRDC2.

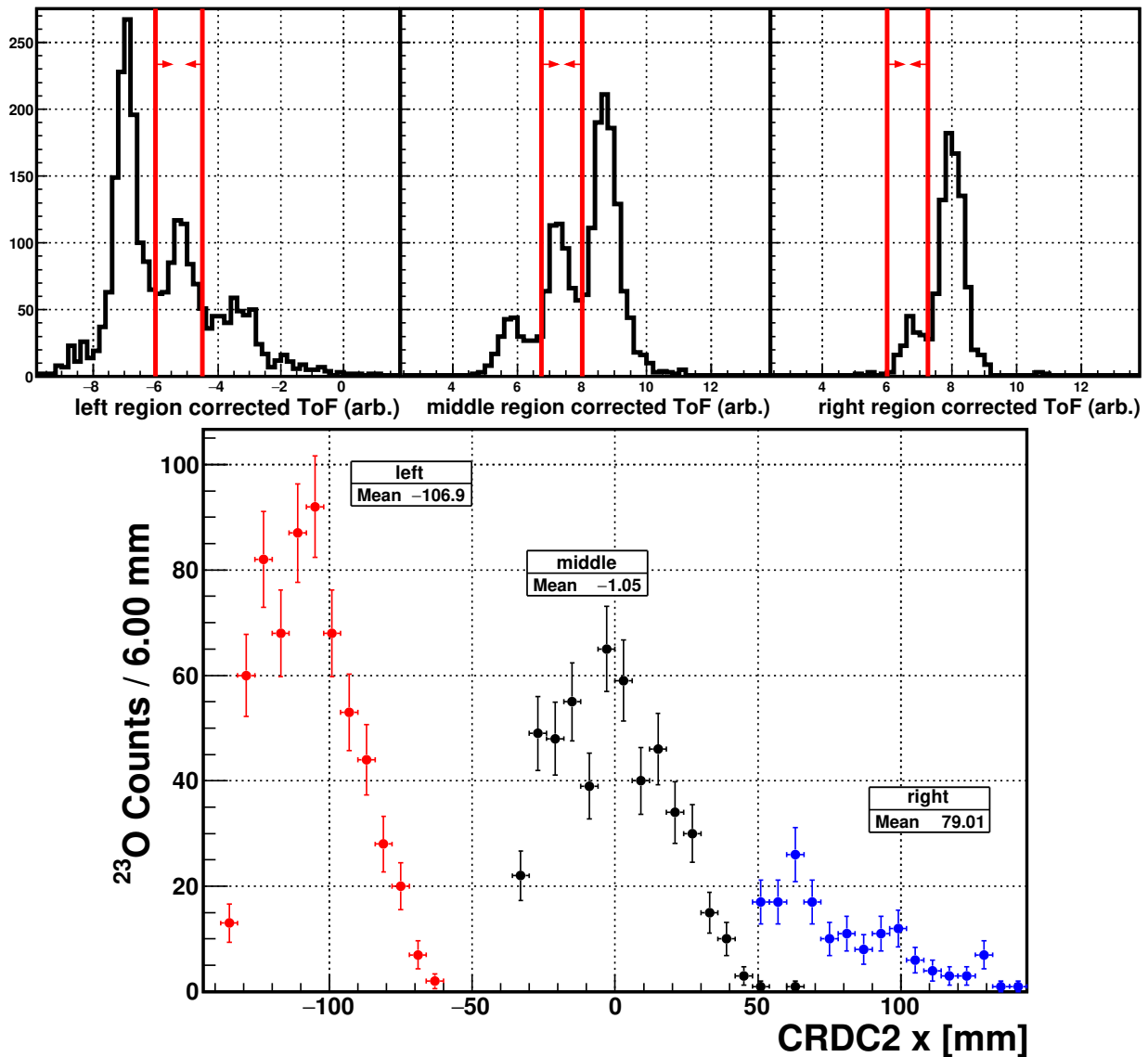


Figure 4.29: The top three panels plot the corrected ToFs for the three different regions. For each region a 1D gate is indicated by the red lines and arrows, and is applied to the CRDC 2 x distributions plotted in the bottom panel. The red, black, and blue points plot the CRDC2 x distributions for events under the left, middle, and right region gates respectively. The gates shown here select events with a slightly shorter flight time and CRDC2 x distributions that are shifted to the left compared to the gates shown in Figure 4.28.

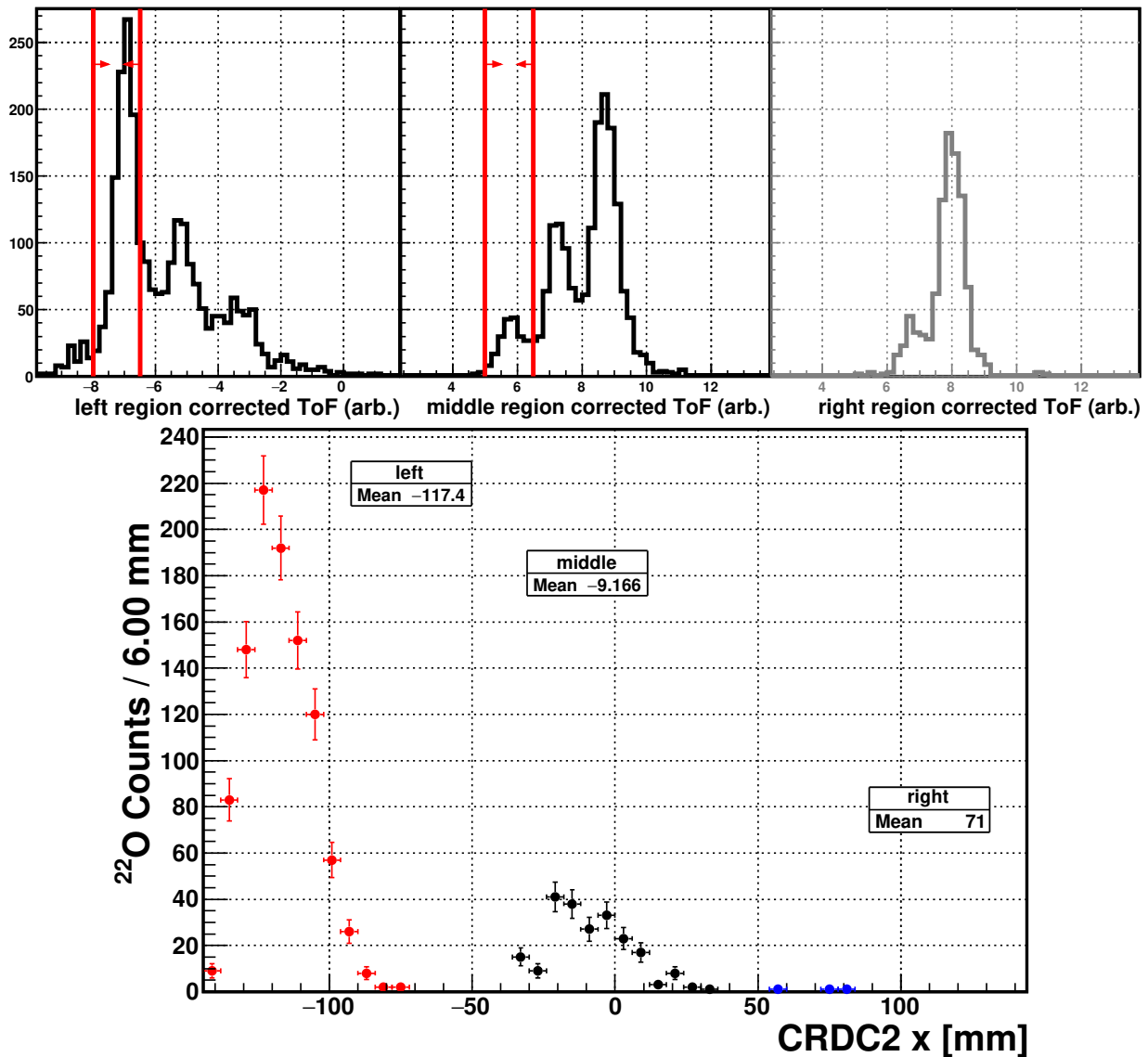


Figure 4.30: The top three panels plot the corrected ToFs for the three different regions. For each region a 1D gate is indicated by the red lines and arrows, and is applied to the CRDC 2 x distributions plotted in the bottom panel. The red, black, and blue points plot the CRDC2 x distributions for events under the left, middle, and blue region gates respectively. The gates applied to these plots select events with the shortest ToFs for oxygen reaction products. Note that the CRDC2 x distributions are shifted further to the left than the other two sets of gates.

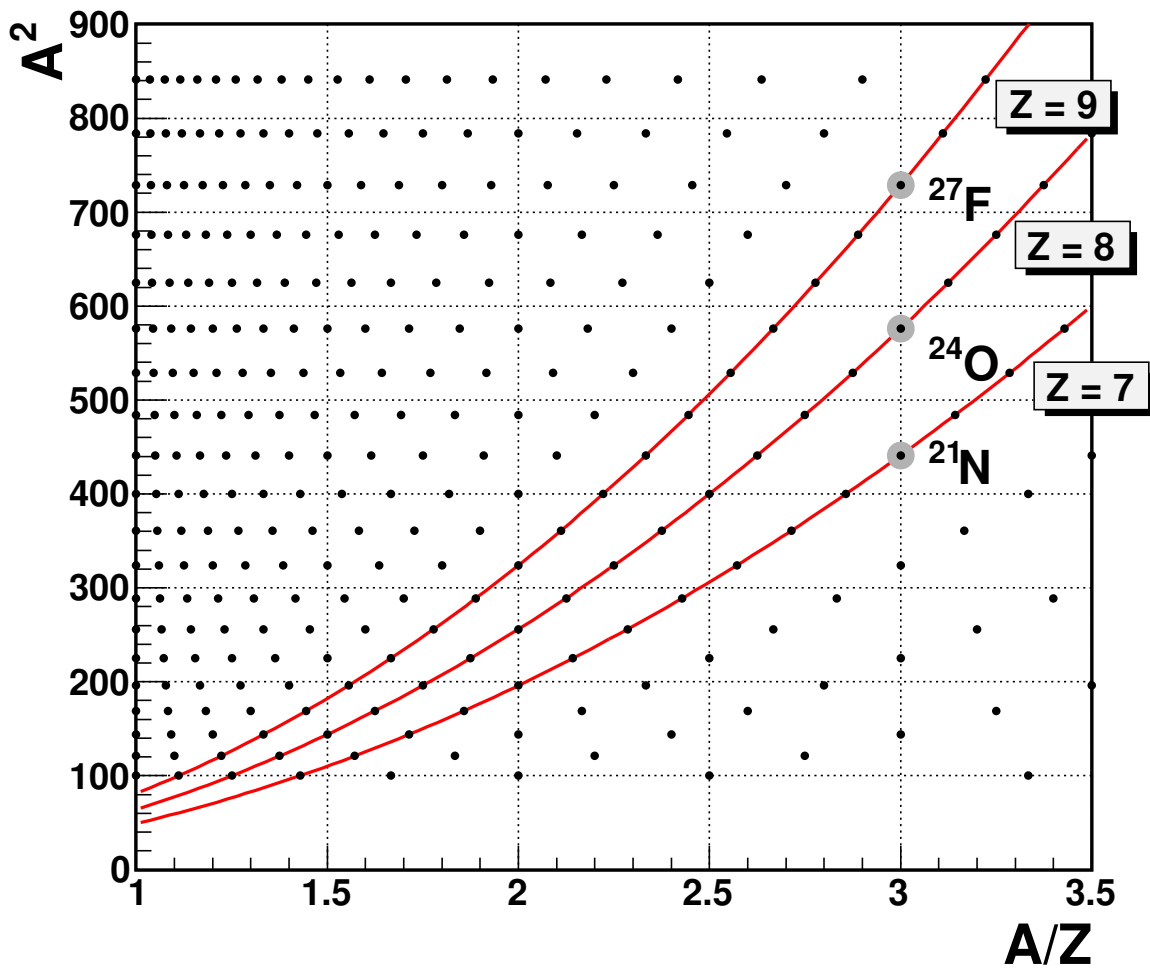


Figure 4.31: An illustration of A^2 versus A/Z for $10 \leq A \leq 30$ and $Z \leq A$. Each point is a separate nucleus (some unphysical). The red curves indicate curves of constant Z . Three nuclei with $A/Z = 3$ that are in the Sweeper acceptance are highlighted with gray circles.

4.2.4 Two-Neutron Selection

The four-momentum of both neutrons from a $2n$ decay must be measured in order to correctly calculate the three-body decay energy. The detector system does not distinguish between one neutron interacting twice and two neutrons interacting independently. Therefore, identifying events where MoNA/LISA recorded two interactions (also referred to as hits) in coincidence with an oxygen fragment does not guarantee that the two hits correspond to the two neutrons from the decay. When a neutron interacts with the scintillator material, it can transfer any amount of energy up to its total kinetic energy. Therefore, it is possible that the second hit results from a second

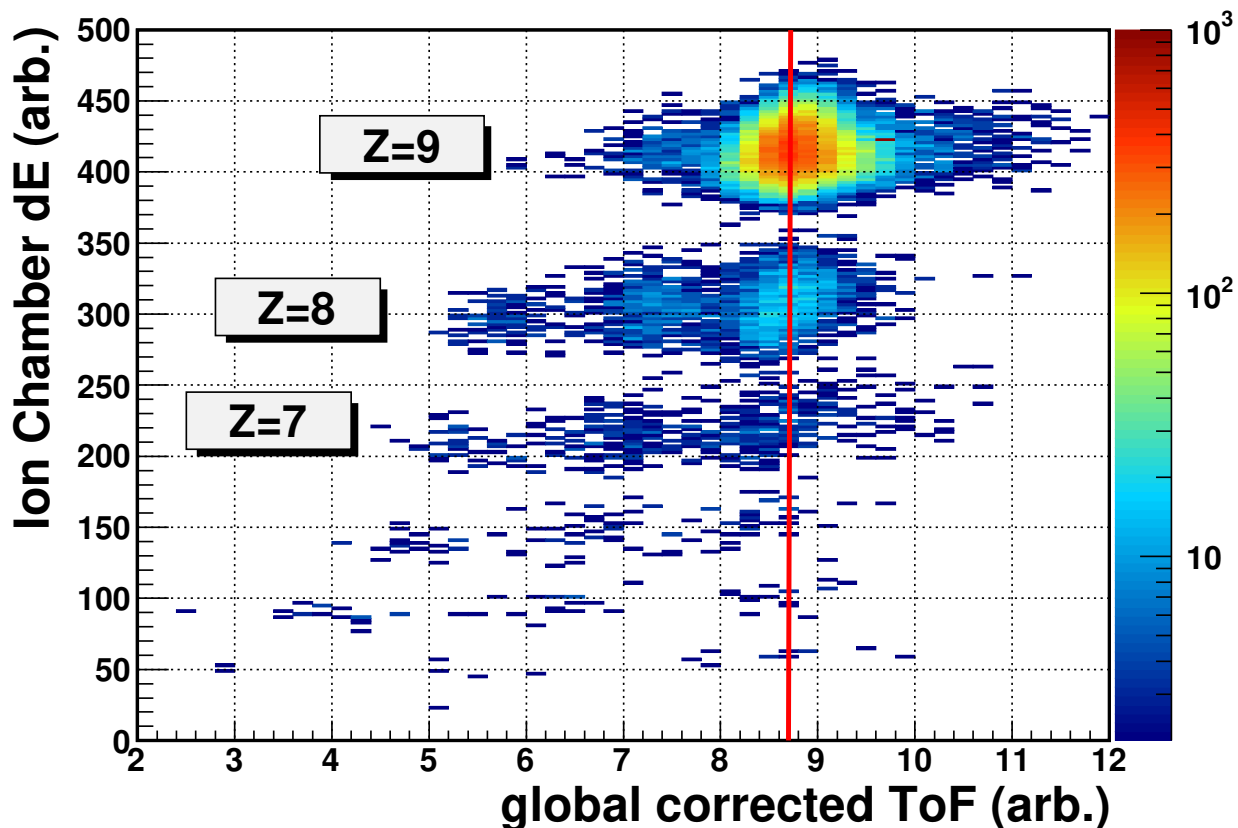


Figure 4.32: Ion chamber ΔE versus global corrected ToF for all events from the ^{27}F beam that fall inside one of the region gates shown in Figure 4.25. The red line corresponds to the $A/Z = 3$ line in Figure 4.31.

detection of a single neutron after it was scattered during its first interaction. For the purposes of this document, events where a single neutron is detected twice will be referred to as “one-neutron scattering” events and events where both neutrons are detected will be referred to as “true two-neutron” events.

4.2.4.1 Causality Cuts

Contributions from one-neutron scattering are reduced by applying “causality cuts.” These analysis cuts place restrictions on the spatial separation and the first-to-second hit speed which is defined as the distance between hits divided by the time between hits; see Figure 4.34. This technique has been used to enhance the two-neutron signal in previous measurements of three-body states (87; 88; 89; 46; 90; 91; 92; 93; 94). For this analysis the causality cuts were $d_{12} \geq 25$ cm and

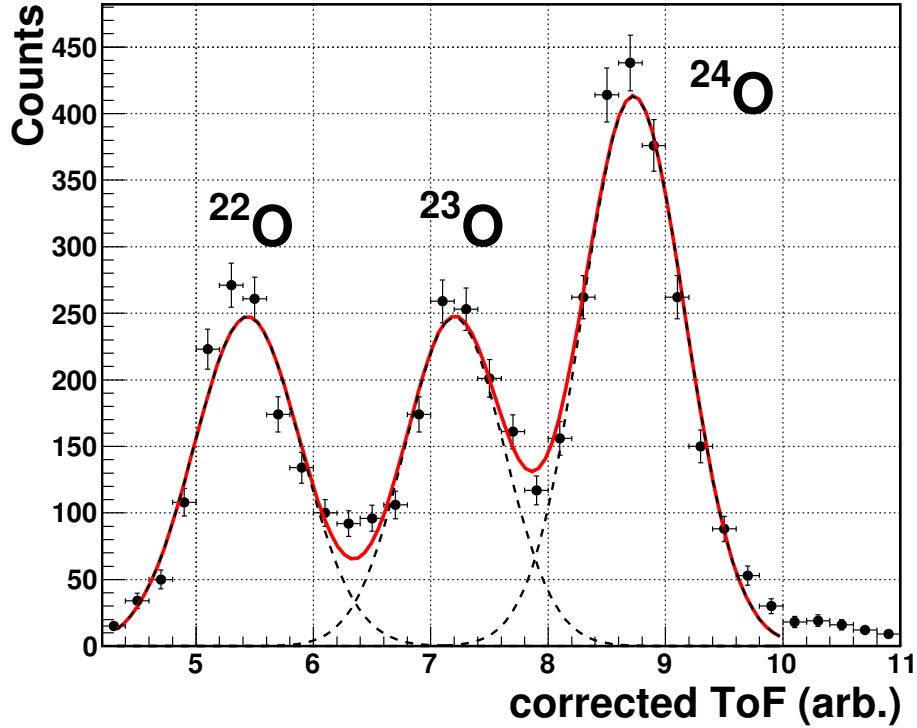


Figure 4.33: One dimensional particle identification for the oxygen reaction products. Events plotted here are required to fall inside the oxygen reaction product gate shown in Figure 4.24 and inside one of the “good” CRDC1 gates shown in Figure 4.25. In addition, coincidence with one of the MoNA/LISA bars is required.

$$7 \leq v_{12} \leq 30 \text{ cm/ns.}$$

4.2.4.2 Decision Forest

A machine learning approach was used as an alternative method for selecting true two-neutron events using the Toolkit for Multivariate Data Analysis (TMVA) (95) built into the ROOT Data Analysis Framework (96). This approach is described in Ref. (39) and a brief summary is provided in this section.

The TMVA toolkit supplies the computational implementation for a number of machine learning techniques of which the decision forest was found to be the most suitable for classifying events as either true two-neutron or one-neutron scattering events. A decision tree makes binary cuts on a number of different parameters in order to classify an event as signal or background. In this analysis, the parameters are the x , y , z , and t components of the first and second hit vectors as

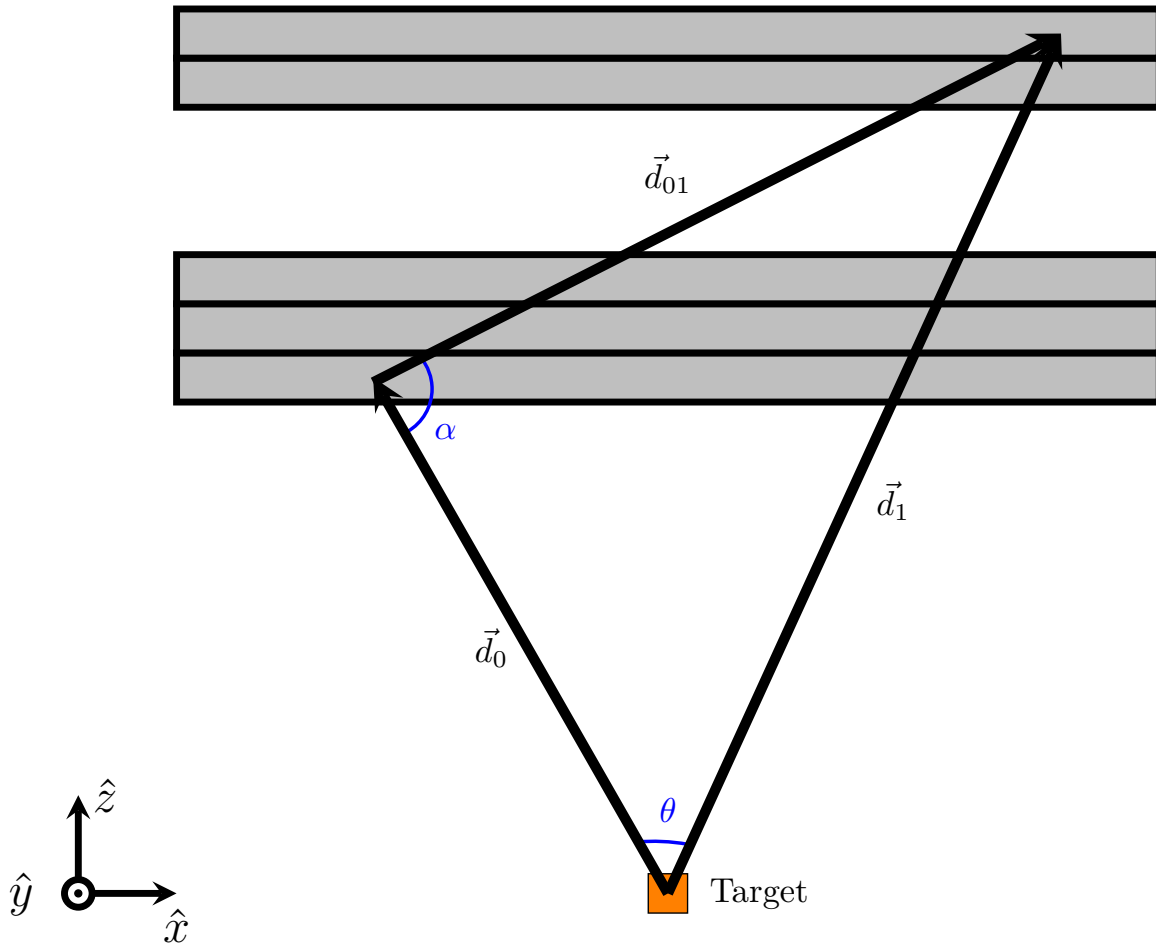


Figure 4.34: An illustration of the relevant position vectors calculated in a two-neutron event. The position vector \vec{d}_0 (\vec{d}_1) is from the target to the location of the first (second) interaction in MoNA/LISA; $\vec{d}_{01} = \vec{d}_1 - \vec{d}_0$.

well as the hit separation distance $|\vec{d}_{01}|$, relative speed $|\vec{d}_{01}|/(t_1 - t_0)$, opening (θ) and scattering (α) angles; see Figure 4.34.

A schematic view of a decision tree is shown in Figure 4.35. The process for training/building a decision tree may be summarized as iteratively dividing the labeled training data into subsets by finding the parameter and corresponding cut value that maximizes the separation between signal and background. At each node in Figure 4.35, the training data are divided into two groups based on which parameter x_i best distinguishes signal from background. The process stops once the training data subsets reach some minimum size ($\sim 5\%$ of the training sample size). The “leaf”

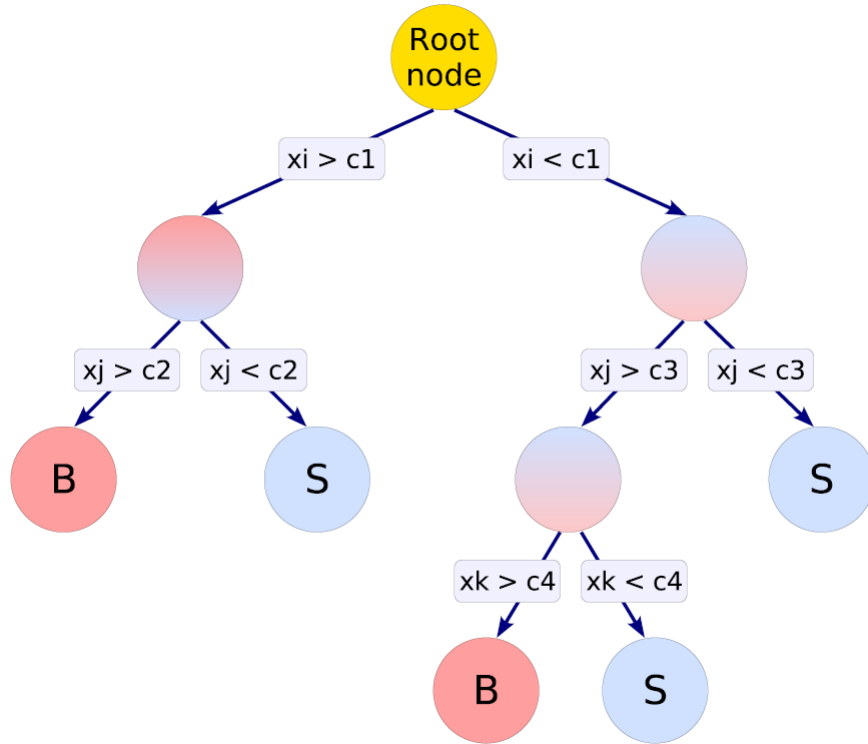


Figure 4.35: Schematic view of a decision tree. At each node a binary cut is made on one of the parameters $x_{i,j,k,\dots}$. Image source: (95).

nodes at the end of the training process are labeled “signal” or “background” depending on the class to which the majority of events in each “leaf” subset belong. This process essentially divides the parameter space into many regions that are classified based on the majority of labeled test events in the final leaf node. The separation criterion used in this analysis was defined by $p(1 - p)$ where $p = 0.5$ for an evenly mixed signal/background sample.

A single decision tree may be unstable with respect to statistical fluctuations in the training sample (95). To circumvent this instability, multiple trees are built and their classifications are averaged together to give a dimensionless value $-1 \leq x \leq 1$ for every event. A single cut based on this “classifier” variable is used to distinguish between true two-neutron and one-neutron scattering events. A value of 0.03 was chosen to optimize statistics and signal purity in terms of both the classifier and the causality cuts discussed in Section 4.2.4.1.

Once the decision forest is built and trained the experimental and simulated data sets are pro-

cessed through the classification algorithm to compute the classifier variable for every event. The top panel in Figure 4.36 shows the classifier output for a simulated data set that was not used for training and validation. In simulation the true two-neutron (signal) and one-neutron scattering (background) events are labeled so the efficacy of the classification can be assessed; the purity of the simulated true two-neutron signal above the cut (classifier = 0.03, the red line in Figure 4.36) is 90%.

Building the decision trees requires a training data set with more statistics than are available in the experimental data. Therefore, simulated data were used to train the decision tree. This method has the advantage that the training data are easily labeled. However, the crippling disadvantage is that this reduces the reliability of the decision tree since the construction of the tree is entirely based on the simulation. Any correlations that are present in the simulation, whether or not they reflect reality, will be incorporated into the classification routine. Training a decision tree on experimental data is not without its own drawbacks because there is no way to label true two-neutron and one-neutron scattering events with 100% certainty. The performance of the decision forest can be compared to that of the causality cuts. The bottom panel in Figure 4.36 shows the classifier output in terms of the signal/background determination made by the causality cuts. According to the causality cuts, the signal purity above the classifier cut is 80%.

The decision forest classification to identify two-neutron events results in slightly higher statistics while the causality cuts are a simple, easy-to-implement solution. Therefore, two versions of the ^{26}O half-life analysis were carried out; one used the decision forest the other used the causality cuts to select two-neutron events.

4.3 Fragment Reconstruction

Measurement of a two- or three-body decay energy requires that the four-momentum vector of the recoiling fragment be known at the decay vertex. Typically this is recovered from measurements of the fragment positions $(x, y)^{(D)}$ and angles $(\theta_x, \theta_y)^{(D)}$ after the Sweeper magnet (see (97; 78)). These measurements are fed into an ion-optical calculation that includes information

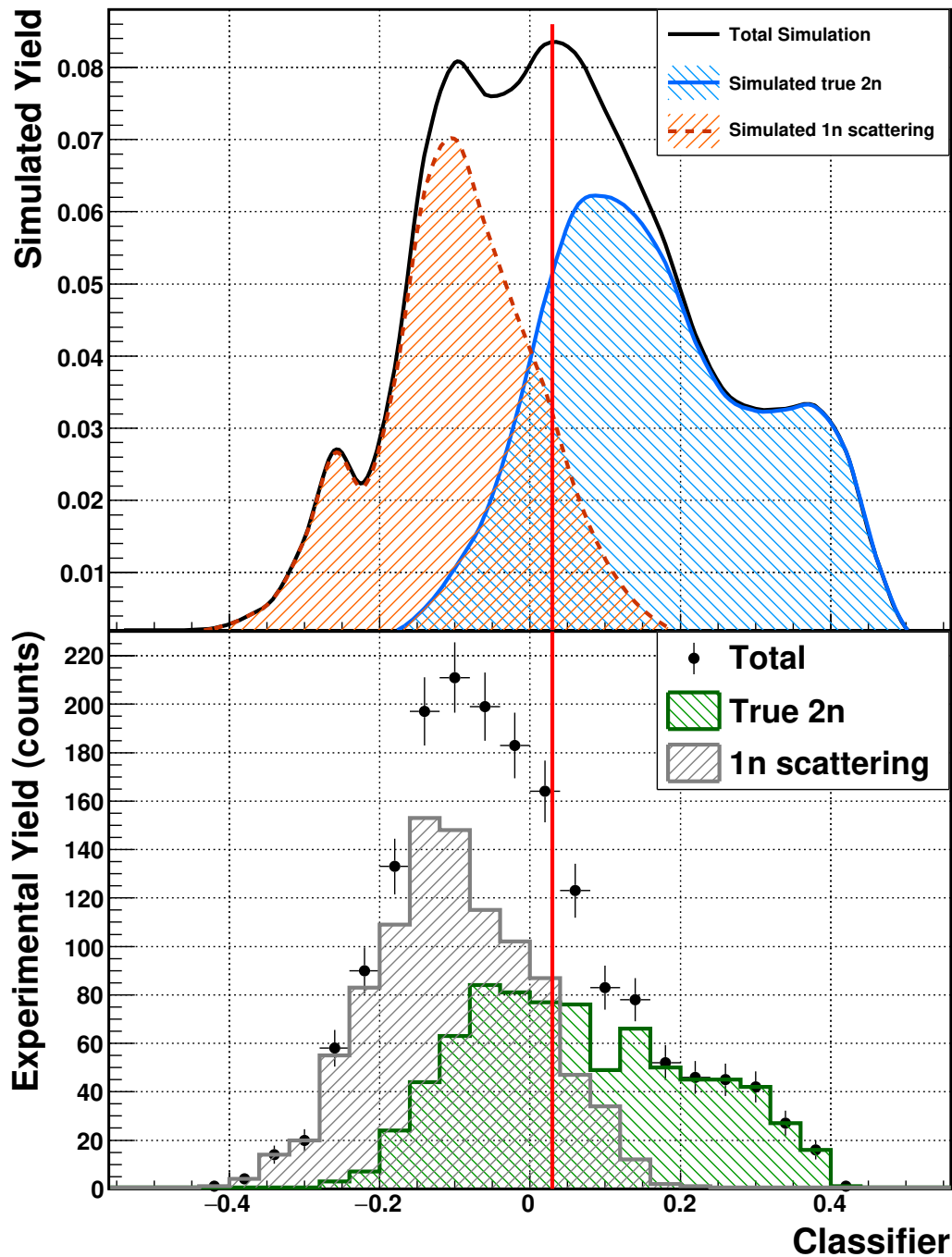


Figure 4.36: The classifier output is plotted to examine the reliability of the decision forest. In the top panel, the classifier output distributions for simulated, labeled true two-neutron (blue) and one-neutron scattering (orange) events are plotted. The black curve is the sum of the two distributions. In the bottom panel, the decision forest is compared to the causality cuts; the green histogram plots the classifier output for events that the causality cuts identify as true two-neutron events. The gray histogram shows the classifier output for events that the causality cuts identify as one-neutron scattering events. The red line indicates the final cut on the classifier output used in the analysis.

about the strength and shape of the magnetic field and outputs the angles $(\theta_x, \theta_y)^{(T)}$ and energy of the fragment at the exit of the target. This method of reconstruction was not viable for this experiment because the CRDC1 malfunction (Section 4.1.2.2) corrupted one of the position measurements needed to calculate the dispersive angle after the magnet $\theta_x^{(D)}$. Therefore, the fragment energy was determined using the measured time-of-flight between the target and thin scintillators:

$$\begin{aligned}\beta &= \frac{d}{t} \\ \gamma &= \frac{1}{\sqrt{1 - \beta^2}} \\ E &= \gamma m \\ P &= m\beta\gamma\end{aligned}\tag{4.4}$$

where $c = 1$, d is the path length that the fragment with rest mass m traverses in the measured time t ; β and γ are the velocity and Lorentz factors respectively and E and P are energy and momentum.

The path length between the two timing scintillators is not directly measured and varies event-by-event because the decay kinematics and position and angular spreads of the incoming beam result in slightly different trajectories through the magnet. To first order, a trajectory along an inner arc through the Sweeper and ending on the $-x$ side of CRDC2 will cover a shorter distance than a larger arc along the outer edge of the magnet and ending on the $+x$ side of CRDC2 (see coordinates defined in Figure 3.1). Therefore, the measured x position on CRDC2 can provide an estimate of the path length of the fragment trajectory.

In order to extract a correlation between CRDC2 x and path length, the calibrated time-of-flight (ToF) measured for unreacted ^{27}F beam fragments between the target and thin scintillators (see Section 4.1.2.4) was used along with the known beam velocity to estimate path length as a function of CRDC2 x . Data were recorded where the Sweeper magnetic field was adjusted to place the unreacted ^{27}F beam at different positions across the charged particle acceptance. The dispersive effect of the magnetic field introduces a correlation between momentum/velocity and x position for the unreacted beam; so selecting events near the center of the x distribution corresponds to selecting

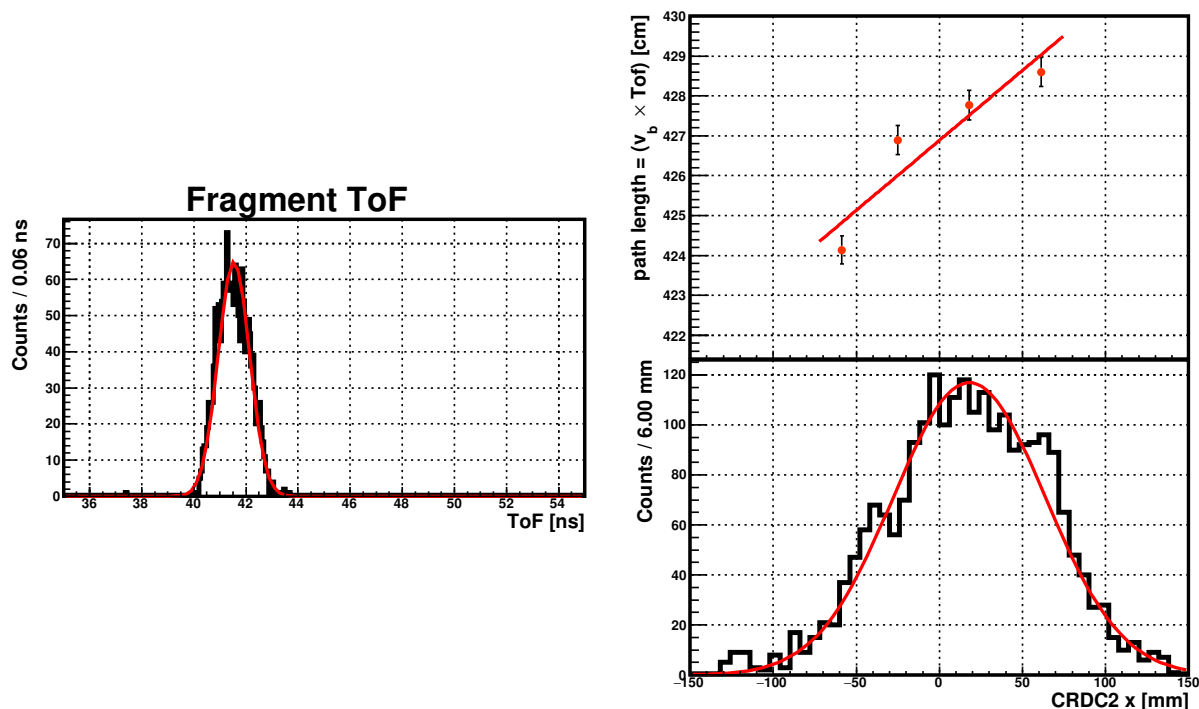


Figure 4.37: The correlation between path length as a function of CRDC2 x is plotted in the upper right panel. The abscissa for each point is the mean of a Gaussian fit to the CRDC2 x distribution. The ordinate of each point is the mean of a Gaussian fit to the calibrated ToF distribution multiplied by the velocity of ^{27}F after the segmented target; the error bars represent the fit error and the uncertainty in the velocity calculation introduced by the uncertainties in the silicon and beryllium thicknesses, $\pm 1 \mu\text{m}$ and $\pm 4 \mu\text{m}$ respectively. The left and bottom right panels are examples of the ToF and CRDC2 x spectra, respectively. Red curves plot the Gaussian fits.

events near the center of the momentum distribution. Since the central velocity/momentum of the ^{27}F entering the magnet is known and unchanged by adjustments to the Sweeper magnetic field, the distance to different x positions can be approximated by multiplying the velocity by the measured ToF. The upper right panel in Figure 4.37 plots the correlation between CRDC2 x and ^{27}F velocity \times ToF centroid; the other two panels show the CRDC2 x and ToF distributions for one of the data sets during which the current in the Sweeper magnet was set to 300 A. Data was taken with four different current settings: 290, 300, 310 and 320 A.

The correlation described above was extracted for the unreacted ^{27}F beam and subsequently used to estimate the path length event-by-event for oxygen reaction products. The velocity of oxygen reaction fragments was then calculated event-by-event by dividing the path length by the calibrated ToF between the target and thin scintillators; see Section 4.1.2.4. The energy and mo-

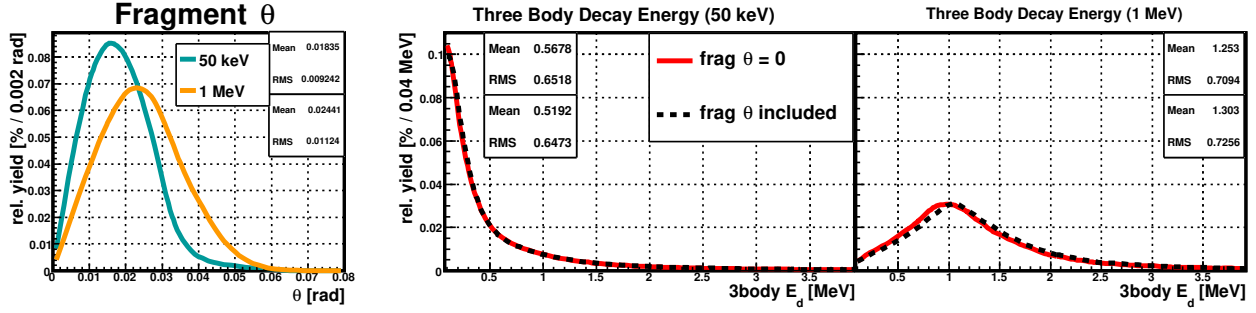


Figure 4.38: The left panel plots the simulated distribution of angles θ between the lab-frame fragment momentum vector and the beam axis. The middle and right panels plot the three-body decay energies reconstructed from the simulated detector responses where the decay energy available for every simulated event was 50 keV (middle) and 1 MeV (right). The red curves plot the decay energies calculated with the fragment angle $\theta = 0$ and the black curves include the angle information.

momentum magnitude for the fragments was calculated according to eq. 4.4. The momentum vectors for every fragment were assumed to be aligned with the beam axis. Three-body decay energies reconstructed under this assumption will, on average, be lower than if the fragment angle is included. However, through simulation, this shift was found to be $\sim 1.5\%$ for 50 keV decay energies and $\sim 3.8\%$ for 1 MeV decay energies; see Figure 4.38.

Finally, the kinetic energy of the fragment at the decay vertex is approximated by adding back an estimate for the energy lost by the fragment as it traveled from the decay vertex to the edge of the target. After identifying the beryllium segment in which the reaction and decay took place, see Section 4.1.1.2, an estimate for the energy addback is selected event-by-event, see Table 4.7. The addback estimate for reaction fragments produced in a beryllium segment is determined by the energy loss calculated for an ^{24}O fragment produced in the middle of the beryllium segment plus the energy loss through all subsequent segments. There are seven total segments in the segmented target, indexing them from zero to six implies that the beryllium targets have indices $i = 1, 3, 5$, so the addback estimate for these segments is

$$dE_i^{\text{addback}} = dE(0.5t_i) + \sum_{j=i+1}^6 dE(t_j)$$

where t_i, t_j are the thicknesses for the $i^{\text{th}}, j^{\text{th}}$ segmented given in Table 3.1. For example, the Be

2 addback is calculated as the energy loss through 1868 μm of beryllium, 138 μm of silicon, 3302 μm of beryllium, and 142 μm of silicon.

Target	Energy Addback [MeV]
Be 1	785.0
Be 2	488.7
Be 3	177.6

Table 4.7: Energy addback used to reconstruct the energy of the ^{24}O fragments produced from ^{27}F in one of the ^9Be targets.

4.4 Modeling and Simulation

The ^{26}O half-life was extracted by comparing the measured relative speed distribution to simulated ones that were generated using different values for the half-life. A Monte Carlo simulation was used to produce simulated data sets that are convoluted with the experimental resolution, acceptance and efficiency and take into account the beam profile, reaction and decay processes, energy losses in the segmented target, and the half-life of the neutron-unbound state.

In general, the simulation consists of two parts that (1) model the incoming beam and the dynamics of the reaction and subsequent neutron decay as well as the energy loss in the target material and transportation of the charged fragments through the magnet and (2) model the neutron interactions with the MoNA/LISA detectors using GEANT4 (98; 99; 100). For each simulated event, a beam trajectory is described by randomly generated $(x, \theta_x, y, \theta_y)$ based on a set of user-defined Gaussian distributions. The beam energy is randomly selected from a uniform distribution corresponding to the momentum acceptance of the A1900 fragment separator in the experiment. Then a random point inside the reaction target is selected as the location for the nucleon removal. Next, an energy loss is determined by the kinetic energy of the particle and the amount of material upstream from the reaction point. This energy loss is subtracted from the starting energy to set the particle's kinetic energy at the reaction point. Next, the knockout reaction is simulated (see Section 4.4.3); this is a one-proton removal for the case of ^{26}O . If the half-life, $T_{1/2}$, is set to be nonzero, a random value for the survival time, t_s , of the unbound system is drawn from an

exponential distribution characterized by $T_{1/2}$. Then the unbound nucleus is propagated a distance d to the decay point determined by its speed and t_s ; the propagation incorporates the energy loss based on the nucleus (A, Z) and the material. The neutron decay is simulated and the kinetic energy of the daughter fragment and the distance between the decay point and the edge of the target determines an energy loss value that is subtracted from the kinetic energy of the daughter fragment to set the kinetic energy after the target. If $T_{1/2} = 0$ ps, the neutron decay occurs immediately after the nucleon removal reaction (i.e. the reaction and decay points are the same). Finally, the energy loss through the remainder of the segmented target is determined to set the fragment energy and momentum going into the Sweeper magnet. An ion-optical matrix is used to calculate the fragment $(x, \theta_x, y, \theta_y)$ after the magnetic field. This transformation determines the (x, y) positions at the CRDCs. The (x, y) positions are then folded with the detector resolutions which are simulated by adding a random number drawn from a Gaussian distribution with mean $\mu = 0$ mm and $\sigma = 3$ mm.

The four-momentum vectors of the neutrons are passed to GEANT4 where interactions with MoNA and LISA are modelled. The MENATE_R database (101; 102) supplies cross-sections for neutron-carbon and neutron-hydrogen interactions. When treating a multi-neutron decay, GEANT4 generates separate lists of interaction location, time and light output for each neutron. Before comparing to data, these lists are re-ordered to produce a single list sorted by interaction time.

The charged particle and neutron simulation outputs are combined into a single ROOT file then processed with the same analysis code used to make spectra from the data. The simulation is designed such that a single reaction/decay channel in one of the beryllium targets is simulated at a time. Therefore, three simulations, one for each target, are run for each reaction/decay channel then combined before comparing to data. Analysis cuts on the experimental data are used to extract sets of events with a certain combination of beam and reaction fragments (e.g. ^{27}F and ^{24}O or unreacted ^{27}F). The relevant simulations can then be run and compared to the experimental data set.

4.4.1 Incoming Beam Parameters

The incoming beam profile was determined by comparing the (x, y) distributions from the first silicon detector and CRDC2 to the corresponding distributions from the unreacted ^{27}F experimental data set. The beam energy and uniform energy spread just upstream from the segmented target were determined to be 105.3 MeV/u and 2.75 MeV/u, respectively, by the settings of the A1900 fragment separator and the thickness of the target scintillator. The (x, y) distributions measured by the first silicon detector (Si 0) determined the shape of the beam spot and the (θ_x, θ_y) parameters were tuned to match the simulated CRDC2 (x, y) distributions to the experimental data, see Figure 4.39.

The discrepancy between data and simulation for the CRDC 2 y distribution (lower right panel in Figure 4.39) exists because the simulated beam enters the magnetic field offset from $y = 0$ due to the constraint that the simulation reproduce the y position distribution measured on the first silicon detector. The mismatch between simulated and measured CRDC 2 y distributions in Figure 4.39 implies that the offset used in the rough calibration of the silicon y position is incorrect. This offset can be reduced to bring the simulated and measured CRDC 2 y distributions into agreement. However, the CRDC 2 y measurement is not used in calculating any physics quantities (e.g. decay energy or relative speed) so it has no impact on the analysis, therefore an exact match between data and simulation for this observable is not critical.

4.4.2 Energy Loss in Silicon Detectors

The unreacted ^{27}F data set was also used to validate the simulation of ion energy losses in the silicon detectors. The silicon energy loss measurements in this data set were made on ^{27}F ions coming from a beam with a well-known energy profile 105.3 ± 2.75 MeV/u impinging on segments of silicon and beryllium with thicknesses (measurement uncertainty $< 1\%$), so the energy deposited by the ions can be easily modeled. The stopping power tables from the SRIM software package (103; 104) determine the energy loss per unit length dE/dx for ions with mass A and charge Z traveling in a specific material, in this case either silicon or beryllium. The dE/dx is multiplied by

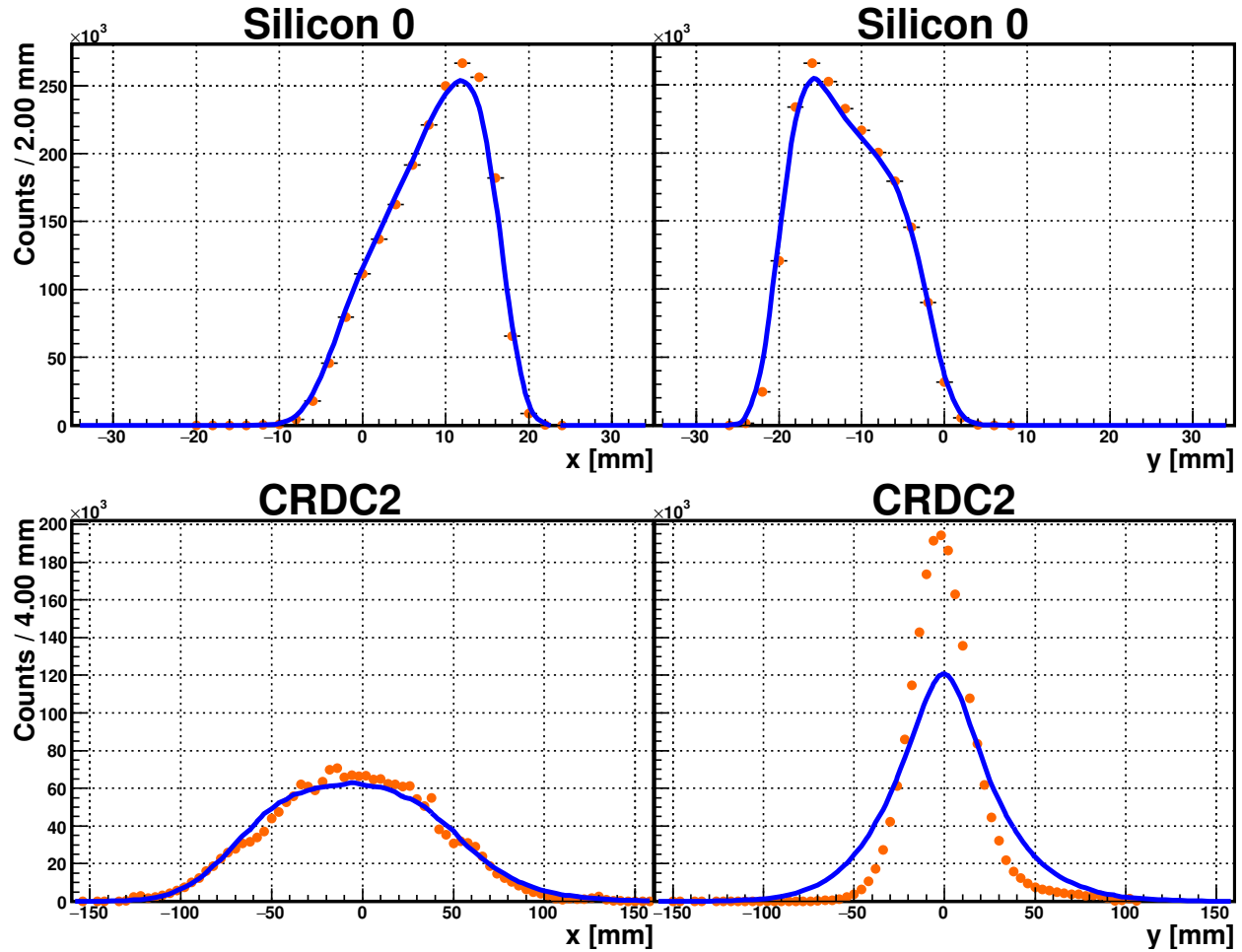


Figure 4.39: The $(x, y, \theta_x, \theta_y)$ profile for the simulated beam was set through comparisons to the experimental distributions plotted from the unreacted ^{27}F data set. The first silicon x, y position distributions are shown in the top row and the CRDC2 x, y distribution are plotted in the bottom row. Orange points are data and blue lines are simulation.

the thickness of the material to give the energy deposited by the ion. The resolution of the energy loss measurement is reproduced using a Gaussian distribution with $\sigma = 0.9$ MeV. Figure 4.40 compares the energy loss measured with the silicon detectors to the simulated energy loss.

4.4.3 Reaction Parameters

The $1p$ -knockout reaction was simulated by removing nucleons from the beam fragment and imparting a momentum kick to the resulting system. The component of the momentum kick parallel to the beam axis was parameterized according to the Goldhaber model (105). The component of

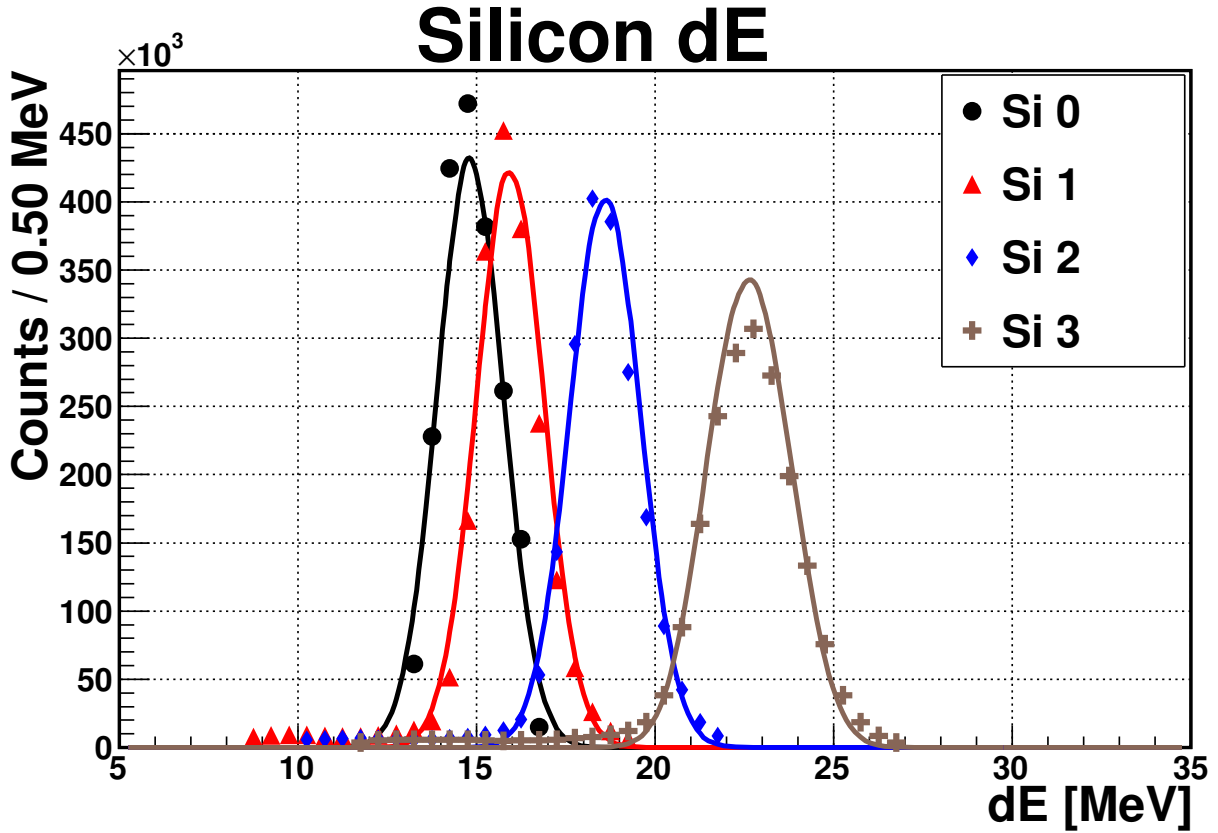


Figure 4.40: Energy loss of ^{27}F beam fragments measured in the four silicon detectors is plotted by the black dots, red triangles, blue diamonds, and brown crosses; solid curves plot the simulation output. The resolution of the silicon detectors is simulated using a Gaussian with $\sigma = 0.9$ MeV.

the kick transverse to the beam axis was parameterized according to the model described in (106). Both models describe the parallel and transverse momenta distributions as Gaussians defined by widths $\sigma_{\parallel} = 120$ MeV/c and $\sigma_{\perp} = 92$ MeV/c respectively. These widths were fixed through comparing the simulated and experimental CRDC2 x position distributions.

4.4.4 Additional parameters

The area densities of the silicon detectors were specified by the manufacturer, and the area densities of the beryllium targets were determined from their mechanically measured thicknesses. Table 3.1 summarizes the thicknesses of each component in the segmented target. The matrices for the ion-optics calculations are generated based on measurements of the Sweeper magnetic field. A library of field measurements was produced in previous work (78) and a Hall probe inserted in the field

during the experiment determined the field strength and thus which set of measurements (along with the mass and charge of the fragment to be analyzed) to use for producing the ion-optical matrices. The geometric acceptances of the detectors were based on the measured physical sizes of the devices. Resolutions for MoNA/LISA included Gaussian resolutions for time ($\sigma = 0.18$ ns) and position ($\sigma = 3$ cm) measurements along the bar (82). The length of the bars as well as their discretization in the y and z directions were also incorporated into the simulation.

4.4.5 Cuts

The graphical cuts shown in Figure 4.25 were necessary for a reliable particle identification (e.g. Figure 4.33). These same cuts were applied to the simulation output in order to replicate any biases introduced by accepting different regions of the reaction fragment momentum distributions in a non-uniform manner. The resulting measured and simulated CRDC2 x distributions are plotted in upper left panel of Figure 4.41.

Cuts on the (x, y) positions of the charged fragments are made to ensure the detector acceptances are reproduced. The simulated neutrons are required to have physical flight times, and the same two-neutron cuts used on the experimental data (Section 4.2.4) are also applied to the simulation output.

4.4.6 Decay Model

The relative speed $v_{\text{rel}} \equiv |\vec{v}_n| - |\vec{v}_f|$ is the observable of interest for this experiment, and this quantity is influenced by the amount of energy available in the decay. A larger decay energy will produce a broader distribution of v_{rel} while a lower decay energy will produce a narrower distribution. Furthermore, since fits to the decay energy spectrum will not be used to extract any information about ^{26}O , a simplified decay model was used to reproduce the experimental spectra.

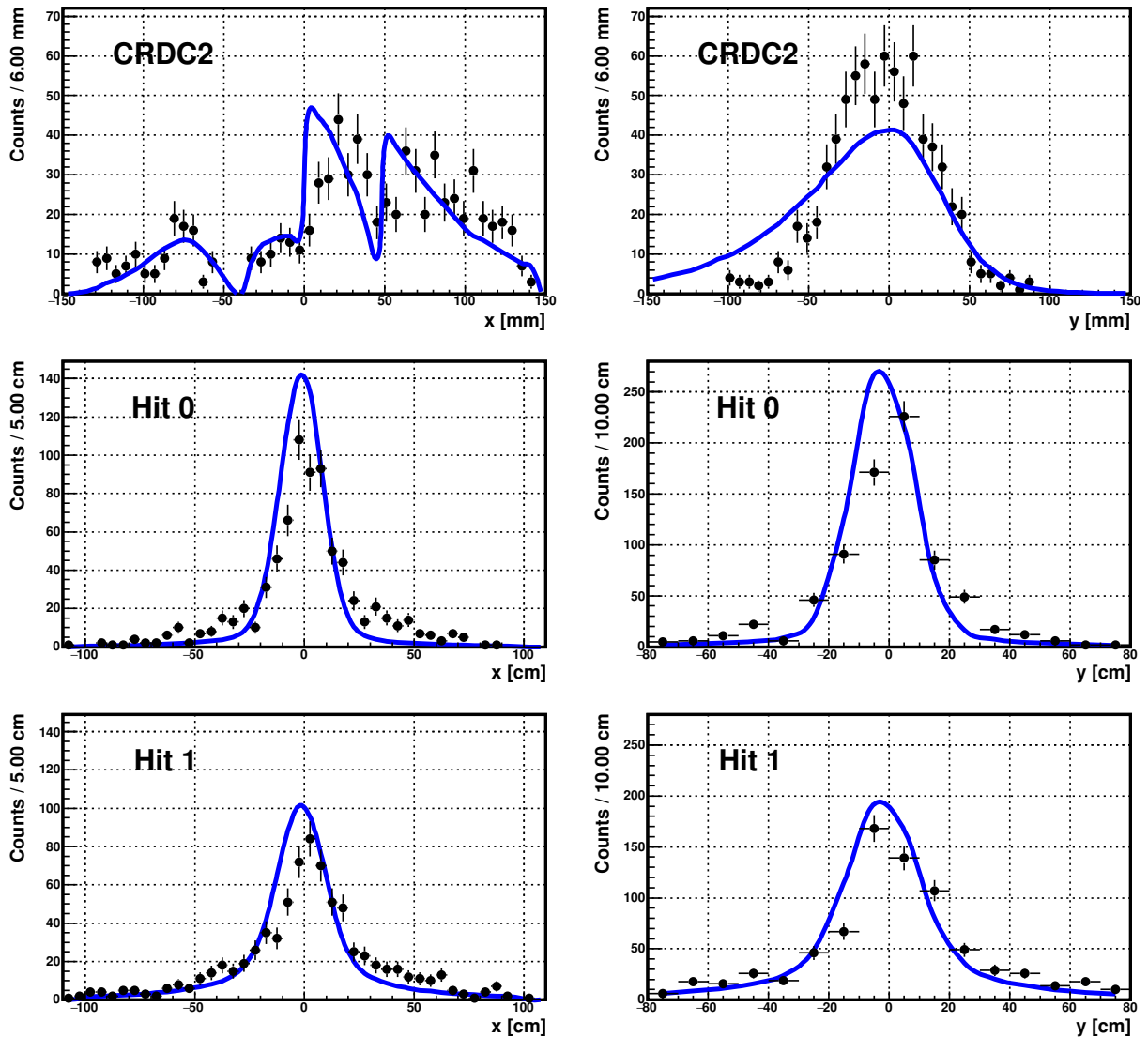


Figure 4.41: Fragment and neutron position spectra for ^{24}O events in coincidence with two hits in MoNA/LISA. Simulated position spectra (blue curves) are overlaid on the corresponding experimental spectra (black points). The top left and right panels plot the CRDC2 x and y spectra respectively. The middle left and right panels show the x and y distributions for the first time-sorted hit in MoNA/LISA. The bottom left and right panels show the x and y distributions for the second hit in MoNA/LISA.

4.4.6.1 One neutron decays

The decay energy for the single neutron emission $^{23}\text{O}^* \rightarrow ^{22}\text{O} + n$ was modeled as a δ -function at $E_{\text{decay}} = 50$ keV based on previous measurements of this decay (107; 108; 109). This means that for every simulated event, the amount of energy shared between the ^{22}O daughter fragment and the neutron was 50 keV. This energy was partitioned between the two particles according to eq. 2.4. The center-of-mass momentum vectors are equal and opposite. The orientation of the decay axis, which is collinear with the momentum vectors, is randomly chosen so that the decay is isotropic in the center of mass frame. Finally, the neutron and fragment momenta are boosted into the lab frame.

4.4.6.2 Two neutron decays

Two ^{26}O decay channels were simulated in this work. First, the decay of the ^{26}O ground state was modeled as a simultaneous emission of two uncorrelated neutrons where the decay energy distribution was a δ -function at 50 keV. For the purposes of this work, this process will be referred to as a phase-space decay and it uniformly samples the invariant mass of the fragment-neutron and neutron-neutron pairs using the TGenPhaseSpace class as it's implemented in ROOT (110). Second, the decay of the ^{26}O 1.28 MeV first excited state was modeled as a two neutron sequential decay through the 750 keV state in ^{25}O . The allowed decay energies for the one-neutron emission $^{26}\text{O}^* \rightarrow ^{25}\text{O} + n$ were uniformly distributed between 600 and 800 keV and the decay energies for the second one-neutron emission $^{25}\text{O} \rightarrow ^{24}\text{O} + n$ were uniformly distributed between 50 and 450 keV. This model for the ^{26}O and ^{25}O level structure is clearly unphysical but it serves to fold any background processes (such as the sequential decay of the 1.28 MeV ^{26}O excited state) into a single simulation.

4.5 Extracting $T_{1/2}$

After events corresponding to the $^{27}\text{F}(-1p) \rightarrow ^{26}\text{O} \rightarrow ^{24}\text{O} + 2n$ process were extracted from the experimental data set, the relative speed v_{rel} was calculated for each of these events

and the resulting distribution was compared to simulation using an unbinned maximum likelihood technique. This section describes the reason for using this technique and then the procedure by which it was implemented.

The survival time of each ^{26}O nucleus is not directly measured, so the half-life cannot be extracted by fitting an exponential function to a distribution of measured times. Instead the effect of a ~ 1 ps half-life on the neutron-fragment relative speed provides an indirect measurement of the half-life (see Section 3.10). The problem of extracting a value for the half-life, $T_{1/2}$, becomes one of parameter estimation where the true distribution of relative speeds is distorted not only by detector acceptances and resolutions but also by the kinematics of the decay process. The underlying probability density function (p.d.f.) can be thought of as the relative speed distribution produced by modeling the incoming beam, the $1p$ removal reaction, the $^{26}\text{O} \rightarrow ^{24}\text{O} + 2n$ decay and the detector responses. Model parameters, except for the half-life of the decay, are constrained by the experimental setup. The decay half-life is determined by finding the value $\hat{T}_{1/2}$ that maximizes the log-likelihood, $\ln L(T_{1/2})$, or equivalently, minimizes the negative log-likelihood. The latter sign convention will be adopted for the remainder of this document.

The p.d.f. from the previous paragraph cannot be described by an analytic function so the log-likelihood was constructed from a Monte Carlo simulation following the prescription described in Ref. (111). The procedure is outlined as follows:

1. Generate a simulated data set with a specified value for the half-life (e.g. $T_{1/2} = 1.5$ ps)
2. Specify a narrow range $\pm r$ in relative speed around each value s_i from the experimental data set
3. Calculate the total number of simulated events that fall within the range $s_i \pm r$ for each s_i
4. Divide the sum from step 3 by the total size of the range, $2r$, and the total number of simulated events for normalization

5. Take the natural logarithm of the quotient from step 4 and sum over all experimental data points s_i

This procedure can be summarized by the following equation

$$\ln L = \sum_i \ln \left[\frac{\sum_j \mathbf{1} \text{ if } (\tilde{s}_j \in (s_i \pm r))}{2rN} \right]$$

where \tilde{s}_j are the simulated relative speeds and N is the total number of events in the simulation.

The procedure outlined above can introduce systematic errors from two sources: (1) nonlinearity in the simulated relative speed distribution over the small range and (2) statistical fluctuations due to the number of events generated in the Monte Carlo simulation. In order to determine an appropriate range, the negative loglikelihood was calculated for two simulated data sets with known half-lives ($T_{1/2} = 2, 4$ ps). These pseudo data sets consisted of 100 simulated events in order to reproduce the statistics of the experimental data set. The negative LnL curves extracted from the pseudo data sets are plotted in Figure 4.42. For each data set, four range values were used to carry out the LnL calculation: $r = 0.005$ cm/ns, 0.050 cm/ns, 0.100 cm/ns and 0.500 cm/ns. When the range value is too large ($r = 0.5$ cm/ns, gray crosses), sensitivity to the half-life is reduced. When the value for r is too small ($r = 0.005$ cm/ns, black dots), the sum in Step 3 becomes sensitive to statistical fluctuations in the number of simulated data points. In principle, the range could be made vanishingly small in the limit of an infinitely large number of simulated events, however, this would not change the extracted half-life or the statistical uncertainty. Therefore, a value of $r = 0.100$ cm/ns was chosen since it resulted in extracting the expected $T_{1/2}$ for both pseudo data sets while utilizing a reasonable simulated data set size. Each point in the negative LnL curves corresponds to a simulated data set containing six million events.

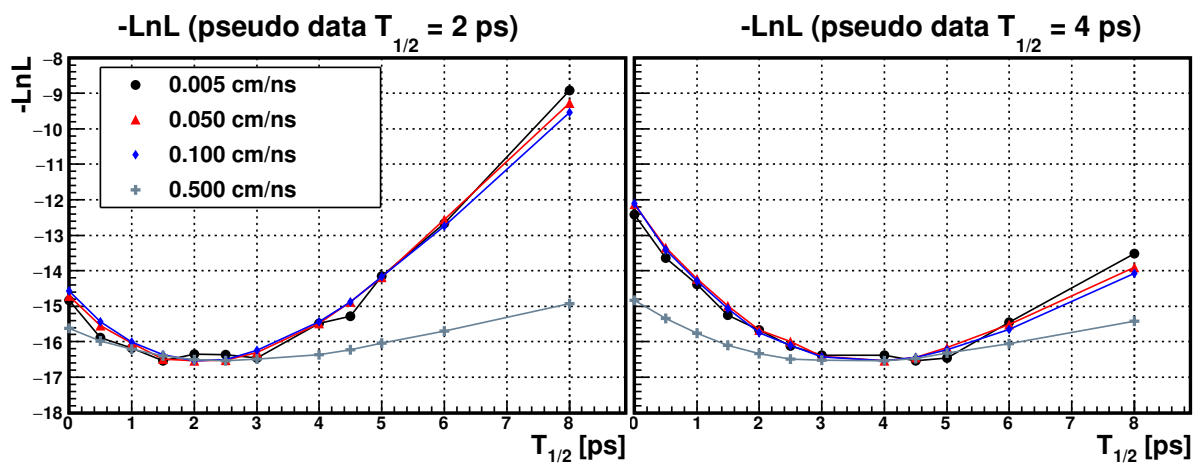


Figure 4.42: Negative LnL curves extracted from a pseudo data set with $T_{1/2} = 2$ ps (left) and a second pseudo data set with $T_{1/2} = 4$ ps (right). In both panels, range values of 0.005 cm/ns, 0.050 cm/ns, 0.100 cm/ns, and 0.500 cm/ns correspond to the black dots, red triangles, blue diamonds, and gray crosses respectively.

CHAPTER 5

RESULTS AND DISCUSSION

In this chapter, the results of the lifetime measurement are presented followed by a discussion about the performance of the segmented target. The performance is evaluated through comparing two versions of the analysis: (1) where the addback for the fragment kinetic energy is estimated assuming a single thick beryllium target and (2) where the procedure discussed in Section 4.1.1.2 is used to make an event-by-event identification of the beryllium segment in which the ^{26}O was produced.

5.1 Half-life Measurement

The signature of a measurable ($T_{1/2} \sim 1$ ps) half-life is a shift in the relative speed distribution. Details of this technique are presented in Section 3.10. To briefly summarize, if the decay of ^{26}O does not occur instantaneously, then the nucleus will slow down as it travels through the target material. As a result, the neutrons are emitted with a slower speed than if the decay happens instantaneously. This shifts the centroid of the relative speed distribution below zero.

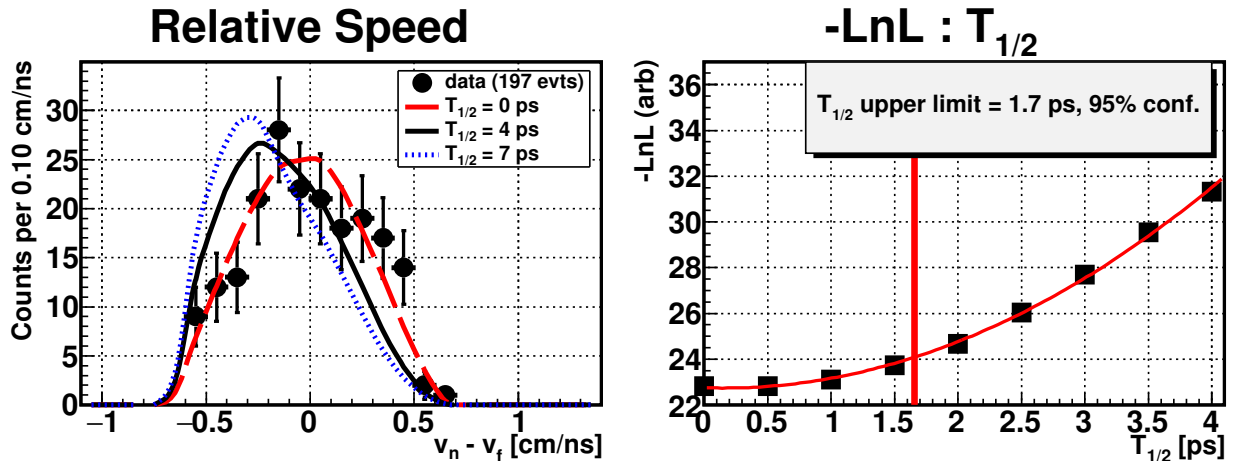


Figure 5.1: Half-life extracted from $^{23}\text{O}^* \rightarrow ^{22}\text{O} + n$ data. The left panel shows the relative speed distribution for data (black points) and three simulations with $T_{1/2} = 0$ ps, 4 ps, 7 ps. The right panel shows the negative loglikelihood as a function of half-life. The red line indicates the upper limit of 1.7 ps corresponding to a 95% confidence level.

5.1.1 Results

For consistency with the previous analysis (1) an unbinned maximum likelihood (LnL) technique (111) was used to extract the statistical uncertainties, see Section 4.5. The systematic uncertainty was determined by examining the decay of the ^{23}O first unbound excited state: $^{23}\text{O}^* \rightarrow ^{22}\text{O}+n$, reported in Ref. (107). In the current experiment, this decay was measured at the same time and with an identical setup to the ^{26}O measurement: segmented target, magnet setting, MoNA configuration, Sweeper detector settings and calibrations. Since the $^{23}\text{O}^*$ decay has a half-life $T_{1/2} \lesssim 10^{-20}$ s, it provides a means to quantify the systematic uncertainty associated with extracting a lifetime from a shift in the relative speed distribution. The distribution of relative speeds between ^{22}O fragments and the first neutron detected in MoNA/LISA is plotted in the left panel of Figure 5.1. In addition to the required fragment-neutron coincidence, the light deposited is required to be greater than 1 MeVee and the two-body decay energy is restricted to be less than 300 keV in order to suppress background events. The upper limit on the $^{23}\text{O}^*$ half-life was found to be 1.7 ps with a 95% confidence level, see Figure 5.1. This value represents the systematic uncertainty associated with extracting a half-life from the relative speed distribution measured with the experimental setup described in Chapter 3.

Turning to the ^{26}O half-life measurement, the relative speeds for ^{24}O fragments and first neutron hits are plotted in the left panels of Figure 5.2. The top left panel shows the distribution of relative speeds between ^{24}O and the first neutron hit for events where MoNA/LISA registered at least two hits, both of which deposit at least 1 MeVee of light. The three-body decay energy is required to be less than 300 keV in order to suppress background events. Causality cuts, see Section 4.2.4.1, were applied to suppress events where the two hits resulted from two separate detections of the same neutron. The spatial separation between two hits was required to be greater than 25 cm and the velocity difference, $|\vec{v}_{01}| = |\vec{v}_1 - \vec{v}_0|$ was required to be between 7 cm/ns and 30 cm/ns. In the bottom left panel, the relative speed distribution is plotted but the three-body decay energy gate is relaxed to 350 keV and the decision forest classifier is used to select true $2n$ events, see Section 4.2.4.2, instead of the causality cuts. The right panels in Figure 5.2 plot the negative

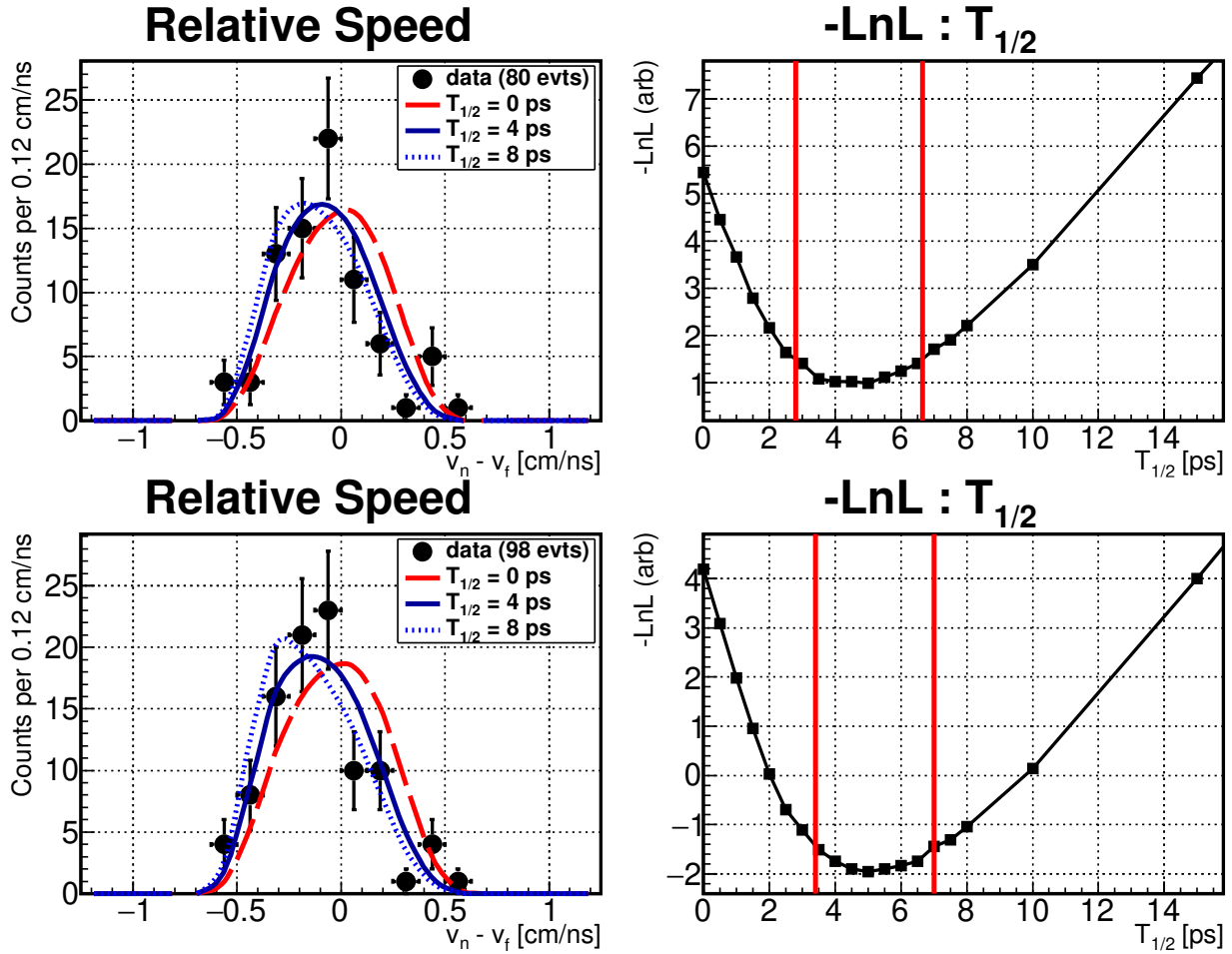


Figure 5.2: The relative speed distributions and LnL curves for two sets of analysis gates used to isolate events corresponding to the $^{26}\text{O} \rightarrow ^{24}\text{O} + 2n$ decay. The top row shows the results for events extracted using the causality cuts and the bottom row shows the results using the decision forest. In the relative speed plots, the black points represent data and the curves are from simulations with $T_{1/2} = 0$ ps, 4 ps, and 8 ps. The vertical red lines on top of the LnL curves denote the 1σ statistical uncertainties.

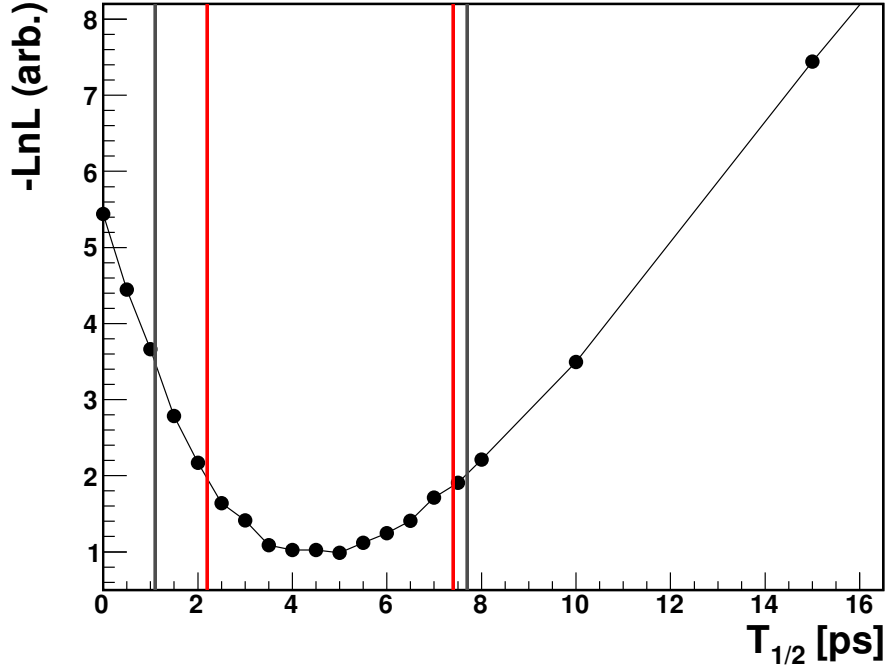


Figure 5.3: The gray vertical lines indicate the upper and lower limits on the half-life obtained from adding, in quadrature, the statistical and systematic uncertainties quoted in Ref. (1). The red vertical lines denote the upper and lower limits and the black points show the negative loglikelihood curve from the current analysis using the causality cuts.

loglikelihoods for the half-lives extracted from the data under these two sets of gates. Using the causality cuts, $T_{1/2} = 5.0^{+1.7}_{-2.2}$ (1σ statistical) ± 1.7 (systematic) ps. Using the decision forest $2n$ cuts $T_{1/2} = 5.0^{+2.0}_{-1.6}$ (stat) ± 1.7 (syst) ps.

The currently adopted value of $4.5^{+3.2}_{-3.4}$ ps (112) for the half-life of the ^{26}O ground state comes from the measurement reported in Ref. (1). The +3.2 ps and -3.4 ps uncertainties come from adding the statistical and systematic errors from Ref. (1) in quadrature. Applying the same procedure to the results stated at the end of the last paragraph gives $T_{1/2} = 5.0^{+2.4}_{-2.8}$ ps for the causality cuts analysis. The upper (lower) error bar is reduced by 0.8 ps (0.6 ps) compared to the currently adopted value. Figure 5.3 illustrates the reduction in the upper and lower limits for the analysis using the causality cuts since this is the same method that was used in Ref. (1) to select two-neutron events. For the decision forest analysis, $T_{1/2} = 5.0^{+2.6}_{-2.3}$ ps, and the upper (lower) error bar is reduced by 0.6 ps (1.1 ps).

Focusing on the decision forest scenario because it has slightly higher statistics, 98 counts

compared to 80 counts, one can conclude that ^{26}O has a non-zero half-life with a 95% confidence level. This is determined by finding the 95% confidence interval to be $1.9 \text{ ps} < T_{1/2} < 9.9 \text{ ps}$. When the lower error bar at 1.9 ps is combined with the 1.7 ps systematic error bar, the resulting lower limit $T_{1/2} = 0.2 \text{ ps}$ excludes zero. In a similar fashion, the result from the causality cuts suggests a non-zero lifetime at a 90% confidence level, where the corresponding interval is $1.9 \text{ ps} < T_{1/2} < 8.1 \text{ ps}$ so the lower 1.6σ error bar is located at 1.9 ps. These results confirm the observation of $2n$ radioactivity from the ground state of ^{26}O , first reported in Ref. (1). Ultimately, a higher confidence level, e.g. $>5\sigma$ (113; 114), is needed to establish a definitive observation of a new form of radioactivity. Analysis is currently underway to extract the ^{26}O half-life from a measurement carried out at the RIKEN Nishina Center's Radioactive Isotope Beam Factory.

5.1.2 Implications

The experimental constraints shown in Figure 2.2 have been adjusted to reflect the $T_{1/2} > 0.2 \text{ ps}$ result from this analysis and the updated plot is shown in Figure 5.4. The measurement from RIKEN establishes the ^{26}O decay energy $E_{\text{decay}} = 18 \pm 7 \text{ keV}$ (48) as indicated by the red vertical lines in Figure 5.4. The figure also shows that only one of the calculations from Ref. (58) is consistent with both the half-life and decay energy measurements. The red dotted line corresponds to calculations where the $n - n$ potential has been reduced by a factor of four. Setting this $n - n$ interaction to zero, see the blue dashed line in Figure 5.4, over-predicts the half-life. Calculations with the full potential, see the purple short-dashed line in Figure 5.4, predict a $T_{1/2}$ that is shorter than the value reported here.

5.2 Segmented Target Evaluation

As discussed in Section 2.4, the uncertainty introduced by the unknown reaction/decay position is a key component that directly influences the decay energy resolution. The analysis procedure (2) from above results in an improved decay energy resolution compared to procedure (1) because it enables a better estimate of the energy addback. This resolution improvement is demonstrated

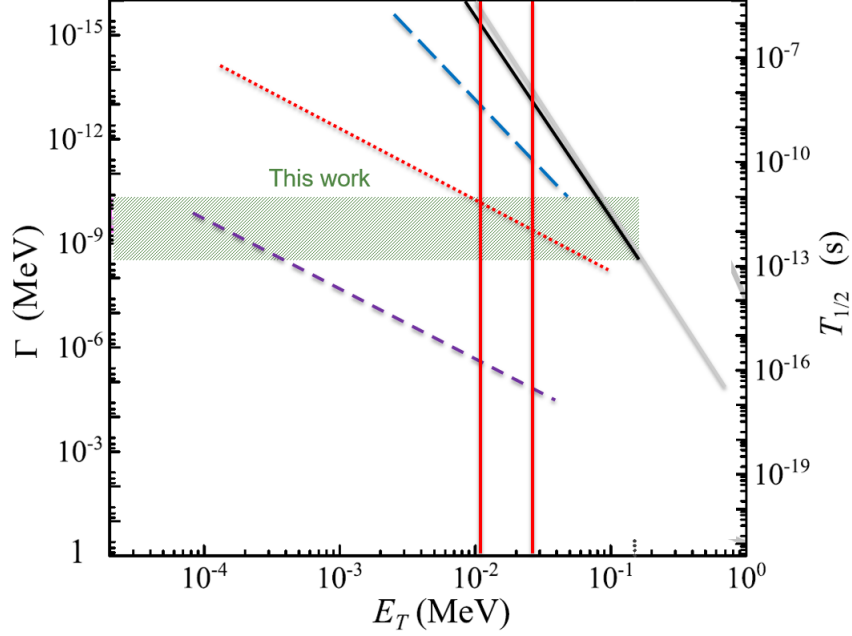


Figure 5.4: Decay width/half-life as a function of decay energy for $2n$ emission from ^{26}O . The gray line assumes a pure orbital $[d^2]$ configuration coupled to the total angular momentum $L = 0$. The solid black curve shows the results when no final state interaction (FSI) and an infinite ^{24}O mass is simulated. The blue dashed line plots the results when no FSI and the correct ^{24}O mass is simulated. The red dotted line shows the calculation results when the $n - n$ FSI is scaled by 0.25, and the purple short-dashed curve includes the full $n - n$ FSI. The vertical red lines roughly indicate the experimental results from (48), and the green shaded area indicates half-life limits obtained in this work. Image adapted from (58).

through the simulation and data analysis of the ^{26}O half-life measurement.

5.2.1 Target Thickness - Simulation

To illustrate the effect that the target thickness has on the decay energy resolution, the reaction $^{27}\text{F}(-1p) \rightarrow ^{26}\text{O} \rightarrow ^{24}\text{O} + 2n$ was simulated using the software package described in Section 4.4. The simulation output has the same format as the calibrated data, so it is processed through the same decay energy calculation that is used for the experimental data. The resulting spectrum has the detector acceptances, efficiencies and resolutions folded in so it is directly comparable to the experimental data.

The right panel in Figure 5.5 compares two decay energy spectra reconstructed from simulations of (1) a single thick (11.1 mm) beryllium target (gray line) and (2) a segmented target (red

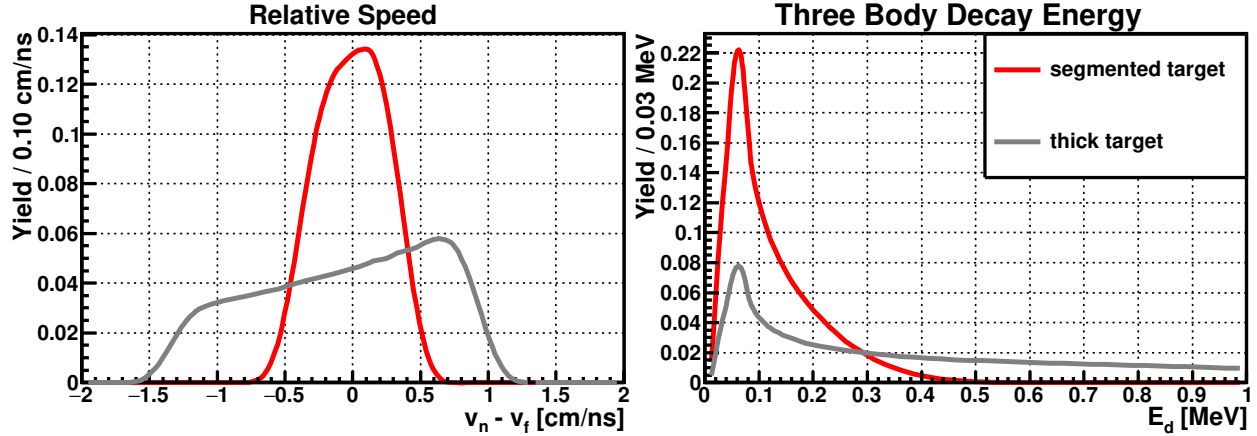


Figure 5.5: Results from a simulation run with a single 11.1 mm target (gray curves) and with a segmented target (red curves). The 11.1 mm target is the sum of the thicknesses of the three beryllium targets used in the segmented target. For the segmented target simulation, the detector and target thicknesses in the simulation are the same as those listed in Table 3.1. The left panel plots the difference in speed $|\vec{v}_n| - |\vec{v}_f|$ between the first detected neutron and the charged fragment and the right panel plots the three body decay energy reconstructed from the simulation. Deviation from the 50 keV input decay energy is due to the energy addback. Neutron resolutions are turned off.

line) consisting of three separate pieces of beryllium 4.1 mm, 3.7 mm and 3.3 mm thick. The input decay energy for every event in both simulations is 50 keV. For both the red and the gray lines, the reconstructed decay energies are broadened relative to the input distribution because of the uncertainty in the reaction/decay location within the target. Resolution effects for the neutron measurements are turned off.

The left panel in Figure 5.5 compares the neutron-fragment relative speed distributions for the thick (gray curve) and segmented (red curve) target simulations. The relative speed is calculated as $|\vec{v}_n| - |\vec{v}_f|$ where $v_f = v_0 + v_{\text{addback}}$ and $v_{\text{addback}} \propto \sqrt{E_{\text{addback}}}$ represents the adjustment (due to the kinetic energy addback) to the measured velocity v_0 . For the low decay energy case simulated here, the lab frame neutron and fragment velocities are similar to the beam velocity at the decay vertex. After the decay the fragment travels through the remainder of the target material and loses energy. The energy addback serves to account for this loss and recover the kinetic energy at the vertex. Since the average reaction/decay position is the center of the target, the energy addback is estimated as the energy lost by a fragment produced at the center of the target. The

deviation from zero of the relative speed distribution's centroid quantifies how well this estimate reproduces the event-by-event actual energy loss. The width of the relative speed distribution is related to the thickness of the target and the decay energy of the unbound resonance. At fixed decay energy, a thicker target implies a larger spread of reaction/decay points around the target center which translates to a larger spread of actual energy losses around the chosen addback value. This introduces a spread in the relative speed proportional to the target thickness as illustrated by the difference between the gray and red curves in the left panel of Figure 5.5.

5.2.2 Improved decay energy resolution

Figure 5.6 shows the relative speed and three-body decay-energy spectra reconstructed from data (points) and simulation (curves). In the top row of Figure 5.6, the reconstruction used energy loss information from the silicon detectors to identify event-by-event the segment in which the proton knockout occurred. Based on this identification the appropriate energy addback (see Table 4.7) was then used to reconstruct the fragment momentum. In the bottom row of Figure 5.6, the addback to the center of the middle beryllium segment was used in the reconstruction for all events. Just as in the simulated case (Figure 5.5) there is a substantial improvement in the decay energy resolution of the segmented target spectrum compared to the single thick target reconstruction.

As mentioned above, the spread of the relative speed distribution is related to the target thickness and to the decay energy which is partitioned among the fragment and neutrons. When more energy is available in the decay the difference between the momenta of the daughter products will be larger. This is why the upper and lower tails (e.g. the upper left panel in Figure 5.6) of the relative speed distribution correspond to higher decay energies (see also Eq. 3.3). For low decay energies, like the ^{26}O ground state, a large mismatch between the actual fragment energy loss and the estimated value results in artificially high decay energies; note the much larger tail on the low energy peak in the bottom right panel compared to the upper right panel in Figure 5.6.

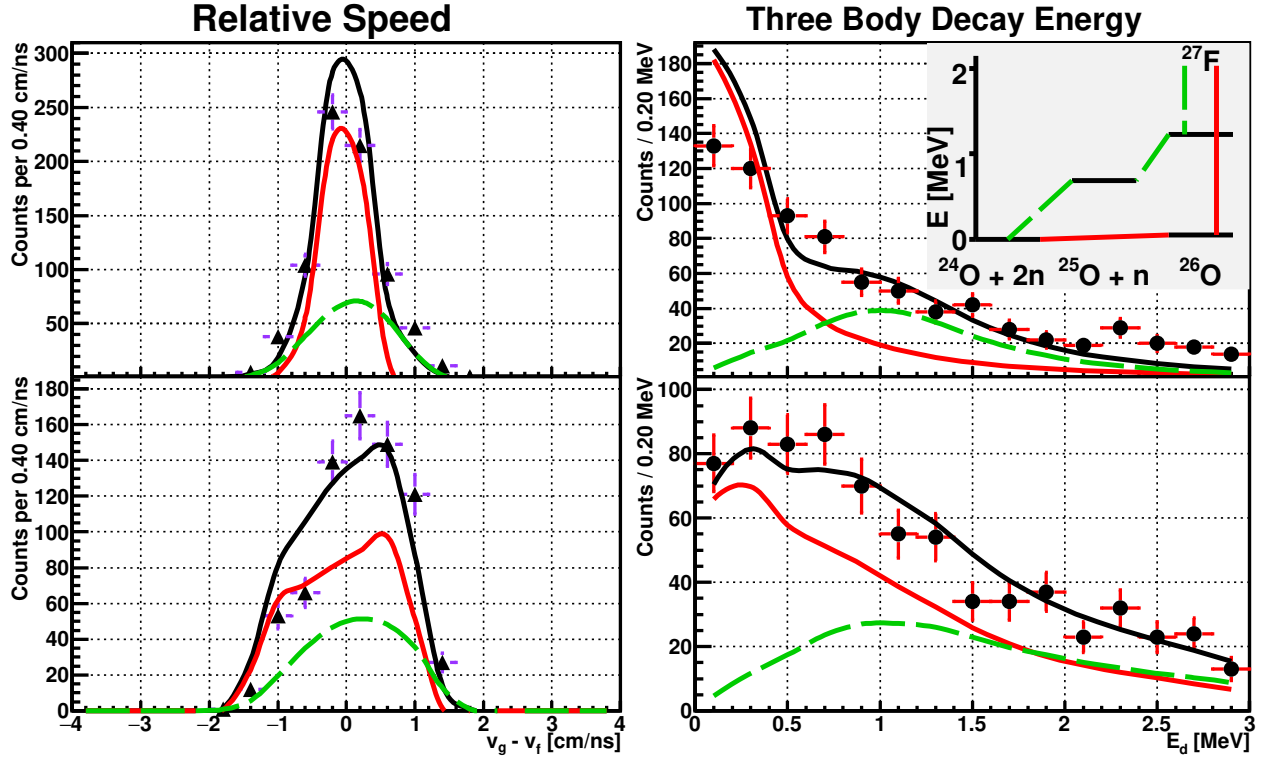


Figure 5.6: Measured relative speed and three body decay energy spectra for $^{27}\text{F}(-1p) \rightarrow ^{26}\text{O} \rightarrow ^{24}\text{O} + 2n$ are drawn as black triangles and black circles, respectively. The solid curves are spectra reconstructed from simulation. Two different decay channels were simulated (see inset of top right panel): (1) direct population of the ^{26}O ground state followed by two-neutron emission (red solid line) and (2) population of the ^{26}O first excited state followed by a sequential neutron emission through the ^{25}O ground state (green dashed line). In the top row, the energy addback is chosen event-by-event based on which beryllium segment was identified as the reaction target using the method described in Section 4.1.1.2. In the bottom row, the addback for the middle beryllium segment is applied to all events.

5.2.3 Resolution Improvements and the Half-life Measurement

Figure 5.7 plots the relative speed distributions and the negative loglikelihood (LnL) curves extracted using the target identification to inform the energy addback (top panels) and assuming a single thick target (bottom panels). The comparison in Figure 5.7 shows that the relative speed distribution for a single thick target would not have provided a sensitive measure of the half-life.

In cases where one needs to discriminate between two decay channels like the ones shown in Figure 5.6, the improved resolution offered by the segmented target allows for a cleaner gate on the three body decay energy which provides better statistics for studies of a single unbound resonance.

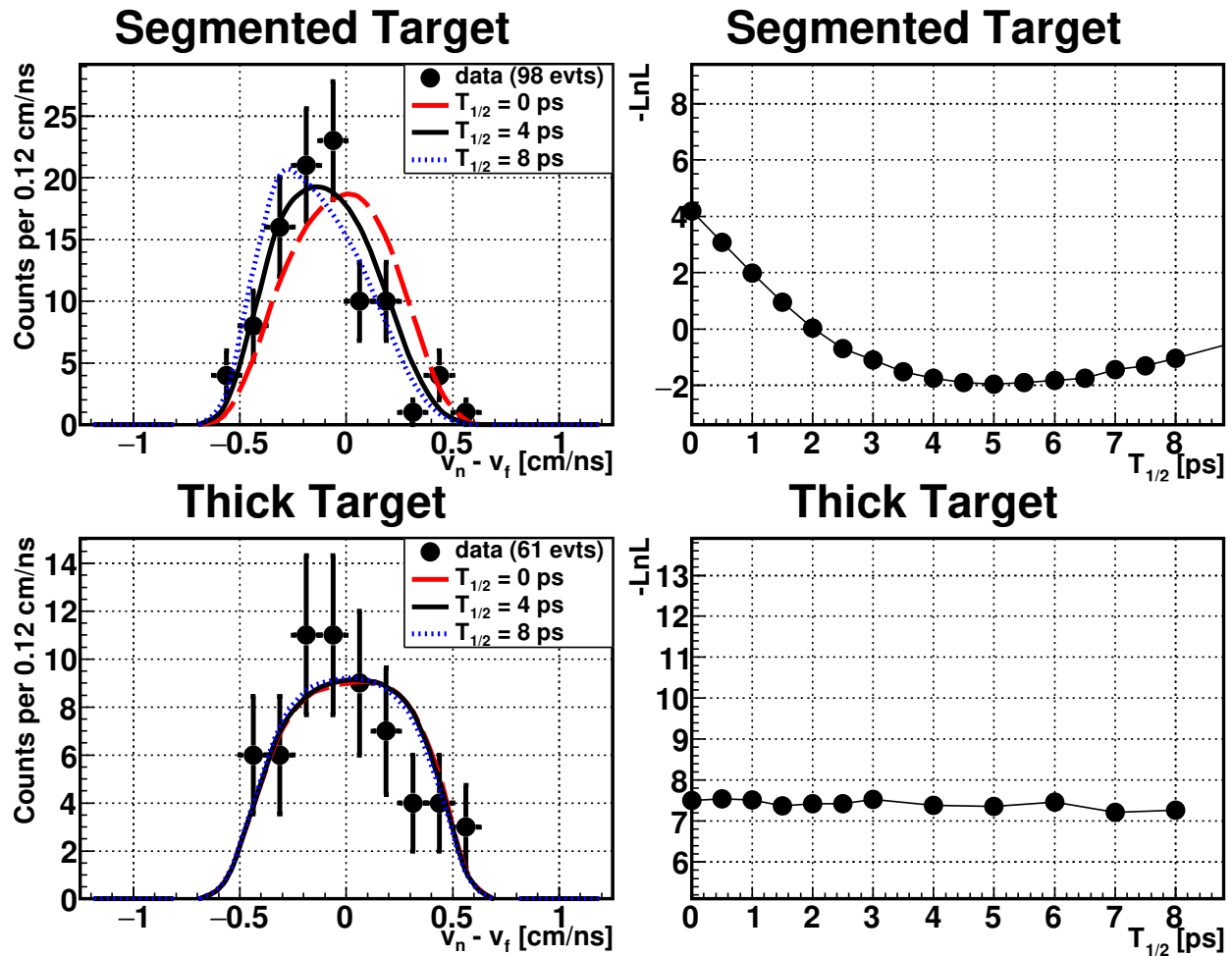


Figure 5.7: The top left plot shows the relative speed reconstructed using the target identification (Section 4.1.1.2) to inform the energy addback. The black points are data and the curves represent relative speed distributions simulated assuming various $T_{1/2}$ for ^{26}O - red dashed is 0 ps, black solid is 4 ps and blue dotted corresponds to 8 ps. In the bottom left a single value for the addback (corresponding to the energy loss through half of a single thick target) is used for all measured and simulated events. The right panels show the extracted negative loglikelihood curves for the segmented (top) and single thick (bottom) target reconstructions.

The half-life measurement requires selecting events where the decay of the ^{26}O ground state was observed. Events where the decay of the 2^+ state was observed represent background because this state is not expected to be long-lived. Event-by-event discrimination between these two types of events is enhanced by the improved decay energy resolution provide by the segmented target.

CHAPTER 6

SUMMARY AND CONCLUSIONS

6.1 Half-life measurement

In summary, the lifetime of the ^{26}O ground state was extracted using two different approaches for suppressing false $2n$ (background) events. Both results are consistent within the 1σ statistical errors. The systematic uncertainty was determined by extracting an upper limit for the half-life of the first unbound excited state in ^{23}O . The results of the half-life measurement are consistent with those of Ref. (1) and suggest a half-life for the ^{26}O $2n$ decay on the order of picoseconds which meets the criteria for radioactivity. A lower limit $T_{1/2} > 0.2$ ps was determined at a 95% confidence level. This result together with the decay energy measurement from Ref. (48) constrains the strength of the $n - n$ final state interaction used in the calculations from Ref. (58).

A logical extension of this work is to consider whether $2n$ radioactivity is unique to ^{26}O or if other nuclei might exhibit this exotic decay mode. A purely qualitative discussion of this question can be based around the three criteria listed in Section 2.2.3. Naively, one could expect that the valence neutrons in certain heavier systems could occupy orbitals with higher angular momenta thus increasing the potential barrier and subsequently the half-life for two-neutron emission. However, the increasing nuclear level density near the neutron threshold for heavier systems (115; 116) must be taken into account. This trend corresponds to a decrease in the likelihood to have no intermediate states in the two-neutron emission process (see Figure 2.1), and this conflicts with the requirement stated in item (1) from the list in Section 2.2.3. A balance between these two general trends could allow for $2n$ radioactivity from a handful of nuclei heavier than ^{26}O .

Furthermore, the development of theoretical frameworks like the Gamow shell model (117; 118; 119) has highlighted the importance of incorporating scattering and decay channels into shell model calculations. An interesting conjecture based on these theoretical developments holds that coupling to cluster decay channels (e.g. $2n$ emission) imprints cluster correlations on the shell

model wavefunctions (120; 121). From this perspective, the organization of nucleons into clusters inside the nucleus is viewed as a near-threshold phenomenon and not as a consequence of properties of the Hamiltonian or some symmetry of the nuclear many-body problem. This interpretation suggests that certain systems near the $2n$ emission threshold could have energy level schemes that meet the simultaneous (cluster) emission requirement (see Figure 2.1 and item (1) from Section 2.2.3), thus enhancing the possibility to find more cases of $2n$ radioactivity.

6.2 Segmented Target

A new device was developed for use in invariant mass spectroscopy of neutron unbound states at the NSCL. It currently consists of three beryllium targets interleaved between four silicon detectors. The energy loss measured in each silicon allows the reaction that produces the unbound state to be localized to a particular beryllium segment. This improves the accuracy of the energy addback used to reconstruct the fragment momentum. The result is a thicker reaction target for improved reaction yield without sacrificing decay energy resolution.

In order to evaluate the performance of the segmented target, two versions of the analysis were conducted: (1) a single target equal in thickness to the sum of the three beryllium segments was assumed when calculating the energy addback and (2) the dE measurements were used to identify the target segment containing the reaction and the addback for that particular segment was applied. Method (2) results in a better reconstruction of the fragment momentum. Consequently, the relative speed and decay energy resolutions were much improved in method (2) compared to method (1).

The increased reaction yield was critical in light of the CRDC 1 electronics board failure discussed in Section 4.1.2.2. This malfunction reduced the efficiency of the charged particle position measurement by a factor of two. Based on simulations with twice the statistics, the total width of the 1σ confidence interval could be reduced by approximately 20% relative to its $1.7 + 2.2 = 3.9$ ps ($2.0 + 1.6 = 3.6$ ps for the decision forest analysis) width reported in the previous chapter.

BIBLIOGRAPHY

BIBLIOGRAPHY

- [1] Z. Kohley *et al.*, *Phys. Rev. Lett.*, **110**, 152501, 2013.
- [2] This Month in Physics History, *APS News*. March 2008, Vol. 17, No. 3.
- [3] From *Nobel Lectures, Physics 1901-1921*. Elsevier Publishing Company, Amsterdam, 1967.
- [4] H. Becquerel, *Comptes Rendus Acad Sci, Paris*, **122**, 501–3, 1896.
- [5] H. Becquerel, *Comptes Rendus Acad Sci, Paris*, **122**, 501, 1896.
- [6] H. Becquerel, *Comptes Rendus Acad Sci, Paris*, **122**, 559, 1896.
- [7] H. Becquerel, *Comptes Rendus Acad Sci, Paris*, **122**, 689–694, 1896.
- [8] H. Becquerel, *Comptes Rendus Acad Sci, Paris*, **122**, 762, 1896.
- [9] H. Becquerel, *Comptes Rendus Acad Sci, Paris*, **122**, 1086, 1896.
- [10] H. Becquerel, *Sur diverses propriétés des rayons uraniques* (Gauthier-Villars 1896).
- [11] This Month in Physics History, *APS News*. May 2006, Vol. 15, No. 5.
- [12] This Month in Physics History, *APS News*. May 2007, Vol. 16, No. 5.
- [13] From *Nobel Lectures, Physics 1922-1941*. Elsevier Publishing Company, Amsterdam, 1965.
- [14] G. Audi, F. G. Kondev, M. Wang, W. Huang, and S. Naimi, *Chinese Physics C*, **41**(3), 030001, 2017.
URL <http://dx.doi.org/10.1088/1674-1137/41/3/030001>
- [15] M. G. Mayer, *Phys. Rev.*, **74**, 235–239, 1948.
URL <http://dx.doi.org/10.1103/PhysRev.74.235>
- [16] M. G. Mayer, *Phys. Rev.*, **75**, 1969–1970, 1949.
URL <http://dx.doi.org/10.1103/PhysRev.75.1969>
- [17] K. Krane, *Introductory Nuclear Physics* (Wiley, New York, NY 1988).
URL <https://cds.cern.ch/record/359790>
- [18] M. G. Mayer, *Phys. Rev.*, **78**, 16–21, 1950.
URL <http://dx.doi.org/10.1103/PhysRev.78.16>
- [19] M. G. Mayer, *Phys. Rev.*, **78**, 22–23, 1950.
URL <http://dx.doi.org/10.1103/PhysRev.78.22>
- [20] O. Haxel, J. H. D. Jensen, and H. E. Suess, *Phys. Rev.*, **75**, 1766–1766, 1949.
URL <http://dx.doi.org/10.1103/PhysRev.75.1766.2>

- [21] A. Brown, *Lecture Notes in Nuclear Structure Physics*, national Superconducting Cyclotron Laboratory and Department of Physics and Astronomy, East Lansing, MI, USA, 2011.
- [22] M. Thoennessen, *Reports on Progress in Physics*, **67**(7), 1187–1232, 2004.
URL <http://dx.doi.org/10.1088/0034-4885/67/7/r04>
- [23] M. Pfützner, M. Karny, L. V. Grigorenko, and K. Riisager, *Reviews of Modern Physics*, **84**(2), 567–619, 2012.
URL <http://dx.doi.org/10.1103/RevModPhys.84.567>
- [24] M. Thoennessen, *The Discovery of Isotopes* (Springer, Cham 2016).
URL <https://doi-org.proxy1.cl.msu.edu/10.1007/978-3-319-31763-2>
- [25] J. Erler, N. Birge, M. Kortelainen, W. Nazarewicz, E. Olsen, A. M. Perhac, and M. Stoitsov, *Nature*, **486**(7404), 509–512, 2012.
URL <http://dx.doi.org/10.1038/nature11188>
- [26] G. Gamow, *Zeitschrift für Physik*, **51**(3), 204–212, 1928.
URL <http://dx.doi.org/10.1007/BF01343196>
- [27] R. W. Gurney and E. U. Condon, *Nature*, 1928.
URL <http://dx.doi.org/10.1038/122439a0>
- [28] G. Knoll, *Radiation Detection and Measurement* (Wiley 1989).
URL <https://books.google.com/books?id=UCt1QgAACAAJ>
- [29] R. Dunlap, *An Introduction to the Physics of Nuclei and Particles* (Thomson Brooks/Cole 2004).
URL <https://books.google.com/books?id=UZN9QgAACAAJ>
- [30] K. Jackson, C. Cardinal, H. Evans, N. Jelley, and J. Cerny, *Physics Letters B*, **33**(4), 281 – 283, 1970.
URL [http://dx.doi.org/https://doi.org/10.1016/0370-2693\(70\)90269-8](http://dx.doi.org/https://doi.org/10.1016/0370-2693(70)90269-8)
- [31] S. Hofmann, W. Reisdorf, G. Münzenberg, F. P. Heßberger, J. R. H. Schneider, and P. Armbruster, *Zeitschrift für Physik A Atoms and Nuclei*, **305**(2), 111–123, 1982.
URL <http://dx.doi.org/10.1007/BF01415018>
- [32] Y. B. Zel’dovich, *J. Exptl. Theoret. Phys. (U.S.S.R.)*, **38**, 1123–1131, 1960.
- [33] V. I. Goldansky, *Nuclear Physics*, **19**, 482–495, 1960.
URL [http://dx.doi.org/10.1016/0029-5582\(60\)90258-3](http://dx.doi.org/10.1016/0029-5582(60)90258-3)
- [34] D. F. Geesaman, R. L. McGrath, P. M. S. Lesser, P. P. Urone, and B. VerWest, *Phys. Rev. C*, **15**, 1835–1838, 1977.
URL <http://dx.doi.org/10.1103/PhysRevC.15.1835>
- [35] O. V. Bochkarev, A. A. Korshennikov, E. A. Kuz’min, I. G. Mukha, A. A. Ogloblin, L. V. Chulkov, and G. B. Yan’kov, *ZhETF Pisma Redaktsiiu*, **40**, 204, 1984.

- [36] G. J. KeKelis, M. S. Zisman, D. K. Scott, R. Jahn, D. J. Vieira, J. Cerny, and F. Ajzenberg-Selove, *Phys. Rev. C*, **17**, 1929–1938, 1978.
URL <http://dx.doi.org/10.1103/PhysRevC.17.1929>
- [37] R. A. Kryger *et al.*, *Phys. Rev. Lett.*, **74**, 860–863, 1995.
URL <http://dx.doi.org/10.1103/PhysRevLett.74.860>
- [38] M. Pfützner *et al.*, *The European Physical Journal A - Hadrons and Nuclei*, **14**(3), 279–285, 2002.
URL <http://dx.doi.org/10.1140/epja/i2002-10033-9>
- [39] H. Liu, *Reaction Mechanism Dependence of the Population and Decay of He-10*, Ph.D. thesis, Michigan State University, 2019.
- [40] M. Meister *et al.*, *Phys. Rev. Lett.*, **91**, 162504, 2003.
URL <http://dx.doi.org/10.1103/PhysRevLett.91.162504>
- [41] M. S. Golovkov *et al.*, *Phys. Rev. Lett.*, **93**, 262501, 2004.
URL <http://dx.doi.org/10.1103/PhysRevLett.93.262501>
- [42] M. S. Golovkov *et al.*, *Phys. Rev. C*, **72**, 064612, 2005.
URL <http://dx.doi.org/10.1103/PhysRevC.72.064612>
- [43] Z. Kohley *et al.*, *Phys. Rev. C*, **87**, 011304, 2013.
URL <http://dx.doi.org/10.1103/PhysRevC.87.011304>
- [44] Y. Aksyutina *et al.*, *Physics Letters B*, **666**(5), 430 – 434, 2008.
URL <http://dx.doi.org/https://doi.org/10.1016/j.physletb.2008.07.093>
- [45] A. Spyrou *et al.*, *Phys. Rev. Lett.*, **108**, 102501, 2012.
URL <http://dx.doi.org/10.1103/PhysRevLett.108.102501>
- [46] E. Lunderberg *et al.*, *Phys. Rev. Lett.*, **108**, 142503, 2012.
- [47] C. Caesar *et al.*, *Phys. Rev. C*, **88**, 034313, 2013.
URL <http://dx.doi.org/10.1103/PhysRevC.88.034313>
- [48] Y. Kondo *et al.*, *Phys. Rev. Lett.*, **116**, 102503, 2016.
URL <http://dx.doi.org/10.1103/PhysRevLett.116.102503>
- [49] A. H. Wuosmaa *et al.*, *Phys. Rev. C*, **95**, 014310, 2017.
URL <http://dx.doi.org/10.1103/PhysRevC.95.014310>
- [50] L. V. Grigorenko, I. G. Mukha, C. Scheidenberger, and M. V. Zhukov, *Phys. Rev. C*, **84**, 021303, 2011.
URL <http://dx.doi.org/10.1103/PhysRevC.84.021303>
- [51] D. Guillemaud-Mueller *et al.*, *Phys. Rev. C*, **41**, 937–941, 1990.
URL <http://dx.doi.org/10.1103/PhysRevC.41.937>

- [52] M. Fauerbach, D. J. Morrissey, W. Benenson, B. A. Brown, M. Hellström, J. H. Kelley, R. A. Kryger, R. Pfaff, C. F. Powell, and B. M. Sherrill, *Phys. Rev. C*, **53**, 647–651, 1996.
URL <http://dx.doi.org/10.1103/PhysRevC.53.647>
- [53] S. M. Lukyanov and Y. E. Penionzhkevich, *Physics of Atomic Nuclei*, **67**, 1627–1632, 2004.
URL <http://dx.doi.org/10.1134/1.1802348>
- [54] A. Schiller, T. Baumann, J. Dietrich, S. Kaiser, W. Peters, and M. Thoennessen, *Phys. Rev. C*, **72**, 037601, 2005.
URL <http://dx.doi.org/10.1103/PhysRevC.72.037601>
- [55] M. Thoennessen, G. Christian, Z. Kohley, T. Baumann, M. Jones, J. K. Smith, J. Snyder, and A. Spyrou, *Nuclear Instruments and Methods in Physics Research, Section A: Accelerators, Spectrometers, Detectors and Associated Equipment*, 2013.
URL <http://dx.doi.org/10.1016/j.nima.2013.07.035>
- [56] Looking at Physics History, *Capitol Hill Quaterly (APS)*. July 2000, Vol. 6, No. 2.
- [57] W. von Schlippe, relativistic Kinematics of Particle Interactions, March 2002
http://www.physics.utah.edu/~jui/5110/hw/kin_rel.pdf.
URL http://www.physics.utah.edu/~jui/5110/hw/kin_rel.pdf
- [58] L. V. Grigorenko, I. G. Mukha, and M. V. Zhukov, *Phys. Rev. Lett.*, **111**, 042501, 2013.
URL <http://dx.doi.org/10.1103/PhysRevLett.111.042501>
- [59] L. V. Grigorenko and M. V. Zhukov, *Phys. Rev. C*, **91**, 064617, 2015.
URL <http://dx.doi.org/10.1103/PhysRevC.91.064617>
- [60] K. Hagino and H. Sagawa, *Phys. Rev. C*, **93**, 034330, 2016.
URL <http://dx.doi.org/10.1103/PhysRevC.93.034330>
- [61] L. V. Grigorenko, R. C. Johnson, I. G. Mukha, I. J. Thompson, and M. V. Zhukov, *Phys. Rev. Lett.*, **85**, 22–25, 2000.
URL <http://dx.doi.org/10.1103/PhysRevLett.85.22>
- [62] C. R. Hoffman *et al.*, *Phys. Rev. Lett.*, **100**, 152502, 2008.
- [63] G. Cowan, *Statistical Data Analysis*, Oxford science publications (Clarendon Press 1998).
URL <https://books.google.com/books?id=ff8ZyW0n1JAC>
- [64] G. Christian *et al.*, *Physical Review Letters*, **108**(3), 1–5, 2012.
URL <http://dx.doi.org/10.1103/PhysRevLett.108.032501>
- [65] S. Leblond *et al.*, *Phys. Rev. Lett.*, **121**, 262502, 2018.
URL <http://dx.doi.org/10.1103/PhysRevLett.121.262502>
- [66] T. Baumann, A. Spyrou, and M. Thoennessen, *Reports on Progress in Physics*, **75**(3), 036301, 2012.
URL <http://dx.doi.org/10.1088/0034-4885/75/3/036301>

- [67] Y. Ayyad *et al.*, Nuclear Instruments and Methods in Physics Research Section A: Accelerators, Spectrometers, Detectors and Associated Equipment, 2018.
URL <http://dx.doi.org/https://doi.org/10.1016/j.nima.2018.10.019>
- [68] T. Furuno *et al.*, Nuclear Instruments and Methods in Physics Research Section A: Accelerators, Spectrometers, Detectors and Associated Equipment, **908**, 215 – 224, 2018.
URL <http://dx.doi.org/https://doi.org/10.1016/j.nima.2018.08.042>
- [69] A. Laird *et al.*, Nuclear Instruments and Methods in Physics Research Section A: Accelerators, Spectrometers, Detectors and Associated Equipment, **573**(1), 306 – 309, 2007, proceedings of the 7th International Conference on Position-Sensitive Detectors.
URL <http://dx.doi.org/https://doi.org/10.1016/j.nima.2006.10.384>
- [70] S. Beceiro-Novo, T. Ahn, D. Bazin, and W. Mittig, Progress in Particle and Nuclear Physics, **84**, 124 – 165, 2015.
URL <http://dx.doi.org/https://doi.org/10.1016/j.pnpnp.2015.06.003>
- [71] W. Rogers, A. Kuchera, J. Boone, N. Frank, S. Mosby, M. Thoennessen, and A. Wantz, Nuclear Instruments and Methods in Physics Research Section A: Accelerators, Spectrometers, Detectors and Associated Equipment, **943**, 162436, 2019.
URL <http://dx.doi.org/https://doi.org/10.1016/j.nima.2019.162436>
- [72] F. Marti, P. Miller, D. Poe, M. Steiner, J. Stetson, and X. Y. Wu, in F. Marti (editor), *Cyclotrons and Their Applications 2001*, volume 600 of *American Institute of Physics Conference Series*, 64–68 (2001).
URL <http://dx.doi.org/10.1063/1.1435199>
- [73] D. J. Morrissey, B. M. Sherrill, M. Steiner, A. Stolz, and I. Wiedenhoever, Nuclear Instruments and Methods in Physics Research B, **204**, 90–96, 2003.
URL [http://dx.doi.org/10.1016/S0168-583X\(02\)01895-5](http://dx.doi.org/10.1016/S0168-583X(02)01895-5)
- [74] I. Tanihata, Nuclear Physics A, **553**, 361 – 372, 1993.
URL [http://dx.doi.org/https://doi.org/10.1016/0375-9474\(93\)90636-C](http://dx.doi.org/https://doi.org/10.1016/0375-9474(93)90636-C)
- [75] M. S. Basunia, Nuclear Data Sheets, **112**(8), 1875 – 1948, 2011.
URL <http://dx.doi.org/https://doi.org/10.1016/j.nds.2011.08.001>
- [76] M. D. Jones, *Spectroscopy of Neutron Unbound States in O-24 and N-23*, Ph.D. thesis, Michigan State University, 2015.
- [77] M. D. Bird, S. J. Kenney, J. Toth, H. W. Weijers, J. C. DeKamp, M. Thoennessen, and A. F. Zeller, IEEE Transactions on Applied Superconductivity, **15**(2 PART II), 1252–1254, 2005.
URL <http://dx.doi.org/10.1109/TASC.2005.849553>
- [78] N. Frank, *Spectroscopy of Neutron Unbound States in Neutron Rich Oxygen Isotopes*, Ph.D. thesis, Michigan State University, 2006.

- [79] B. Luther *et al.*, Nuclear Instruments and Methods in Physics Research Section A: Accelerators, Spectrometers, Detectors and Associated Equipment, **505**(1), 33 – 35, 2003, proceedings of the tenth Symposium on Radiation Measurements and Applications.
URL [http://dx.doi.org/https://doi.org/10.1016/S0168-9002\(03\)01014-3](http://dx.doi.org/https://doi.org/10.1016/S0168-9002(03)01014-3)
- [80] T. Baumann *et al.*, Nuclear Instruments and Methods in Physics Research, Section A: Accelerators, Spectrometers, Detectors and Associated Equipment, **543**(2-3), 517–527, 2005.
URL <http://dx.doi.org/10.1016/j.nima.2004.12.020>
- [81] K. Stiefel, *Measurement and Modeling of Fragments and Neutrons Produced from Projectile Fragmentation Reactions*, Ph.D. thesis, Michigan State University, 2018.
- [82] W. Peters, *Study of Neutron Unbound States Using the Modular Neutron Array*, Ph.D. thesis, Michigan State University, 2007.
- [83] G. A. Christian, *Spectroscopy of Neutron-Unbound Fluorine*, Ph.D. thesis, Michigan State University, 2011.
- [84] J. Paul, Nuclear Instruments and Methods, **96**(1), 51 – 59, 1971.
URL [http://dx.doi.org/https://doi.org/10.1016/0029-554X\(71\)90436-8](http://dx.doi.org/https://doi.org/10.1016/0029-554X(71)90436-8)
- [85] O. B. Tarasov and D. Bazin, Nuclear Instruments and Methods in Physics Research, Section B: Beam Interactions with Materials and Atoms, **266**(19-20), 4657–4664, 2008.
URL <http://dx.doi.org/10.1016/j.nimb.2008.05.110>
- [86] S. Matsuno *et al.*, Phys. Rev. D, **29**, 1–23, 1984.
URL <http://dx.doi.org/10.1103/PhysRevD.29.1>
- [87] M. D. Jones *et al.*, Phys. Rev. C, **92**, 051306, 2015.
URL <http://dx.doi.org/10.1103/PhysRevC.92.051306>
- [88] J. K. Smith *et al.*, Phys. Rev. C, **90**, 024309, 2014.
URL <http://dx.doi.org/10.1103/PhysRevC.90.024309>
- [89] Z. Kohley *et al.*, Phys. Rev. C, **87**, 011304, 2013.
URL <http://dx.doi.org/10.1103/PhysRevC.87.011304>
- [90] A. Spyrou *et al.*, Phys. Rev. Lett., **108**, 102501, 2012.
URL <http://dx.doi.org/10.1103/PhysRevLett.108.102501>
- [91] Z. Kohley *et al.*, Phys. Rev. Lett., **109**, 232501, 2012.
URL <http://dx.doi.org/10.1103/PhysRevLett.109.232501>
- [92] C. R. Hoffman *et al.*, Phys. Rev. C, **83**, 031303, 2011.
URL <http://dx.doi.org/10.1103/PhysRevC.83.031303>
- [93] T. Nakamura *et al.*, Phys. Rev. Lett., **96**, 252502, 2006.
URL <http://dx.doi.org/10.1103/PhysRevLett.96.252502>

- [94] F. M. Marqués, M. Labiche, N. A. Orr, F. Sarazin, and J. C. Angélique, *Nuclear Instruments and Methods in Physics Research A*, **450**, 109–118, 2000.
URL [http://dx.doi.org/10.1016/S0168-9002\(00\)00248-5](http://dx.doi.org/10.1016/S0168-9002(00)00248-5)
- [95] A. Hoecker, P. Speckmayer, J. Stelzer, J. Therhaag, E. von Toerne, and H. Voss, *PoS, ACAT*, 040, 2007.
- [96] R. Brun and F. Rademakers, *Nucl. Instrum. Meth.*, **A389**, 81–86, 1997.
URL [http://dx.doi.org/10.1016/S0168-9002\(97\)00048-X](http://dx.doi.org/10.1016/S0168-9002(97)00048-X)
- [97] N. Frank, A. Schiller, D. Bazin, W. Peters, and M. Thoennessen, *Nuclear Instruments and Methods in Physics Research Section A: Accelerators, Spectrometers, Detectors and Associated Equipment*, **580**(3), 1478 – 1484, 2007.
URL <http://dx.doi.org/http://dx.doi.org/10.1016/j.nima.2007.07.008>
- [98] S. Agostinelli *et al.*, *Nuclear Instruments and Methods in Physics Research Section A: Accelerators, Spectrometers, Detectors and Associated Equipment*, **506**(3), 250 – 303, 2003.
URL [http://dx.doi.org/https://doi.org/10.1016/S0168-9002\(03\)01368-8](http://dx.doi.org/https://doi.org/10.1016/S0168-9002(03)01368-8)
- [99] J. Allison *et al.*, *IEEE Transactions on Nuclear Science*, **53**(1), 270–278, 2006.
URL <http://dx.doi.org/10.1109/TNS.2006.869826>
- [100] J. Allison *et al.*, *Nuclear Instruments and Methods in Physics Research Section A: Accelerators, Spectrometers, Detectors and Associated Equipment*, **835**, 186 – 225, 2016.
URL <http://dx.doi.org/https://doi.org/10.1016/j.nima.2016.06.125>
- [101] B. Roeder, Development and validation of neutron detection simulations for EURISOL, EURISOL Design Study, Report No. 10-25-2018-006, 2008.
URL http://ns.ph.liv.ac.uk/eurisol/M3_in-beam_validations.pdf
- [102] Z. Kohley *et al.*, *Nuclear Instruments and Methods in Physics Research Section A: Accelerators, Spectrometers, Detectors and Associated Equipment*, **682**, 59 – 65, 2012.
URL <http://dx.doi.org/https://doi.org/10.1016/j.nima.2012.04.060>
- [103] J. Biersack and L. Hagmark, *Nuclear Instruments and Methods*, **174**(1), 257 – 269, 1980.
URL [http://dx.doi.org/https://doi.org/10.1016/0029-554X\(80\)90440-1](http://dx.doi.org/https://doi.org/10.1016/0029-554X(80)90440-1)
- [104] J. F. Ziegler and J. P. Biersack, *The Stopping and Range of Ions in Matter*, 93–129 (Springer US, Boston, MA 1985).
URL http://dx.doi.org/10.1007/978-1-4615-8103-1_3
- [105] A. Goldhaber, *Physics Letters B*, **53**(4), 306 – 308, 1974.
URL [http://dx.doi.org/https://doi.org/10.1016/0370-2693\(74\)90388-8](http://dx.doi.org/https://doi.org/10.1016/0370-2693(74)90388-8)
- [106] K. Van Bibber *et al.*, *Phys. Rev. Lett.*, **43**, 840–844, 1979.
- [107] A. Schiller *et al.*, *Phys. Rev. Lett.*, **99**, 112501, 2007.
URL <http://dx.doi.org/10.1103/PhysRevLett.99.112501>

- [108] N. Frank *et al.*, Nuclear Physics A, **813**(3), 199 – 211, 2008.
URL <http://dx.doi.org/https://doi.org/10.1016/j.nuclphysa.2008.09.009>
- [109] G. Christian *et al.*, Nuclear Physics A, **801**(3), 101 – 113, 2008.
URL <http://dx.doi.org/https://doi.org/10.1016/j.nuclphysa.2008.01.004>
- [110] F. James, Monte Carlo Phase Space, CERN, 1968.
URL <http://cds.cern.ch/record/275743/files/CERN-68-15.pdf?version=1>
- [111] D. M. Schmidt, R. J. Morrison, and M. S. Witherell, Nuclear Inst. and Methods in Physics Research, A, **328**(3), 547–552, 1993.
URL [http://dx.doi.org/10.1016/0168-9002\(93\)90674-7](http://dx.doi.org/10.1016/0168-9002(93)90674-7)
- [112] M. Basunia and A. Hurst, Nuclear Data Sheets, **134**, 1 – 148, 2016.
URL <http://dx.doi.org/https://doi.org/10.1016/j.nds.2016.04.001>
- [113] G. Aad *et al.*, Physics Letters B, **716**(1), 1 – 29, 2012.
URL <http://dx.doi.org/https://doi.org/10.1016/j.physletb.2012.08.020>
- [114] S. Chatrchyan *et al.*, Physics Letters B, **716**(1), 30 – 61, 2012.
URL <http://dx.doi.org/https://doi.org/10.1016/j.physletb.2012.08.021>
- [115] H. A. Bethe, Phys. Rev., **50**, 332–341, 1936.
URL <http://dx.doi.org/10.1103/PhysRev.50.332>
- [116] P. Leboeuf and J. Roccia, Phys. Rev. Lett., **97**, 010401, 2006.
URL <http://dx.doi.org/10.1103/PhysRevLett.97.010401>
- [117] N. Michel, W. Nazarewicz, M. Płoszajczak, and K. Bennaceur, Phys. Rev. Lett., **89**, 042502, 2002.
URL <http://dx.doi.org/10.1103/PhysRevLett.89.042502>
- [118] R. Id Betan, R. J. Liotta, N. Sandulescu, and T. Vertse, Phys. Rev. Lett., **89**, 042501, 2002.
URL <http://dx.doi.org/10.1103/PhysRevLett.89.042501>
- [119] N. Michel, W. Nazarewicz, M. Płoszajczak, and T. Vertse, Journal of Physics G: Nuclear and Particle Physics, **36**(1), 013101, 2008.
URL <http://dx.doi.org/10.1088/0954-3899/36/1/013101>
- [120] J. Okołowicz, M. Płoszajczak, and W. Nazarewicz, Progress of Theoretical Physics Supplement, **196**, 230–243, 2012.
URL <http://dx.doi.org/10.1143/PTPS.196.230>
- [121] M. Płoszajczak and J. Okołowicz, arXiv e-prints, arXiv:1910.06526, 2019.